Hybrid Qubit–Rotor Quantum Systems: Clifford Structure, Universal Control, and Applications

Dengyao Luo*[1], Arvin Kushwaha†[1,2,3], Mastawal Tirfe[1,2], and Bojko N. Bakalov‡[1]

[1]*Department of Mathematics, North Carolina State University, Raleigh, North Carolina 27695, USA*
[2]*Department of Physics, North Carolina State University, Raleigh, North Carolina, 27695, USA*
[3]*Department of Physics, Universität Stuttgart, Stuttgart, Baden-Württemberg, 70569, Germany*

August 20, 2026

Abstract

A $U(1)$ quantum rotor pairs a periodic angle with an integer-valued conjugate momentum, and occurs in molecular rotation, superconducting phase–charge circuits, and compact gauge fields. Coupling such a rotor coherently to qubits gives a hybrid register whose control structure is not inherited from either the oscillator–qubit or the qudit case. We develop a Clifford theory, together with a universal-control result, for registers of n qubits and r rotors. We classify all automorphisms of the hybrid phase space $\mathbb{F}_2^{2n} \times \mathbb{Z}^r \times \mathbb{T}^r$ that preserve the Weyl commutation relations, and give an explicit finite Clifford circuit for each one. The classification is directional: rotor momentum parity may control qubit Pauli operations within the Clifford group, while every nonzero qubit-controlled rotor momentum shift is non-Clifford. It also yields normal forms for the mixed qubit–rotor couplings and the exact minimum number of elementary mixed gates needed to synthesize them. Adding a rotor cosine potential and one fixed qubit–rotor conditional phase to the local Clifford operations gives universal control on the full Hilbert space in the strong operator topology. We then apply this structure in three settings: an exact controlled-shift realization of gauge-covariant matter hopping, which is necessarily non-Clifford; rotor phase estimation with direct angle readout and probe optimization under momentum-support and energy constraints; and finite Fourier transforms on rotor momentum codes, where the one-rotor transform for $d = 2^s$ compiles into $O(s)$ momentum-selective and controlled-shift instructions and each cross-register Fourier factor is implemented by one quadratic rotor Clifford gate.

Contents

*dluo6@ncsu.edu
†research@arvinsk.org
‡bnbakalo@ncsu.edu

1 Introduction

Quantum rotors arise in molecular rotation, rotational motion of trapped particles, superconducting phase–charge degrees of freedom, and compact $U(1)$ gauge fields [1–7]. Their Hilbert spaces also support finite-dimensional logical encodings [8, 9], while planar-rotor models can instead be digitized into qubit registers [10]. Here we retain the rotor itself as a computational degree of freedom and allow it to interact coherently with qubits.

Such hybrid qubit–rotor systems occur in several contexts. In compact $U(1)$ gauge–matter theory, gauge links carry integer electric flux while matter is represented by finite-dimensional degrees of freedom [11]. Recent quantum-simulation proposals likewise combine finite-dimensional matter registers with infinite-dimensional gauge degrees of freedom [7, 12, 13], and direct qubit–rotor couplings appear in hybrid quantum rotor devices [14]. Rotor quantum phase estimation uses a rotor as the phase register for a qubit target [15], while hybrid processor architectures require coherent interfaces between finite- and infinite-dimensional registers [16, 17]. In each case, control is required both within the individual registers and across the qubit–rotor interface.

These examples share a common control problem. The two registers have incompatible phase spaces, and once they are coupled, the transformations preserving their joint commutation relations are no longer determined by either one alone. Neither is the set of operations needed to go beyond them.

Much of hybrid quantum processing has been developed for oscillator modes [16, 18–21], and oscillator–qudit systems admit a corresponding stabilizer and symplectic theory [22]. Unlike an oscillator, which has two continuous phase-space directions, a $U(1)$ rotor pairs a compact configuration variable with a discrete momentum [23]: its angle $\theta \in \mathbb{T} = \mathbb{R}/2\pi\mathbb{Z}$ and integer-valued angular momentum $\ell \in \mathbb{Z}$ form the Pontryagin-dual pair

$$\mathbb{Z} \longleftrightarrow \mathbb{T}.$$

For n qubits and r rotors, the Weyl operators are parametrized by the Abelian group

$$K_{n,r} = \mathbb{F}_2^{2n} \times \mathbb{Z}^r \times \mathbb{T}^r.$$

The first consequence is an asymmetry in the mixed Clifford action. Rotor momentum parity can control a qubit Pauli operation, but no Clifford operation can make a qubit control a nonzero rotor momentum shift, since every homomorphism from $\mathbb{F}_2^{2n}$ to $\mathbb{Z}^r$ is trivial. This has no counterpart in oscillator–qubit systems, where the mixed blocks vanish in both directions, or in finite qudit systems, where they can be nonzero in both.

Normalizer circuits over Abelian groups provide the general setting for this structure. Ref. [24] develops a generalized stabilizer formalism for such groups, including the configuration group $\mathbb{F}_2^n \times \mathbb{Z}^r$ underlying $K_{n,r}$, and establishes the corresponding Gottesman–Knill simulation result, which the hybrid Clifford circuits constructed below inherit. Ref. [25] gives a broader quadratic formulation of Clifford-type structures over Abelian groups, and the pure-rotor Clifford structure is described in Ref. [26]. In these treatments group automorphisms enter as normalizer-gate primitives, as the simulation theorem requires.

We work out the qubit–rotor case at the level of circuits and cost. Every automorphism preserving the Weyl commutator has the unique block form of Theorem 2.3, and each one is realized by an explicit finite circuit assembled from qubit Clifford gates, rotor Clifford gates, and elementary mixed gates (Theorem 2.4). The qubit–rotor coupling is carried entirely by one binary matrix, the mixed block C, which determines both the parity-controlled Pauli action and the antisymmetric part of the shear matrix Θ. Under Clifford operations acting separately on the two registers, C is completely classified by the pair $k = \operatorname{rank}_{\mathbb{F}_2} C$ and $h = \frac{1}{2} \operatorname{rank}_{\mathbb{F}_2}\big(C^{\mathsf{T}} J_n C\big)$ (Theorem 2.7). Here k counts the independent qubit Pauli directions controlled by rotor momentum parity and equals the minimum number of elementary mixed gates in the cost model of Corollary 2.8, while h counts the independent anticommuting pairs among those directions.

The same analysis applies directly to parameterized gates. Sec. 3 determines the Clifford parameter values of the momentum- and angle-dependent operations that arise on rotor platforms: momentum-diagonal phases, momentum-dependent qubit gates, periodic angle potentials, and qubit-controlled rotor displacements. In particular, every nonzero qubit-controlled rotor momentum shift is non-Clifford. Beyond the Clifford group, the local Clifford operations $\mathrm{Cl}_{n,r}^{\mathrm{loc}}$, the cosine-potential family $K_1(t)$ on one rotor, and the fixed conditional phase $C_{c_1,1}(\pi/4)$ generate a subgroup of $\mathrm{U}(\mathcal{H}_{n,r})$ that is dense in the strong operator topology for $n, r \geq 1$. The single-rotor step uses spectral controllability results for infinite-dimensional bilinear Schrödinger systems [27, 28]. This is an existence result: it gives no bound on circuit length or control time.

The first application is compact $U(1)$ gauge–matter dynamics. Rotor links carry integer electric flux and qubits encode matter occupations [11, 12]; related implementations use qubit–qumode or superconducting phase–charge degrees of freedom [7, 13]. Gauge-covariant hopping transfers a matter excitation between neighboring sites together with a unit change of the intervening link flux. We realize its time evolution exactly on the full rotor Hilbert space by conjugating a qubit exchange with a qubit-controlled rotor shift. The shift is non-Clifford, so gauge-covariant hopping lies outside the Clifford group: every hopping term in a rotor-based compact $U(1)$ simulation carries an irreducible non-Clifford cost. This construction is exact only on the full rotor space; we therefore study hard-wall electric-flux truncation through ground-state and real-time calculations on an open two-plaquette model.

A second application uses the rotor as the phase register in quantum phase estimation [15]. The momentum label ℓ indexes the controlled powers $U^{-\ell}$ of the target unitary. Phase kickback produces the character $e^{-i\ell\varphi}$ of $\mathbb{Z}$, which translates the conjugate angle distribution under $\mathbb{Z} \longleftrightarrow \mathbb{T}$. The eigenphase can therefore be read directly from an angle measurement, without a coherent inverse QFT on the phase register. The initial rotor probe determines both the estimation accuracy and the required range of controlled powers. At fixed momentum support, the optimum is the cosine-window probe [29, 30]; at fixed mean kinetic energy, the optimum is a Mathieu probe [31]. Under the circular-variance criterion, both optimized probes give $O(E_R^{-1/2})$ angular-error scaling for $E_R = \langle \hat{\ell}^2 \rangle$, compared with $O(E_R^{-1/4})$ for the uniform finite-momentum probe.

The third application uses finite rotor codes for Fourier processing. We construct the same finite Fourier matrix in two forms, related to hybrid state-transfer and oscillator-assisted Fourier methods [17, 32]. One construction maps an angle code to a momentum code using local angle-to-momentum Fourier operations and mixed code-space phases. The other remains within a rotor momentum code and compiles the transform using the hybrid gate set developed earlier. Under the logical-instruction convention stated in Sec. 7.4, the one-rotor compilation for $d = 2^s$ uses $O(s)$ instructions. Each cross-register base-d Fourier phase is implemented by the rotor–rotor quadratic Clifford gate

$$\mathrm{CPHS}_{jk}(\alpha) := e^{i\alpha \hat{\ell}_j \hat{\ell}_k},$$

while the corresponding factor in the binary decomposition contains s^2 controlled-phase gates.

These constructions are formulated at the level of logical operations. Sec. 8 connects them to native-rotor and finite-code implementations. Superconducting phase–charge circuits provide the quadratic momentum and cosine terms used in the control construction [7, 33]. Finite-code implementations can instead use spectrally selective qubit control, conditional displacements, and nonlinear interactions on a chosen subspace of another infinite-dimensional system [21, 34–36]. For the compiled QFT, the main requirements are resolution of individual binary digits of the momentum label and, for $r \geq 2$, a cross-register interaction angle $2\pi/d^r$.

2 Clifford structure of hybrid qubit–rotor systems

We begin by constructing the Weyl and Clifford structure of the hybrid qubit–rotor register. The commutator pairing on $K_{n,r} = \mathbb{F}_2^{2n} \times \mathbb{Z}^r \times \mathbb{T}^r$ fixes the allowed phase-space transformations. Their block form leads to finite Clifford circuit realizations. Local changes of basis then reduce the mixed block to two rank invariants and give the elementary mixed-gate cost.

2.1 Hybrid register and phase space

Throughout this paper, a rotor means a $U(1)$ quantum rotor with configuration group $\mathbb{T} = \mathbb{R}/2\pi\mathbb{Z} \cong S^1$ and momentum group $\mathbb{Z}$. Consider n qubits and r rotors,

$$\mathcal{H}_{n,r} = (\mathbb{C}^2)^{\otimes n} \otimes \ell^2(\mathbb{Z}^r) \simeq (\mathbb{C}^2)^{\otimes n} \otimes L^2(\mathbb{T}^r). \tag{2.1}$$

The rotor phase space pairs the discrete group $\mathbb{Z}^r$ with the compact group $\mathbb{T}^r$. We use the joint basis

$$|u, \ell\rangle, \qquad u \in \mathbb{F}_2^n, \quad \ell \in \mathbb{Z}^r. \tag{2.2}$$

For one rotor, the generalized angle states are related to momentum states by the Fourier relation

$$|\theta\rangle = \frac{1}{\sqrt{2\pi}} \sum_{\ell \in \mathbb{Z}} e^{-i\ell\theta} |\ell\rangle. \tag{2.3}$$

All angle-dependent operators below are defined through periodic functions, such as $e^{im\hat{\theta}}$ and $\cos\hat{\theta}$.

The joint qubit computational basis and rotor momentum basis are indexed by the Abelian group $A_{n,r} = \mathbb{F}_2^n \times \mathbb{Z}^r$. Its Pontryagin dual, $\widehat{A}_{n,r} = \mathbb{F}_2^n \times \mathbb{T}^r$, indexes the corresponding phase operators.

We define the hybrid qubit–rotor phase space by

$$K_{n,r} = A_{n,r} \times \widehat{A}_{n,r} \cong \mathbb{F}_2^{2n} \times \mathbb{Z}^r \times \mathbb{T}^r. \tag{2.4}$$

The Weyl commutator pairing introduced below equips $K_{n,r}$ with its symplectic structure.

Write

$$x = (q, m, \phi), \qquad q = \begin{pmatrix} a \\ b \end{pmatrix} \in \mathbb{F}_2^{2n}, \quad m \in \mathbb{Z}^r, \quad \phi \in \mathbb{T}^r, \tag{2.5}$$

and define

$$J_n = \begin{pmatrix} 0 & I_n \\ I_n & 0 \end{pmatrix}. \tag{2.6}$$

An overbar on an integer vector or matrix denotes entrywise reduction modulo two. For a matrix M over $\mathbb{F}_2$, πM denotes the corresponding matrix with entries in $\mathbb{T}$, under the entrywise identification $0 \mapsto 0$ and $1 \mapsto \pi$.

2.2 Weyl multiplication and commutation relation

Define the qubit Weyl operators by

$$X_Q(a)|u\rangle = |u + a\rangle, \qquad Z_Q(b)|u\rangle = (-1)^{b^\mathsf{T} u} |u\rangle, \tag{2.7}$$

and define the rotor momentum shift $X_R(m)$ and rotor phase operator $Z_R(\phi)$ by

$$X_R(m)|\ell\rangle = |\ell + m\rangle, \qquad Z_R(\phi)|\ell\rangle = e^{i\phi^\mathsf{T}\ell} |\ell\rangle. \tag{2.8}$$

We write the corresponding rotor Weyl displacement as

$$D_R(m, \phi) := X_R(m) Z_R(\phi). \tag{2.9}$$

For $x = (q, m, \phi) \in K_{n,r}$, define the associated hybrid Weyl operator by

$$W(x) = W(q, m, \phi) := X_Q(a) Z_Q(b) \otimes X_R(m) Z_R(\phi). \tag{2.10}$$

For $y = (q', m', \phi') \in K_{n,r}$, direct multiplication gives

$$W(x)W(y) = \sigma(x, y) W(x + y), \qquad \sigma(x, y) = (-1)^{b^\mathsf{T} a'} e^{i\phi^\mathsf{T} m'}. \tag{2.11}$$

Reversing the product order gives

$$W(x)W(y) = \omega(x, y) W(y) W(x), \tag{2.12}$$

where

$$\omega(x, y) = \frac{\sigma(x, y)}{\sigma(y, x)} = (-1)^{q^\mathsf{T} J_n q'} \exp\Big(i[\phi^\mathsf{T} m' - {\phi'}^\mathsf{T} m]\Big). \tag{2.13}$$

The Weyl commutator pairing ω is continuous and multiplicative in each phase-space argument.

Lemma 2.1 (Perfectness of the commutator pairing)**.** *The map*

$$D_\omega : K_{n,r} \longrightarrow \widehat{K}_{n,r}, \qquad y \longmapsto \omega(y, \cdot\,), \tag{2.14}$$

is an isomorphism. Thus every continuous character of $K_{n,r}$ can be written uniquely in the form $\omega(y, \cdot\,)$ for some $y \in K_{n,r}$.

Proof. Set $\mathcal{A} = A_{n,r}$ and write $K_{n,r} = \mathcal{A} \times \widehat{\mathcal{A}}$. For $x = (u, \chi)$ and $y = (v, \psi)$, Eq. (2.13) becomes

$$\omega(x, y) = \chi(v) \psi(u)^{-1}. \tag{2.15}$$

Let $\iota_\mathcal{A} : \mathcal{A} \longrightarrow \widehat{\widehat{\mathcal{A}}}$ be the evaluation map. Under the natural identification $\widehat{K_{n,r}} \cong \widehat{\mathcal{A}} \times \widehat{\widehat{\mathcal{A}}}$, the map D_ω is

$$D_\omega(u, \chi) = \big(\chi, -\iota_\mathcal{A}(u)\big). \tag{2.16}$$

Pontryagin biduality identifies $\mathcal{A}$ with $\widehat{\widehat{\mathcal{A}}}$. Hence D_ω is a topological group isomorphism, which proves the claim [37, Example 1.1]. ☐

2.3 Hybrid Clifford group and induced phase-space action

Adjoining scalar phases to the hybrid Weyl operators gives the hybrid Pauli group

$$\mathcal{P}_{n,r} = \{ z W(x) : z \in \mathrm{U}(1),\ x \in K_{n,r} \}. \tag{2.17}$$

Since the commutator pairing is nondegenerate, the center of $\mathcal{P}_{n,r}$ consists of the scalar phases: $Z(\mathcal{P}_{n,r}) = \mathrm{U}(1)$. Moreover, the map $zW(x) \mapsto x$ induces a group isomorphism $\mathcal{P}_{n,r}/\mathrm{U}(1)I \cong K_{n,r}$.

The hybrid Clifford group is defined as the unitary normalizer of $\mathcal{P}_{n,r}$:

$$\mathrm{Cl}_{n,r} = N_{\mathrm{U}(\mathcal{H}_{n,r})}(\mathcal{P}_{n,r}). \tag{2.18}$$

Lemma 2.2 (Clifford action on phase space)**.** *For every $U \in \mathrm{Cl}_{n,r}$, conjugation induces a unique group automorphism $S_U : K_{n,r} \to K_{n,r}$. For the chosen Weyl representatives, there is a unique phase function $\alpha_U : K_{n,r} \to \mathrm{U}(1)$ such that*

$$U W(x) U^\dagger = \alpha_U(x) W(S_U x). \tag{2.19}$$

Moreover, S_U preserves the commutator pairing:

$$\omega(S_U x, S_U y) = \omega(x, y), \qquad x, y \in K_{n,r}. \tag{2.20}$$

Proof. Conjugation by U induces an automorphism of $\mathcal{P}_{n,r}/\mathrm{U}(1)I \cong K_{n,r}$, which defines S_U. The remaining scalar defines α_U. Since conjugation preserves operator commutators, S_U preserves ω. ☐

Define

$$\mathrm{Sp}(K_{n,r}, \omega) = \{ S \in \mathrm{Aut}(K_{n,r}) : \omega(Sx, Sy) = \omega(x, y) \text{ for all } x, y \in K_{n,r} \}. \tag{2.21}$$

The preceding lemma therefore defines a homomorphism $\pi : \mathrm{Cl}_{n,r} \longrightarrow \mathrm{Sp}(K_{n,r}, \omega)$ by $U \longmapsto S_U$.

2.4 Classification of hybrid phase-space transformations

Theorem 2.3 (Hybrid phase-space classification)**.** *Every group automorphism of $K_{n,r}$ preserving ω is automatically continuous and has the unique form*

$$S_{M,A,C,\Theta}(q,m,\phi) = \left(Mq + C\bar{m}, Am, A^{-\mathsf{T}}[\phi + \Theta m + \pi C^{\mathsf{T}} J_n M q]\right), \tag{2.22}$$

where $M \in \mathrm{Sp}(2n, \mathbb{F}_2), A \in \mathrm{GL}(r, \mathbb{Z}), C \in \mathrm{Mat}_{2n\times r}(\mathbb{F}_2), \Theta \in \mathrm{Mat}_r(\mathbb{T}),$ *and*

$$\Theta - \Theta^{\mathsf{T}} = \pi C^{\mathsf{T}} J_n C. \tag{2.23}$$

Conversely, every such tuple defines an element of $\mathrm{Sp}(K_{n,r}, \omega)$*.*

The matrix M is the qubit symplectic action familiar from the stabilizer formalism [38]. The matrix A preserves the rotor momentum lattice, and Θ is the shear matrix. The binary matrix C records the mixed qubit–rotor action $q \longmapsto q + C\bar{m}$.

Writing c_j for the jth column of C, each $c_j \in \mathbb{F}_2^{2n}$ labels a qubit Pauli operator P_{c_j} up to phase. We call the nonzero columns the Pauli directions controlled by rotor momentum parity. Their pairwise commutation relations are recorded by $C^{\mathsf{T}} J_n C$: its (i,j) entry is zero when P_{c_i} and P_{c_j} commute and one when they anticommute. These mixed commutators leave the antisymmetric part of the shear no freedom. Eq. (2.23) fixes it as $\Theta - \Theta^{\mathsf{T}} = \pi C^{\mathsf{T}} J_n C$, so only the symmetric part of Θ remains an independent parameter.

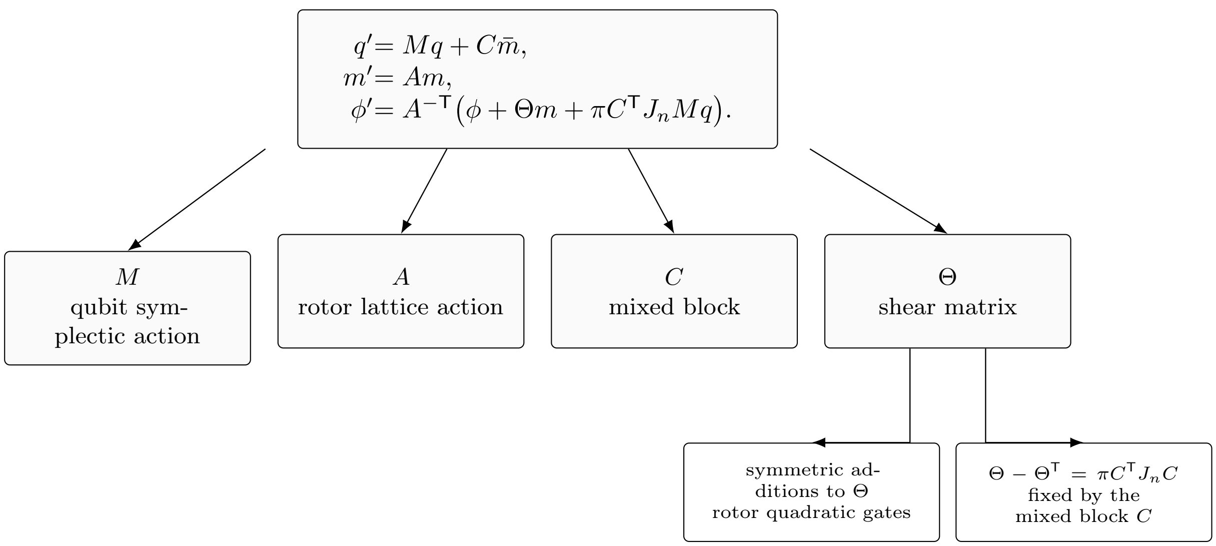

Figure 1: Block structure of the hybrid symplectic map. The matrices M and A describe the qubit symplectic and rotor lattice actions, and C is the mixed block. The difference $\Theta - \Theta^{\mathsf{T}} = \pi C^{\mathsf{T}} J_n C$ is fixed by the mixed block; symmetric additions to Θ correspond to rotor quadratic gates.

Proof sketch. A homomorphism first has the block form $q' = Mq + C\bar{m}, m' = Am, \phi' = \alpha(\phi) + Bm + \pi Gq$. The vanishing homomorphism groups and the uniqueness of the remaining blocks are established in Appendix A.1. The pure qubit commutators give $M^{\mathsf{T}} J_n M = J_n$. The torus–integer commutators force $\alpha(\phi) = A^{-\mathsf{T}}\phi$, which also removes discontinuous torus automorphisms. The finite–integer and integer–integer commutators then determine G and Eq. (2.23). Direct substitution proves the converse. The appendix also gives the composition law and inverse. □

As a first specialization of Theorem 2.3, set $n = 0$. Then q and M are absent, and the $0 \times r$ mixed matrix C vanishes. Hence

$$S_{A,\Theta}(m,\phi) = \left(Am, A^{-\mathsf{T}}[\phi + \Theta m]\right), \qquad \Theta = \Theta^{\mathsf{T}}. \tag{2.24}$$

Define the phase-space transformations $L_A(m,\phi) = (Am, A^{-\mathsf{T}}\phi), N_\Theta(m,\phi) = (m, \phi + \Theta m)$. Then $S_{A,\Theta} = L_A N_\Theta$, and a direct conjugation gives

$$L_A N_\Theta L_A^{-1} = N_{A^{-\mathsf{T}}\Theta A^{-1}}. \tag{2.25}$$

Hence the symmetric shear parameters form a normal subgroup on which $\mathrm{GL}(r,\mathbb{Z})$ acts by $\Theta \mapsto A^{-\mathsf{T}}\Theta A^{-1}$. Since a symmetric $r \times r$ matrix with entries in $\mathbb{T}$ has $r(r+1)/2$ independent entries, the pure-rotor symplectic group is

$$\mathrm{Sym}_r(\mathbb{T}) \rtimes \mathrm{GL}(r,\mathbb{Z}) \simeq \mathrm{U}(1)^{r(r+1)/2} \rtimes \mathrm{GL}(r,\mathbb{Z}). \tag{2.26}$$

This recovers the known phase-space action of the pure-rotor Clifford group. Representative rotor gates are described in Ref. [26]. In the pure-qubit case, $r = 0$ removes A, C, and Θ, leaving the standard qubit symplectic group $\mathrm{Sp}(2n, \mathbb{F}_2)$.

2.5 Unitary realization of hybrid symplectic maps

For $c = (a,b) \in \mathbb{F}_2^{2n}$, define the Hermitian Pauli operator associated with c by $P_c = i^{a^\mathsf{T} b} X_Q(a) Z_Q(b), P_c = P_c^\dagger, P_c^2 = I$. For rotor j, define

$$\Gamma_{c,j} = \sum_{\ell \in \mathbb{Z}^r} P_c^{\ell_j \bmod 2} \otimes |\ell\rangle\langle\ell|. \tag{2.27}$$

This gate applies P_c when ℓ_j is odd and the identity when ℓ_j is even. Its induced mixed block is $C = c e_j^\mathsf{T}$, which has rank one when $c \neq 0$.

When $n, r \geq 1$, take $c = (0, e_1)$, so that $P_c = Z_1$, and set $j = 1$. Then

$$\Gamma_{c,1} = C_\pi = e^{i\pi |1\rangle\langle 1|_{q_1} \otimes \hat{\ell}_1}. \tag{2.28}$$

For $M \in \mathrm{Sp}(2n, \mathbb{F}_2)$, choose a qubit Clifford V_M inducing $q \longmapsto Mq$. For $A \in \mathrm{GL}(r,\mathbb{Z})$, define the rotor automorphism unitary by

$$U_A |\ell\rangle = |A\ell\rangle. \tag{2.29}$$

For $R = R^\mathsf{T} \in \mathrm{Mat}_r(\mathbb{T})$, set

$$f_R(\ell) = \sum_{j=1}^{r} R_{jj} \frac{\ell_j(\ell_j+1)}{2} + \sum_{1 \leq i < j \leq r} R_{ij} \ell_i \ell_j, \tag{2.30}$$

$$Q_R |\ell\rangle = e^{i f_R(\ell)} |\ell\rangle. \tag{2.31}$$

Their induced actions on rotor phase space are

$$\begin{aligned} U_A :&\quad (m,\phi) \longmapsto (Am, A^{-\mathsf{T}}\phi), \\ Q_R :&\quad (m,\phi) \longmapsto (m, \phi + Rm). \end{aligned} \tag{2.32}$$

Consequently, the combined unitary $V_M \otimes (U_A Q_R)$ induces

$$L_{M,A,R}(q,m,\phi) = \big(Mq,\ Am,\ A^{-\mathsf{T}}(\phi + Rm)\big). \tag{2.33}$$

The next theorem realizes every symplectic automorphism in Theorem 2.3 by a finite circuit. The chosen order of the mixed gates produces a triangular contribution to the shear Θ, and a quadratic gate acting only on the rotor register supplies the remaining symmetric contribution.

Theorem 2.4 (Explicit hybrid Clifford realization)**.** *Let $S = S_{M,A,C,\Theta}$ be a map classified in Theorem 2.3. Set*

$$D = M^{-1}C = (d_1, \ldots, d_r), \qquad \Gamma_D := \Gamma_{d_r,r} \cdots \Gamma_{d_1,1}, \tag{2.34}$$

so that the gates $\Gamma_{d_1,1}, \ldots, \Gamma_{d_r,r}$ act in increasing order of the rotor index.

Define $\Theta_D^\triangle \in \mathrm{Mat}_r(\mathbb{T})$ by

$$(\Theta_D^\triangle)_{ji} = \begin{cases} \pi d_j^\mathsf{T} J_n d_i, & i < j, \\ 0, & i \geq j, \end{cases} \tag{2.35}$$

and set $\Theta_{\mathrm{loc}} := \Theta - \Theta_D^{\triangle}$*. Then* Θ_{loc} *is symmetric, and*

$$U_S := \big[V_M \otimes (U_A Q_{\Theta_{\mathrm{loc}}})\big]\Gamma_D, \tag{2.36}$$

$$U_S W(x) U_S^{\dagger} \propto W(Sx), \qquad x \in K_{n,r}. \tag{2.37}$$

Proof. First isolate the mixed part by setting $M = A = I$:

$$S_{I,I,D,\Xi}(q,m,\phi) = \left(q + D\bar{m},\, m,\, \phi + \Xi m + \pi D^{\mathsf{T}} J_n q\right). \tag{2.38}$$

The elementary mixed gate satisfies

$$\Gamma_{c,j} : (q,m,\phi) \longmapsto \left(q + c\bar{m}_j,\, m,\, \phi + \pi e_j c^{\mathsf{T}} J_n q\right). \tag{2.39}$$

Applying the factors in $\Gamma_D = \Gamma_{d_r,r} \cdots \Gamma_{d_1,1}$ in increasing rotor order and iterating Eq. (2.39) gives

$$\Gamma_D : (q,m,\phi) \longmapsto \left(q + D\bar{m},\, m,\, \phi + \Theta_D^{\triangle} m + \pi D^{\mathsf{T}} J_n q\right). \tag{2.40}$$

Thus Γ_D implements $S_{I,I,D,\Theta_D^{\triangle}}$. By construction,

$$\Theta_D^{\triangle} - (\Theta_D^{\triangle})^{\mathsf{T}} = \pi D^{\mathsf{T}} J_n D. \tag{2.41}$$

Since $D = M^{-1}C$ and M is symplectic, $D^{\mathsf{T}} J_n D = C^{\mathsf{T}} J_n C$. Together with Eq. (2.23), this implies $\Theta_{\mathrm{loc}} - \Theta_{\mathrm{loc}}^{\mathsf{T}} = 0$. Hence Θ_{loc} is symmetric, and $Q_{\Theta_{\mathrm{loc}}}$ is a rotor quadratic gate. The unitary $V_M \otimes (U_A Q_{\Theta_{\mathrm{loc}}})$ implements $L_{M,A,\Theta_{\mathrm{loc}}}$ from Eq. (2.33).

Using $D = M^{-1}C$, $\Theta_D^{\triangle} + \Theta_{\mathrm{loc}} = \Theta$, and $D^{\mathsf{T}} J_n = C^{\mathsf{T}} J_n M$ gives

$$S_{M,A,C,\Theta} = L_{M,A,\Theta_{\mathrm{loc}}} \circ S_{I,I,D,\Theta_D^{\triangle}}, \qquad U_S W(x) U_S^{\dagger} \propto W(Sx). \tag{2.42}$$

This completes the construction of a unitary lift for every element of $\mathrm{Sp}(K_{n,r}, \omega)$. $\square$

Corollary 2.5 (Clifford–symplectic exact sequence)**.** *Conjugation on Weyl operators induces a surjective homomorphism* $\pi_{n,r} : \mathrm{Cl}_{n,r} \longrightarrow \mathrm{Sp}(K_{n,r}, \omega)$*, by* $U \longmapsto S_U$*, with kernel* $\mathcal{P}_{n,r}$*. Consequently,*

$$1 \longrightarrow \mathcal{P}_{n,r} \longrightarrow \mathrm{Cl}_{n,r} \xrightarrow{\pi_{n,r}} \mathrm{Sp}(K_{n,r}, \omega) \longrightarrow 1 \tag{2.43}$$

is a short exact sequence, and $\mathrm{Cl}_{n,r} / \mathcal{P}_{n,r} \simeq \mathrm{Sp}(K_{n,r}, \omega)$*.*

Proof. The homomorphism property follows from composition of the induced phase-space actions, and surjectivity follows from Theorem 2.4. It remains to identify the kernel. If $S_U = \mathrm{id}$, then $UW(x)U^{\dagger} = \chi(x)W(x)$ for a phase function χ on $K_{n,r}$. Comparison with the Weyl multiplication law shows that χ is a character.

Since $W(x)$ depends continuously on x, the identity $UW(x)U^{\dagger}W(x)^{\dagger} = \chi(x)I$ shows that χ is continuous. By Lemma 2.1, there exists $y \in K_{n,r}$ such that $\chi(x) = \omega(y,x)$ for all $x \in K_{n,r}$. Hence $V := W(y)^{\dagger}U$ commutes with every Weyl operator. Commutation with all qubit and rotor phase operators makes V diagonal in the joint basis. Commutation with all qubit and rotor shifts makes its diagonal entries equal. Thus V is a scalar and $U \in \mathcal{P}_{n,r}$. The reverse inclusion follows directly from the Weyl commutation relations. The quotient statement follows from the first isomorphism theorem. $\square$

Corollary 2.6 (Generators of the hybrid Clifford group)**.** *For* $n, r \geq 1$*,*

$$\mathrm{Cl}_{n,r} = \langle \mathcal{P}_{n,r}, \mathrm{Cl}_{n,0}, \mathrm{Cl}_{0,r}, C_{\pi} \rangle. \tag{2.44}$$

For $n = 0$ *or* $r = 0$*, the mixed generator* C_{π} *is omitted.*

Proof. Every operator on the right-hand side of Eq. (2.44) is a hybrid Clifford operator.

Conversely, let $U \in \mathrm{Cl}_{n,r}$, and let S_U be its induced phase-space action. By Theorem 2.4, there is an explicitly constructed unitary U_{S_U} satisfying $\pi_{n,r}(U_{S_U}) = S_U$. The elementary mixed gates occurring in U_{S_U} are generated by C_π, Clifford operators acting only on one register, and Weyl operators, while its remaining factors belong to $\mathrm{Cl}_{n,0}$ or $\mathrm{Cl}_{0,r}$. Hence U_{S_U} is generated by the operators in Eq. (2.44).

Since U and U_{S_U} induce the same phase-space action, $UU_{S_U}^\dagger \in \ker \pi_{n,r} = \mathcal{P}_{n,r}$. Therefore $U = (UU_{S_U}^\dagger)U_{S_U}$ is also generated by the operators in Eq. (2.44).

Fix $c \neq 0$ and choose a qubit Clifford V_c such that $V_c Z_1 V_c^\dagger = \varepsilon_c P_c$ with $\varepsilon_c \in \{\pm 1\}$. Choose a rotor permutation U_{π_j} that moves rotor 1 to rotor j. Then

$$(V_c \otimes U_{\pi_j}) C_\pi (V_c \otimes U_{\pi_j})^\dagger = \begin{cases} \Gamma_{c,j}, & \varepsilon_c = +1, \\ Z_{R,j}(\pi)\Gamma_{c,j}, & \varepsilon_c = -1. \end{cases} \tag{2.45}$$

The extra factor in the second line is a rotor Weyl operator. □

Example 2.1 (One qubit and one rotor)**.** For the smallest nontrivial hybrid register,

$$\mathrm{Sp}(K_{1,1}, \omega) \cong \mathbb{T} \times S_4 \times \mathbb{Z}_2. \tag{2.46}$$

Here the factor $\mathbb{T}$ is the one-rotor shear parameter, $\mathbb{Z}_2$ records momentum reversal, and $S_4 \cong \mathrm{AGL}(2, \mathbb{F}_2)$ combines the one-qubit symplectic action with the mixed parity-controlled Pauli action. The group identification is proved in Appendix A.2.

Classical simulation. The generators in Corollary 2.6 are normalizer operations over the Abelian group $A_{n,r} = \mathbb{F}_2^n \times \mathbb{Z}^r$. Hybrid Clifford circuits with the stabilizer inputs and measurements are therefore covered by the generalized Gottesman–Knill simulation result of Ref. [24].

2.6 Classification of mixed Clifford couplings

Let $V = \mathbb{F}_2^{2n}, \beta_J(u, v) = u^\mathsf{T} J_n v$, and regard C as a linear map from $\mathbb{F}_2^r$ to V. Clifford operations acting separately on the qubit and rotor registers transform C as

$$C \longmapsto MCR, \qquad M \in \mathrm{Sp}(2n, \mathbb{F}_2), \quad R \in \mathrm{GL}(r, \mathbb{F}_2). \tag{2.47}$$

Here $R = \overline{A}^{-1}$ for a rotor basis change $A \in \mathrm{GL}(r, \mathbb{Z})$. Every R occurs because reduction modulo two maps $\mathrm{GL}(r, \mathbb{Z})$ onto $\mathrm{GL}(r, \mathbb{F}_2)$. The right action changes the basis of the domain; the left action sends $\operatorname{im} C$ to $M(\operatorname{im} C)$.

Under this action, the orbit of C is determined by the alternating space $(\operatorname{im} C, \beta_J|_{\operatorname{im} C})$. Witt extension lifts its normal form to the ambient symplectic space.

Theorem 2.7 (Classification of mixed blocks)**.** *The pair*

$$(k, h) = \left(\operatorname{rank}_{\mathbb{F}_2} C, \frac{1}{2} \operatorname{rank}_{\mathbb{F}_2}(C^\mathsf{T} J_n C)\right) \tag{2.48}$$

is a complete invariant of the action in Eq. (2.47)*. Two mixed blocks are equivalent under separate qubit and rotor Clifford operations if and only if they have the same pair* (k, h)*.*

Fix a symplectic basis $e_1, f_1, \ldots, e_n, f_n$ *of* V*. Every orbit contains a representative whose nonzero columns are*

$$e_1, f_1, \ldots, e_h, f_h, e_{h+1}, \ldots, e_{k-h}, \tag{2.49}$$

followed by $r - k$ *zero columns. The admissible values are*

$$0 \le k \le \min(r, 2n), \qquad \max(0, k - n) \le h \le \left\lfloor \frac{k}{2} \right\rfloor. \tag{2.50}$$

Proof. Invariance. Suppose that $C' = MCR, M \in \mathrm{Sp}(2n, \mathbb{F}_2), R \in \mathrm{GL}(r, \mathbb{F}_2)$. Then $\operatorname{rank} C' = \operatorname{rank} C$ and $(C')^{\mathsf{T}} J_n C' = R^{\mathsf{T}}(C^{\mathsf{T}} J_n C)R$. Hence both k and h are invariant under this action.

The quotient isomorphism $\mathbb{F}_2^r / \ker C \cong \operatorname{im} C$ identifies the alternating form represented by $C^{\mathsf{T}} J_n C$ with the restriction of β_J to $\operatorname{im} C$. Consequently, $k = \dim(\operatorname{im} C)$ and $2h = \operatorname{rank}(\beta_J|_{\operatorname{im} C})$.

Completeness. Now suppose that C and C' have the same pair (k, h). The restricted alternating spaces $(\operatorname{im} C, \beta_J|_{\operatorname{im} C})$ and $(\operatorname{im} C', \beta_J|_{\operatorname{im} C'})$ have the same dimension and rank, and are therefore isometric. By Witt extension, this isometry extends to an element $M \in \mathrm{Sp}(2n, \mathbb{F}_2)$ satisfying $M(\operatorname{im} C) = \operatorname{im} C'$ [39, Theorem 3.4].

The maps C and $M^{-1}C'$ are surjections $\mathbb{F}_2^r \longrightarrow \operatorname{im} C$ of the same rank. Choosing bases of $\mathbb{F}_2^r$ adapted to their kernels gives $R \in \mathrm{GL}(r, \mathbb{F}_2)$ such that $CR = M^{-1}C'$. Hence $MCR = C'$, so the pair (k, h) completely determines the orbit.

Normal form and admissible range. The space $\operatorname{im} C$ has a basis consisting of h symplectic pairs and $k - 2h$ vectors in the radical of $\beta_J|_{\operatorname{im} C}$. A symplectic transformation of V sends such a basis to $e_1, f_1, \ldots, e_h, f_h, e_{h+1}, \ldots, e_{k-h}$. A change of basis in $\mathbb{F}_2^r$ then places these vectors in the first k columns and makes the remaining $r - k$ columns zero.

This gives Eq. (2.49). The inequalities $k \le r, k \le 2n, 2h \le k$ give the upper bounds in Eq. (2.50). Moreover, the normal form contains an isotropic subspace of dimension $k - h$. Since an isotropic subspace of V has dimension at most n, together with $h \ge 0$, this gives the stated lower bound. Conversely, the columns in Eq. (2.49) exist for every pair (k, h) in this range. □

In this normal form, k counts the independent qubit Pauli directions controlled by rotor momentum parity, and h counts the independent anticommuting pairs among them. The remaining $k - 2h$ directions lie in the radical of the restricted alternating form. Through Eq. (2.23), the binary matrix $C^{\mathsf{T}} J_n C$ also fixes $\Theta - \Theta^{\mathsf{T}}$, and $\operatorname{rank}(C^{\mathsf{T}} J_n C) = 2h$.

Mixed-gate cost model. Qubit-only and rotor-only Clifford operations are free, and each elementary mixed gate $\Gamma_{c,j}$ counts once.

Corollary 2.8 (Minimum number of elementary mixed gates)**.** *In this model, the minimum number of elementary mixed gates required to realize an admissible mixed block C is $N_\Gamma^{\min}(C) = \operatorname{rank}_{\mathbb{F}_2} C$.*

Proof. These free operations act on C by invertible left and right multiplication and therefore preserve its rank. Under composition, Eq. (A.11) gives $C_{12} = M_1 C_2 + C_1 \bar{A}_2$. Hence a circuit containing t elementary mixed gates has a total mixed block that is a sum of at most t rank-one contributions, each multiplied on the left and right by invertible matrices. Rank subadditivity therefore gives $\operatorname{rank}_{\mathbb{F}_2} C \le t$. Thus at least $\operatorname{rank}_{\mathbb{F}_2} C$ elementary mixed gates are required.

Conversely, the representative in Eq. (2.49) has $k = \operatorname{rank} C$ nonzero columns, and each column is realized by one elementary mixed gate. The ordered product of these gates may also produce a rotor shear Θ_*. Since both Θ and Θ_* satisfy $\Theta - \Theta^{\mathsf{T}} = \Theta_* - \Theta_*^{\mathsf{T}} = \pi C^{\mathsf{T}} J_n C$, their difference $\Theta - \Theta_*$ is symmetric and can be implemented by a Clifford operation acting only on the rotor register. Thus $\operatorname{rank} C$ elementary mixed gates are sufficient. □

3 Gate families

The applications below use gates whose parameters depend on rotor momentum or angle. This section determines when those gates are Clifford. We also examine qubit-controlled rotor displacements, which reverse the direction of control in the elementary mixed Clifford gate.

3.1 Pure-rotor and mixed Clifford gates

We regard the pure-qubit Clifford group as standard and recall only the rotor and mixed gates used below. Up to a global phase, the pure-rotor Clifford group is generated by Weyl operators, momentum-lattice automorphisms, and quadratic phase gates. These operations are implemented by $D_R(m, \phi)$, U_A, and Q_R, respectively, as defined in Eqs. (2.9), (2.29), and (2.31) [26].

The following gates give concrete instances of the latter two types. For $i \neq j$ and $\alpha \in \mathbb{T}$, we use

$$\begin{aligned}
\mathrm{PAR}_j|\ell_j\rangle &= |-\ell_j\rangle, \\
\mathrm{SUM}_{i\to j}|\ell_i,\ell_j\rangle &= |\ell_i,\ell_j+\ell_i\rangle, \\
\mathrm{QUAD}_j(\alpha)|\ell_j\rangle &= e^{i\alpha\ell_j(\ell_j+1)/2}|\ell_j\rangle, \\
\mathrm{CPHS}_{ij}(\alpha)|\ell_i,\ell_j\rangle &= e^{i\alpha\ell_i\ell_j}|\ell_i,\ell_j\rangle.
\end{aligned} \tag{3.1}$$

PAR, SUM, and rotor SWAP implement elementary automorphisms of the momentum lattice $\mathbb{Z}^r$. QUAD and CPHS implement the diagonal and off-diagonal entries of the symmetric shear matrix R.

In the hybrid system, the elementary mixed Clifford gate $\Gamma_{c,j}$ in Eq. (2.27) acts as the identity for even ℓ_j and as P_c for odd ℓ_j. For $P_c = Z_1$ and $j = 1$, this family reduces to the one-qubit–one-rotor gate C_π in Eq. (2.28). For $n, r \geq 1$, Eq. (2.44) shows that C_π, together with $\mathcal{P}_{n,r}$, $\mathrm{Cl}_{n,0}$, and $\mathrm{Cl}_{0,r}$, generates $\mathrm{Cl}_{n,r}$.

3.2 Momentum-dependent gates

Momentum-dependent gates fall into two classes: scalar phase gates diagonal in the momentum basis and qubit gates selected by the rotor momentum. The phase in the first family must admit a quadratic representative on $\mathbb{Z}^r$. In the second, apart from a scalar rotor phase, the qubit blocks can vary only through momentum-parity powers of a fixed Pauli operator.

3.2.1 Momentum-diagonal phase gates

Let $u : \mathbb{Z}^r \to \mathrm{U}(1)$ and define

$$G_u|\ell\rangle = u(\ell)|\ell\rangle. \tag{3.2}$$

Proposition 3.1 (Clifford criterion for momentum-diagonal phase gates)**.** *The gate G_u belongs to $\mathrm{Cl}_{0,r}$ if and only if there are $\gamma \in \mathbb{T}$, $\lambda \in \mathbb{T}^r$, and $R = R^\mathsf{T} \in \mathrm{Mat}_r(\mathbb{T})$ such that*

$$u(\ell) = e^{i\gamma + i\lambda^\mathsf{T}\ell + if_R(\ell)} \text{for every } \ell \in \mathbb{Z}^r, \tag{3.3}$$

where f_R is defined in Eq. (2.30).

Proof sketch. Conjugating $X_R(e_j)$ shows that, if G_u is Clifford, the factor $u(\ell+e_j)u(\ell)^{-1}$ must be a character of $\mathbb{Z}^r$, up to a scalar. Compatibility of these finite differences gives a symmetric matrix R. Appendix B.1 solves the resulting difference equations on $\mathbb{Z}^r$ and obtains Eq. (3.3). Conversely, this form gives $G_u = e^{i\gamma}Z_R(\lambda)Q_R$, which is a pure-rotor Clifford gate. □

The degree of a polynomial expression for the phase does not by itself determine whether the gate is Clifford, since different polynomials may agree on the integer momentum spectrum. For one rotor,

$$e^{i\pi\hat{\ell}^3} = e^{i\pi\hat{\ell}} = Z_R(\pi), \tag{3.4}$$

because $\ell^3 - \ell$ is even for every $\ell \in \mathbb{Z}$.

3.2.2 Momentum-dependent qubit gates

For one rotor, let $\{V_\ell\}_{\ell\in\mathbb{Z}}$ be a sequence of n-qubit unitaries and consider the gate

$$\mathcal{V} = \sum_{\ell\in\mathbb{Z}} V_\ell \otimes |\ell\rangle\langle\ell|. \tag{3.5}$$

The qubit operation in each block depends on the rotor momentum ℓ.

Proposition 3.2 (Clifford criterion for momentum-dependent qubit gates)**.** *The gate $\mathcal{V}$ belongs to $\mathrm{Cl}_{n,1}$ if and only if there exist $V_0 \in \mathrm{Cl}_{n,0}, c \in \mathbb{F}_2^{2n}, \alpha, \lambda \in \mathbb{T}$ such that*

$$V_\ell = e^{i[\lambda\ell + \alpha\ell(\ell+1)/2]}P_c^\ell V_0 \qquad \text{for all } \ell \in \mathbb{Z}. \tag{3.6}$$

Proof sketch. Conjugating $I \otimes X_R(1)$ shows that Cliffordness forces $V_{\ell+1}V_\ell^\dagger = e^{i(\rho+\alpha\ell)}P_c$ for a fixed Pauli operator P_c. Appendix B.2 solves this recurrence for every $\ell \in \mathbb{Z}$ and gives Eq. (3.6) with a fixed unitary V_0. Conjugating the qubit Weyl operators shows that $V_0 \in \mathrm{Cl}_{n,0}$. Conversely, writing $\mathcal{V} = (I \otimes G_u)\Gamma_{c,1}(V_0 \otimes I)$, with $u(\ell) = e^{i[\lambda\ell+\alpha\ell(\ell+1)/2]}$, proves that $\mathcal{V}$ is Clifford. □

A simple specialization is the conditional phase gate

$$C_{c,j}(\varphi) = \exp\left[i\varphi\frac{I - P_c}{2} \otimes \hat{\ell}_j\right]. \tag{3.7}$$

Corollary 3.3 (Clifford criterion for the conditional-phase gate)**.** *For $n, r \geq 1$, $c \in \mathbb{F}_2^{2n} \setminus \{0\}$, $1 \leq j \leq r$, and $\varphi \in \mathbb{T}$,*

$$C_{c,j}(\varphi) \in \mathrm{Cl}_{n,r} \iff \varphi \equiv 0 \text{ or } \pi \pmod{2\pi}. \tag{3.8}$$

The case $\varphi \equiv 0$ gives the identity, while $C_{c,j}(\pi) = \Gamma_{c,j}$.

Proof. The relative unitary between adjacent momentum blocks is $\exp\left[i\varphi\frac{I-P_c}{2}\right]$. Its eigenvalues are 1 and $e^{i\varphi}$. For this operator to be proportional to a Pauli operator, these eigenvalues must be either equal or opposite. Hence $e^{i\varphi} = 1$ or $e^{i\varphi} = -1$, which gives $\varphi \equiv 0$ or $\pi \pmod{2\pi}$. For $\varphi = \pi$, the relative unitary is P_c, and the gate is $\Gamma_{c,j}$. □

A broader family is given by momentum-selective qubit rotations (MQRs). For one qubit, let X and Y denote the Pauli matrices and define

$$\mathrm{MQR} = \sum_{\ell\in\mathbb{Z}} R_{\phi_\ell}(\theta_\ell) \otimes |\ell\rangle\langle\ell|, \tag{3.9}$$

$$R_\phi(\theta) = \exp\left[-\frac{i\theta}{2}(\cos\phi\, X + \sin\phi\, Y)\right], \tag{3.10}$$

where $\phi_\ell \in \mathbb{T}$ and $\theta_\ell \in \mathbb{R}$. By Proposition 3.2, such a gate is Clifford if and only if its blocks have the form

$$R_{\phi_\ell}(\theta_\ell) = e^{i[\lambda\ell+\alpha\ell(\ell+1)/2]}P_c^{\,\ell}V_0 \qquad \text{for all } \ell \in \mathbb{Z}, \tag{3.11}$$

for some fixed $V_0 \in \mathrm{Cl}_{1,0}$, fixed Pauli operator P_c, and $\alpha, \lambda \in \mathbb{T}$. Thus, apart from a scalar phase depending quadratically on ℓ, the qubit operation alternates with momentum parity between V_0 and P_cV_0. An MQR outside this form is non-Clifford. A simple Clifford example is $R_0(\pi\ell) = (-iX)^\ell = e^{-i\pi\ell/2}X^\ell$. This is of the form in Eq. (3.11), with a linear scalar phase and momentum-parity-dependent powers of X.

3.3 Angle-dependent phase gates

Angle-dependent phase gates include pure-rotor multiplication operators and phases coupled to a qubit Pauli operator.

3.3.1 Pure-rotor phase gates

Let $g : \mathbb{T}^r \to \mathrm{U}(1)$ be continuous, and define the multiplication operator

$$[M_g\psi](\theta) = g(\theta)\psi(\theta). \tag{3.12}$$

The gate M_g commutes with every $X_R(m)$. Its conjugation of an angle translation is

$$M_g Z_R(\phi) M_g^\dagger = M_{g(\theta)\overline{g(\theta+\phi)}} Z_R(\phi). \tag{3.13}$$

If M_g is Clifford, this factor must be proportional to a torus character for every $\phi \in \mathbb{T}^r$.

Proposition 3.4 (Clifford criterion for pure-rotor phase gates)**.** *The gate M_g belongs to $\mathrm{Cl}_{0,r}$ if and only if there exist $\gamma \in \mathbb{T}$ and $s \in \mathbb{Z}^r$ such that*

$$g(\theta) = e^{i\gamma+is^\intercal\theta} \qquad \textit{for all } \theta \in \mathbb{T}^r. \tag{3.14}$$

Up to a global phase, M_g is the rotor Weyl operator $X_R(s)$.

Proof. Suppose that M_g is Clifford. For each $\phi \in \mathbb{T}^r$, Eq. (3.13) implies

$$g(\theta)\overline{g(\theta+\phi)} = c_\phi e^{is_\phi^\intercal \theta} \tag{3.15}$$

for some $c_\phi \in \mathrm{U}(1)$ and $s_\phi \in \mathbb{Z}^r$.

Translation preserves the winding number of g in every angle variable; complex conjugation reverses it. Hence the left-hand side of Eq. (3.15) has zero winding number in every angle variable. The winding numbers of the character on the right-hand side are the components of s_ϕ, so $s_\phi = 0$.

It follows that $g(\theta+\phi) = \chi(\phi)g(\theta)$ for some continuous function $\chi : \mathbb{T}^r \to \mathrm{U}(1)$. Applying two successive translations gives $\chi(\phi+\phi') = \chi(\phi)\chi(\phi')$, so χ is a continuous character of $\mathbb{T}^r$. Therefore $\chi(\phi) = e^{is^\intercal \phi}$ for some $s \in \mathbb{Z}^r$. Taking $\theta = 0$ gives $g(\theta) = e^{i\gamma + is^\intercal \theta}$ for some $\gamma \in \mathbb{T}$.

Conversely, a function of this form gives $M_g = e^{i\gamma} X_R(s)$, which is a rotor Weyl operator and hence a Clifford gate. □

Let $f \in C(\mathbb{T}^r, \mathbb{R})$, and let M_f be the multiplication operator $[M_f\psi](\theta) = f(\theta)\psi(\theta)$. Define

$$V_f(t) = e^{-itM_f}, \qquad t \in \mathbb{R}. \tag{3.16}$$

Corollary 3.5 (Clifford criterion for real angle potentials)**.** *The gate $V_f(t)$ belongs to $\mathrm{Cl}_{0,r}$ if and only if $t = 0$ or f is constant.*

Proof. The case $t = 0$ gives the identity. Suppose that $t \neq 0$ and that $V_f(t)$ is Clifford. By Proposition 3.4, there exist $\gamma \in \mathbb{T}$ and $s \in \mathbb{Z}^r$ such that

$$e^{-itf(\theta)} = e^{i\gamma + is^\intercal \theta}. \tag{3.17}$$

Because f is a continuous real-valued function on $\mathbb{T}^r$, the left-hand side has zero winding number in every angle variable. The winding numbers of the right-hand side are the components of s. Therefore $s = 0$, and $e^{-itf(\theta)}$ is constant.

It follows that $t\big[f(\theta) - f(0)\big] \in 2\pi\mathbb{Z}$ for all $\theta \in \mathbb{T}^r$. The left-hand side is continuous in θ, while $2\pi\mathbb{Z}$ is discrete. Since $\mathbb{T}^r$ is connected, it must vanish identically. Hence f is constant. The converse is immediate, since a constant f gives only a global phase. □

For one rotor, the cosine-potential gate is

$$K(t) = e^{-itM_{\cos}}, \qquad [M_{\cos}\psi](\theta) = \cos\theta\, \psi(\theta). \tag{3.18}$$

Since $\cos\theta$ is nonconstant, Corollary 3.5 shows that $K(t)$ is non-Clifford for every $t \neq 0$.

3.3.2 Pauli-string–rotor phase gates

For $n, r \geq 1$ and $c \in \mathbb{F}_2^{2n} \setminus \{0\}$, let P_c be the corresponding Hermitian Pauli string. Given $f \in C(\mathbb{T}^r, \mathbb{R})$ and $\tau \in \mathbb{R}$, define the Pauli-string–rotor phase gate (PSR gate)

$$\mathrm{PSR}_{c,f}(\tau) = \exp[-i\tau P_c \otimes M_f]\,. \tag{3.19}$$

The gate restricts to $V_f(\tau)$ and $V_f(-\tau)$ on the $+1$ and -1 eigenspaces of P_c, respectively. All nonidentity Pauli operators are Clifford-conjugate up to sign, so it suffices to analyze one representative.

When $f(\theta) = f_0$ is constant, the rotor dependence drops out and the gate reduces to the Pauli rotation $e^{-i\tau f_0 P_c}$.

Proposition 3.6 (Clifford criterion for PSR gates)**.** *For $\tau = 0$, the gate $\mathrm{PSR}_{c,f}(\tau)$ is the identity. Suppose that $\tau \neq 0$. Then $\mathrm{PSR}_{c,f}(\tau)$ is Clifford if and only if f is constant, say $f(\theta) = f_0$, and $\tau f_0 \in \frac{\pi}{4}\mathbb{Z}$.*

Proof. The case $\tau = 0$ is immediate. Assume that $\tau \neq 0$. Since P_c is nonidentity, choose a Hermitian Pauli string P_d that anticommutes with P_c. By $P_c^2 = I, P_cP_d = -P_dP_c$, we obtain

$$\mathrm{PSR}_{c,f}(\tau)(P_d \otimes I_R)\mathrm{PSR}_{c,f}(\tau)^\dagger = P_d \otimes M_{\cos(2\tau f)} - iP_cP_d \otimes M_{\sin(2\tau f)}, \tag{3.20}$$

where $M_{\cos(2\tau f)}$ and $M_{\sin(2\tau f)}$ denote multiplication by $\cos(2\tau f(\theta))$ and $\sin(2\tau f(\theta))$, respectively.

Suppose first that $\mathrm{PSR}_{c,f}(\tau)$ is Clifford. Then the operator in Eq. (3.20) must be proportional to a single hybrid Weyl operator. The Pauli strings P_d and $-iP_cP_d$ are linearly independent, but a hybrid Weyl operator contains only one qubit Pauli component. Therefore one of the two coefficient functions must vanish identically:

$$\sin\bigl(2\tau f(\theta)\bigr) = 0 \qquad \text{for all } \theta \in \mathbb{T}^r, \tag{3.21}$$

or

$$\cos\bigl(2\tau f(\theta)\bigr) = 0 \qquad \text{for all } \theta \in \mathbb{T}^r. \tag{3.22}$$

In the first case, $2\tau f(\theta) \in \pi\mathbb{Z}$ for all θ, while in the second case, $2\tau f(\theta) \in \frac{\pi}{2} + \pi\mathbb{Z}$ for all θ.

In either case, the continuous function f takes values in a discrete subset of $\mathbb{R}$. Since $\mathbb{T}^r$ is connected, f must be constant. Write $f(\theta) = f_0, a = \tau f_0$.

The PSR gate then reduces to

$$\mathrm{PSR}_{c,f}(\tau) = e^{-iaP_c} \otimes I_R. \tag{3.23}$$

For a Pauli string P_d anticommuting with P_c,

$$e^{-iaP_c} P_d e^{iaP_c} = \cos(2a)P_d - i\sin(2a)P_cP_d. \tag{3.24}$$

For this operator to be proportional to a single Pauli string, one of the two coefficients must vanish. Hence $\sin(2a) = 0$ or $\cos(2a) = 0$. Thus the gate can be Clifford only if $\tau f_0 \in \frac{\pi}{4}\mathbb{Z}$.

Conversely, suppose that $f(\theta) = f_0$ and $\tau f_0 \in (\pi/4)\mathbb{Z}$. Any qubit Pauli string commuting with P_c is unchanged under conjugation by $e^{-i\tau f_0 P_c}$. If a qubit Pauli string instead anticommutes with P_c, Eq. (3.24) shows that it is mapped, up to a scalar phase, to either itself or P_cP_d. Thus $e^{-i\tau f_0 P_c}$ normalizes the qubit Pauli group. Since the gate acts trivially on the rotor subsystem, $\mathrm{PSR}_{c,f}(\tau) = e^{-i\tau f_0 P_c} \otimes I_R \in \mathrm{Cl}_{n,r}$. ☐

For $1 \le j \le n$ and $1 \le k \le r$, choose $P_c = Z_j$ and $f(\theta) = \cos\theta_k$. Then $e^{-i\tau Z_j \otimes \cos\hat{\theta}_k}$ is non-Clifford for every $\tau \neq 0$. On the $Z_j = +1$ and $Z_j = -1$ eigenspaces, its rotor factors are $e^{-i\tau\cos\hat{\theta}_k}$ and $e^{i\tau\cos\hat{\theta}_k}$, respectively.

3.4 Qubit-controlled rotor displacements

The mixed Clifford gate $\Gamma_{c,j}$ uses rotor momentum parity to control a qubit Pauli operation. We now consider the opposite direction of control, in which the qubit controls a rotor displacement. The classification in Sec. 2 already indicates an obstruction: every homomorphism $\mathbb{F}_2^{2n} \longrightarrow \mathbb{Z}^r$ is trivial. A Clifford transformation therefore cannot contain a nonzero qubit-controlled rotor-momentum shift.

For one qubit and one rotor, define the conditional displacement

$$\mathrm{CD}(m,\lambda) = |0\rangle\langle 0| \otimes D_R(m,\lambda) + |1\rangle\langle 1| \otimes D_R(-m,-\lambda), \qquad m \in \mathbb{Z}, \quad \lambda \in \mathbb{T}. \tag{3.25}$$

Proposition 3.7 (Clifford criterion for conditional rotor displacements)**.** *The gate* $\mathrm{CD}(m,\lambda)$ *is Clifford if and only if* $m = 0$ *and* $\lambda \in \frac{\pi}{2}\mathbb{Z} \subset \mathbb{T}$.

Proof. Conjugating the rotor phase operator gives

$$\mathrm{CD}(m,\lambda)(I_Q \otimes Z_R(\phi))\mathrm{CD}(m,\lambda)^\dagger = e^{-im\phi Z} \otimes Z_R(\phi). \tag{3.26}$$

If $m \neq 0$, one can choose ϕ such that $e^{-im\phi Z}$ is not proportional to a Pauli operator. The conjugated operator is then not proportional to a hybrid Weyl operator. Hence $m = 0$ is necessary.

Let c_Z denote the Pauli label for which $P_{c_Z} = Z$. When $m = 0$,

$$\mathrm{CD}(0,\lambda) = [I_Q \otimes Z_R(\lambda)]C_{c_Z,1}(-2\lambda). \tag{3.27}$$

The first factor is a rotor Weyl operator. By Corollary 3.3, the second factor is Clifford if and only if $-2\lambda \equiv 0$ or $\pi \pmod{2\pi}$. Thus $\lambda \in \frac{\pi}{2}\mathbb{Z} \subset \mathbb{T}$, which gives the stated condition. ☐

The following qubit-controlled rotor shift acts nontrivially only on the $|1\rangle$ component:

$$\mathrm{CShift}_{q\to R}(m) = |0\rangle\langle 0|_q \otimes I_R + |1\rangle\langle 1|_q \otimes X_R(m), \qquad m \in \mathbb{Z}. \tag{3.28}$$

Corollary 3.8 (Clifford criterion for qubit-controlled rotor shifts)**.** *The gate* $\mathrm{CShift}_{q\to R}(m)$ *is Clifford if and only if* $m = 0$*.*

Proof. Conjugating the rotor phase operator gives

$$\mathrm{CShift}_{q\to R}(m)(I_Q \otimes Z_R(\phi))\mathrm{CShift}_{q\to R}(m)^\dagger = \big(|0\rangle\langle 0| + e^{-im\phi}|1\rangle\langle 1|\big) \otimes Z_R(\phi). \tag{3.29}$$

If $m \neq 0$, choose ϕ such that $e^{-im\phi} \neq \pm 1$. The qubit factor is then not proportional to a Pauli operator, so the conjugated operator is not proportional to a hybrid Weyl operator. Hence the gate is non-Clifford. For $m = 0$, it is the identity. □

3.5 Summary of Clifford conditions

Table 1 summarizes the Clifford conditions for the parameterized gate families studied above. The standard Clifford gates recalled in Sec. 3.1 are omitted.

Gate family	Clifford condition
G_u	$u(\ell) = e^{i\gamma + i\lambda^\mathsf{T}\ell + if_R(\ell)}$ for some $\gamma \in \mathbb{T}$, $\lambda \in \mathbb{T}^r$, and $R = R^\mathsf{T} \in \mathrm{Mat}_r(\mathbb{T})$.
$\mathcal{V}$ $(r = 1)$	$V_\ell = e^{i[\lambda\ell + \alpha\ell(\ell+1)/2]} P_c{}^\ell V_0$ for some $V_0 \in \mathrm{Cl}_{n,0}$, $c \in \mathbb{F}_2^{2n}$, and $\alpha, \lambda \in \mathbb{T}$.
$C_{c,j}(\varphi)$	$\varphi \equiv 0$ or $\pi \pmod{2\pi}$.
$V_f(t)$	$t = 0$ or f is constant.
$\mathrm{PSR}_{c,f}(\tau)$	$\tau = 0$, or $f(\theta) = f_0$ and $\tau f_0 \in \frac{\pi}{4}\mathbb{Z}$.
$\mathrm{CD}(m, \lambda)$	$m = 0$ and $\lambda \in \frac{\pi}{2}\mathbb{Z} \subset \mathbb{T}$.
$\mathrm{CShift}_{q\to R}(m)$	$m = 0$.

Table 1: Summary of the Clifford conditions for the parameterized gate families considered in this section.

4 Universal control from Clifford and non-Clifford gates

Sec. 3 shows that the cosine potential and the conditional phase at angle $\pi/4$ are non-Clifford. Together with Clifford operations acting separately on the two registers, these two controls give universal control in the strong operator topology.

Define the group of Clifford operations acting separately on the two registers by

$$\mathrm{Cl}^{\mathrm{loc}}_{n,r} := \{U_Q \otimes U_R : U_Q \in \mathrm{Cl}_{n,0},\ U_R \in \mathrm{Cl}_{0,r}\}\,. \tag{4.1}$$

For $n, r \geq 1$, let c_1 be the Pauli label satisfying $P_{c_1} = Z_1$, and let $K_1(t)$ denote the cosine-potential gate in Eq. (3.18) acting on the first rotor. Let

$$G_{n,r} := \left\langle \mathrm{Cl}^{\mathrm{loc}}_{n,r}, K_1(t) : t \in \mathbb{R}, C_{c_1,1}(\pi/4) \right\rangle. \tag{4.2}$$

By Corollary 3.3, $C_{c_1,1}(\pi/4)$ is non-Clifford. Since $\cos\theta$ is nonconstant, Corollary 3.5 shows that $K_1(t)$ is non-Clifford for every $t \neq 0$.

The fixed conditional-phase gate satisfies

$$\left[C_{c_1,1}(\pi/4)\right]^4 = C_{c_1,1}(\pi) = \Gamma_{c_1,1}. \tag{4.3}$$

Since $\mathrm{Cl}^{\mathrm{loc}}_{n,r}$ contains the hybrid Weyl operators, Corollary 2.6 implies that $\mathrm{Cl}^{\mathrm{loc}}_{n,r}$ together with $C_{c_1,1}(\pi)$ generates the full hybrid Clifford group. Lemma 4.4 further shows that $C_{c_1,1}(\pi/4)$ yields a qubit T gate.

4.1 Strong operator topology and finite momentum windows

Throughout this section, $\overline{G}^{\mathrm{s}}$ denotes the closure of G in $\mathrm{U}(\mathcal{H})$ with respect to the strong operator topology.

Definition 4.1 (Universal control in the strong operator topology)**.** A subgroup $G \subseteq \mathrm{U}(\mathcal{H})$ provides universal control in the strong operator topology if $\overline{G}^{\mathrm{s}} = \mathrm{U}(\mathcal{H})$. Thus, for every target unitary $V \in \mathrm{U}(\mathcal{H})$, every finite set of vectors $\psi_1, \ldots, \psi_s \in \mathcal{H}$, and every $\epsilon > 0$, there exists $U \in G$ such that

$$\|(U - V)\psi_j\| < \epsilon, \qquad j = 1, \ldots, s. \tag{4.4}$$

Lemma 4.2 reduces strong density on the full Hilbert space to approximate control on each finite momentum window.

Lemma 4.2 (Finite-window criterion for strong density)**.** *Let $\mathcal{H}$ be separable, and let $\{P_L\}$ be an increasing sequence of finite-rank orthogonal projections satisfying $P_L \longrightarrow I$ strongly. Set $\mathcal{H}_L = P_L\mathcal{H}$. Suppose that for every L, every $V_L \in \mathrm{U}(\mathcal{H}_L)$, and every $\eta > 0$, there exists $W \in \overline{G}^{\mathrm{s}}$ such that W preserves $\mathcal{H}_L$ and*

$$\|W|_{\mathcal{H}_L} - V_L\| < \eta. \tag{4.5}$$

Then G is strongly dense in $\mathrm{U}(\mathcal{H})$.

Appendix C proves Lemma 4.2 by interpolating a target unitary on a sufficiently large finite momentum window and controlling the projected tails. Fig. 2 summarizes the proof strategy.

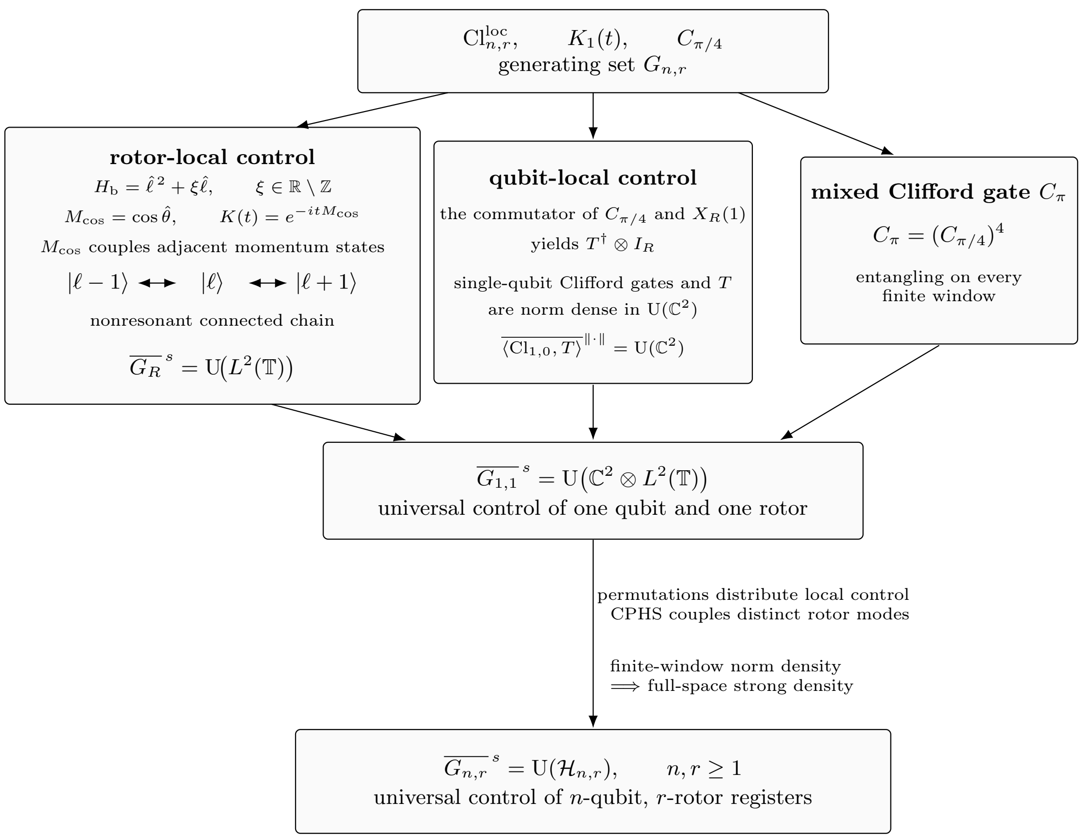

Figure 2: Proof structure for universal control. A biased rotor drift and cosine control yield universal control of a single rotor, while a commutator of $C_{\pi/4}$ with $X_R(1)$ produces $T^\dagger \otimes I_R$ and hence single-qubit control. Combining these local controls with the hybrid entangler $C_\pi = (C_{\pi/4})^4$ gives universal control of one qubit and one rotor. Permutations and CPHS couplings extend the construction to general hybrid registers, while finite-window norm density implies full-space strong density.

4.2 Single-rotor universal control

Let $K(t)$ be the cosine-potential gate defined in Eq. (3.18), and set

$$H_{\mathrm{b}} = \hat{\ell}^2 + \xi\hat{\ell}, \quad \xi \in \mathbb{R} \setminus \mathbb{Z}. \tag{4.6}$$

The drift evolution is a pure-rotor Clifford gate because

$$e^{-isH_{\mathrm{b}}} = \mathrm{QUAD}(-2s) Z_R((1-\xi)s). \tag{4.7}$$

In the momentum basis, $H_{\mathrm{b}}|\ell\rangle = \varepsilon_\ell|\ell\rangle, \varepsilon_\ell = \ell^2 + \xi\ell$, and the nearest-neighbor transition gaps are

$$\varepsilon_{\ell+1} - \varepsilon_\ell = 2\ell + 1 + \xi. \tag{4.8}$$

Moreover, $\langle k|\cos\hat{\theta}|\ell\rangle = \frac{1}{2}\left(\delta_{k,\ell+1} + \delta_{k,\ell-1}\right)$, so the control couples only neighboring momentum levels. Since $\xi \notin \mathbb{Z}$, the spectrum is nondegenerate and the corresponding transition frequencies $|\varepsilon_{\ell+1} - \varepsilon_\ell|$ are pairwise distinct. The nearest-neighbor transitions connect the full momentum lattice and therefore form a nonresonant connectedness chain. Theorem 2.11 of Ref. [28] consequently applies. A related earlier result on approximate state controllability under a stronger spectral assumption is given in Ref. [27].

Theorem 4.3 (Single-rotor universal control)**.** *The group $G_R := \left\langle e^{-isH_{\mathrm{b}}}, K(t) : s,t \in \mathbb{R}\right\rangle$ is strongly dense in $\mathrm{U}(L^2(\mathbb{T}))$.*

Proof. Appendix C verifies the hypotheses of Theorem 2.11 in Ref. [28]. For a constant control amplitude u applied for time τ, the Lie–Trotter formula gives

$$e^{-i\tau(H_{\mathrm{b}} + u\cos\hat{\theta})} = \operatorname{s-lim}_{N\to\infty} \left[e^{-i\tau H_{\mathrm{b}}/N} K\left(\frac{\tau u}{N}\right)\right]^N. \tag{4.9}$$

Hence every evolution generated by a piecewise-constant control belongs to $\overline{G_R}^{\mathrm{s}}$. The cited theorem states that these evolutions can approximate any target unitary simultaneously on any finite set of states. By Definition 4.1, this is precisely the strong density of G_R in $\mathrm{U}(L^2(\mathbb{T}))$. □

4.3 One qubit and one rotor

In this subsection, write $C_\varphi := C_{c_1,1}(\varphi)$.

Lemma 4.4 (A qubit T gate from the conditional phase)**.** *The conditional-phase gate and the unit rotor momentum shift satisfy*

$$(I_Q \otimes X_R(1)) C_\varphi (I_Q \otimes X_R(1)^\dagger) C_\varphi^\dagger = e^{-i\varphi|1\rangle\langle 1|} \otimes I_R. \tag{4.10}$$

For $\varphi = \pi/4$, the right-hand side is $T^\dagger \otimes I_R$, where $T = \mathrm{diag}(1, e^{i\pi/4})$.

Proof. Since $X_R(1)\hat{\ell}X_R(1)^\dagger = \hat{\ell} - I_R$, conjugation by the momentum shift gives $(I_Q \otimes X_R(1))C_\varphi(I_Q \otimes X_R(1)^\dagger) = \left(e^{-i\varphi|1\rangle\langle 1|} \otimes I_R\right) C_\varphi$. Multiplication by $C_\varphi^\dagger$ proves Eq. (4.10). □

The single-qubit Clifford group together with T is dense, up to a global phase, in the single-qubit unitary group [40, 41]. Since scalar phases are contained in $\mathrm{Cl}_{1,0}$, the gates available here generate a norm-dense subgroup of $\mathrm{U}(\mathbb{C}^2)$.

Theorem 4.5 (One-qubit–one-rotor universal control)**.** *The group $G_{1,1}$ defined in Eq. (4.2) is strongly dense in $\mathrm{U}\left(\mathbb{C}^2 \otimes L^2(\mathbb{T})\right)$.*

Proof. The group $G_{1,1}$ contains the single-rotor gates used in Theorem 4.3. Hence its strong closure contains $I_Q \otimes U_R$ for every $U_R \in \mathrm{U}(L^2(\mathbb{T}))$. By Lemma 4.4 and the single-qubit Clifford gates, the same closure contains $U_Q \otimes I_R$ for every $U_Q \in \mathrm{U}(\mathbb{C}^2)$.

For $L \geq 1$, let

$$\mathcal{W}_L = \mathrm{span}\left\{|\ell\rangle : -L \leq \ell \leq L\right\}. \tag{4.11}$$

Every unitary on $\mathcal{W}_L$, extended by the identity on its orthogonal complement, is a rotor-local unitary and therefore belongs to $\overline{G_{1,1}}^{\mathrm{s}}$. Such an extension preserves $\mathcal{W}_L$.

Moreover,

$$C_\pi = \left[C_{\pi/4}\right]^4 = |0\rangle\langle 0| \otimes I_R + |1\rangle\langle 1| \otimes (-1)^{\hat{\ell}} \tag{4.12}$$

also preserves every momentum window. It is entangling on $\mathbb{C}^2 \otimes \mathcal{W}_L$. Indeed, choose an even momentum state $|e\rangle$ and an odd momentum state $|o\rangle$ in the window. Then

$$C_\pi \left[|+\rangle \otimes \frac{|e\rangle + |o\rangle}{\sqrt{2}}\right] = \frac{1}{2}\left[|0\rangle(|e\rangle + |o\rangle) + |1\rangle(|e\rangle - |o\rangle)\right], \tag{4.13}$$

which is an entangled state.

Arbitrary local unitaries together with an entangling bipartite gate generate a norm-dense subgroup of $\mathrm{U}\big(\mathbb{C}^2 \otimes \mathcal{W}_L\big)$ [42, Corollary 2]. Thus every unitary on $\mathbb{C}^2 \otimes \mathcal{W}_L$ can be approximated by elements of $\overline{G_{1,1}}^{\mathrm{s}}$ that preserve this finite window.

The projections onto $\mathbb{C}^2 \otimes \mathcal{W}_L$ increase strongly to the identity. Therefore Lemma 4.2 implies that $G_{1,1}$ is strongly dense in $\mathrm{U}(\mathbb{C}^2 \otimes L^2(\mathbb{T}))$. □

4.4 General hybrid universal control

Theorem 4.6 (General hybrid universal control)**.** *For every $n, r \geq 1$, $\overline{G_{n,r}}^{\mathrm{s}} = \mathrm{U}(\mathcal{H}_{n,r})$, where $G_{n,r}$ is defined in Eq.* (4.2)*.*

Proof. We first obtain arbitrary rotor operations on finite momentum windows. Rotor permutations conjugate $K_1(t)$ to the corresponding cosine-potential gate $K_j(t)$ on any rotor mode j. By Theorem 4.3, the strong closure therefore contains every single-rotor unitary acting on any chosen mode.

For $L \geq 1$, define the r-rotor momentum window

$$\mathcal{W}_{L,r} = \operatorname{span}\left\{|\ell_1, \ldots, \ell_r\rangle : -L \leq \ell_j \leq L \text{ for all } j\right\}. \tag{4.14}$$

Every single-mode unitary on $\operatorname{span}\{|\ell_j\rangle : -L \leq \ell_j \leq L\}$ can be extended by the identity outside that window. Hence the restriction of $\overline{G_{n,r}}^{\mathrm{s}}$ to $\mathcal{W}_{L,r}$ contains arbitrary unitaries on each individual rotor mode.

The pure-rotor Clifford group contains the gates $\mathrm{CPHS}_{ij}(\alpha)$. For $\alpha \not\equiv 0 \pmod{2\pi}$, such a gate is entangling on the finite window. Indeed, on the subspace spanned by $|0\rangle$ and $|1\rangle$ of each of the two modes, it maps $\frac{|0\rangle+|1\rangle}{\sqrt{2}} \otimes \frac{|0\rangle+|1\rangle}{\sqrt{2}}$ to a state whose coefficient matrix is $\begin{pmatrix} 1 & 1 \\ 1 & e^{i\alpha} \end{pmatrix}$. Its determinant is $e^{i\alpha} - 1 \neq 0$, so the resulting state is entangled. Choose CPHS couplings between neighboring rotor modes. These couplings form a connected interaction graph. Applying the bipartite universality criterion of Ref. [42, Corollary 2] iteratively along a spanning tree of this graph, together with arbitrary single-mode unitaries, gives a norm-dense subgroup of $\mathrm{U}(\mathcal{W}_{L,r})$. All these gates preserve the finite momentum window.

We next consider the qubit register. By Lemma 4.4, the available gates produce a T gate on the first qubit. Qubit Clifford operations include qubit permutations, so a T gate is available on every qubit. The n-qubit Clifford group together with these T gates generates a norm-dense subgroup of $\mathrm{U}\big((\mathbb{C}^2)^{\otimes n}\big)$.

It remains to couple the two registers. Since $C_{c_1,1}(\pi) = \left[C_{c_1,1}(\pi/4)\right]^4$, the group $G_{n,r}$ contains the mixed Clifford gate $C_{c_1,1}(\pi)$. This gate preserves every finite momentum window and is entangling across the partition $(\mathbb{C}^2)^{\otimes n} \otimes \mathcal{W}_{L,r}$.

For example, fix all qubits except the first and all rotors except the first, and choose one even and one odd momentum state of the first rotor. The restriction then contains the entangling action exhibited in Eq. (4.13).

We have therefore obtained arbitrary unitaries on the qubit register, arbitrary unitaries on the finite rotor window, and an entangling gate between the two registers. The finite-dimensional bipartite universality criterion consequently gives a norm-dense subgroup of $\mathrm{U}\left((\mathbb{C}^2)^{\otimes n} \otimes \mathcal{W}_{L,r}\right)$ for every L. These operations preserve the finite-dimensional subspace $(\mathbb{C}^2)^{\otimes n} \otimes \mathcal{W}_{L,r}$.

The projections onto $(\mathbb{C}^2)^{\otimes n} \otimes \mathcal{W}_{L,r}$ increase strongly to the identity. Lemma 4.2 therefore implies $\overline{G_{n,r}}^{\mathrm{s}} = \mathrm{U}(\mathcal{H}_{n,r})$. □

Remark 4.7 (Boundary cases)*.* If $r = 0$ and $n \geq 1$, the n-qubit Clifford group together with a single-qubit T gate generates a norm-dense subgroup of $\mathrm{U}((\mathbb{C}^2)^{\otimes n})$. If $n = 0$ and $r \geq 1$, the argument above restricted to the rotor register gives $\overline{\langle \mathrm{Cl}_{0,r}, K_1(t) : t \in \mathbb{R}\rangle}^{\mathrm{s}} = \mathrm{U}(L^2(\mathbb{T}^r))$. The case $n = r = 0$ is one-dimensional.

Logical operations in the applications. Secs. 5–7 also use CShift and $\mathcal{O}_U$ as logical operations. Theorem 4.6 places these operations in the strong closure of $G_{n,r}$.

5 Gate realization of a compact $U(1)$ gauge–matter model

In compact $U(1)$ gauge–matter theory, each oriented link carries a compact gauge angle and an integer-valued electric flux, and each matter site carries a binary occupation. Links are therefore represented by rotors and matter sites by qubits. For a lattice with N_s matter sites and N_ℓ oriented links, the corresponding hybrid register is

$$\mathcal{H}_{\mathrm{GM}} = \left(\mathbb{C}^2\right)^{\otimes N_s} \otimes L^2(\mathbb{T})^{\otimes N_\ell}. \tag{5.1}$$

Gauss's law couples the two registers at the level of the physical state space. The four Hamiltonian terms fall into the gate families introduced in Sec. 3: the electric term is generated by rotor momentum quadratics, the magnetic term by a periodic angle potential, and the mass term by qubit-local operations. The gauge-covariant hopping term changes matter occupation together with an integer shift of the link flux, placing it in the qubit-to-rotor control direction studied in Sec. 3.4.

We use the standard Hamiltonian formulation of compact $U(1)$ lattice gauge theory introduced by Kogut and Susskind [11]. Its separation into matter degrees of freedom and integer-flux gauge links is also the starting point of recent hybrid quantum simulation proposals, including oscillator–qubit, qubit–qumode, and superconducting phase–charge implementations [7, 12, 13]. Broader reviews of quantum simulation methods for lattice gauge theories can be found in Refs. [43, 44].

5.1 Rotor links, matter qubits, and Gauss's law

Let $e = (a, b)$ denote a link oriented from site a to site b. Its gauge field is a rotor with

$$U_e = e^{i\hat{\theta}_e} = X_R(1), \qquad E_e = \hat{\ell}_e, \qquad [E_e, U_{e'}] = \delta_{ee'} U_{e'}. \tag{5.2}$$

Thus $U_e|\ell_e\rangle = |\ell_e+1\rangle$. For the oriented plaquettes, let $B = (B_{pe})$ be the boundary matrix, with $B_{pe} \in \{0, \pm 1\}$, and set

$$U_p = \prod_e U_e^{B_{pe}} = e^{i\Phi_p}, \qquad \Phi_p = \sum_e B_{pe}\hat{\theta}_e. \tag{5.3}$$

One qubit at site n stores the occupation

$$\hat{n}_n = \frac{I + Z_n}{2}. \tag{5.4}$$

With this Pauli convention, $|0\rangle$ is occupied and $|1\rangle$ is empty. On a two-dimensional square lattice, let $\eta_n = (-1)^{n_x+n_y}$, $b_n = \frac{1-\eta_n}{2}$ and

$$\rho_n = \hat{n}_n - b_n + q_n^{\mathrm{ext}}, \qquad q_n^{\mathrm{ext}} \in \mathbb{Z}. \tag{5.5}$$

Here q_n^{ext} is a fixed external charge.

Let $D \in \mathbb{Z}^{N_s \times N_\ell}$ be the oriented site–link incidence matrix, with

$$D_{ne} = \begin{cases} +1, & \text{if site } n \text{ is the tail of } e, \\ -1, & \text{if site } n \text{ is the head of } e, \\ 0, & \text{otherwise.} \end{cases} \tag{5.6}$$

The Gauss-law generators are

$$G_n = \sum_e D_{ne} E_e - \rho_n, \qquad \mathcal{H}_{\mathrm{phys}} = \bigcap_n \ker G_n. \tag{5.7}$$

Because each oriented link has one tail and one head, $\mathbf{1}^\intercal D = 0$. Every physical state therefore satisfies the global Gauss constraint

$$\sum_n \left(\hat{n}_n - b_n + q_n^{\mathrm{ext}}\right)|\psi\rangle = 0, \qquad |\psi\rangle \in \mathcal{H}_{\mathrm{phys}}. \tag{5.8}$$

The Gauss-law constraint couples the flux divergence on the rotor links incident on site n to the matter-qubit charge ρ_n. The physical subspace consists of matter occupations and link-flux configurations satisfying $G_n = 0$ at every site.

Let $g > 0$ denote the gauge coupling, $a_{\rm lat} > 0$ the lattice spacing, $m_0 \in \mathbb{R}$ the staggered mass parameter, and $\kappa \in \mathbb{R}$ the hopping amplitude. The gauge–matter Hamiltonian is

$$H = H_E + H_B + H_M + H_K, \tag{5.9}$$

where

$$H_E = \frac{g^2}{2} \sum_e E_e^2, \qquad H_B = \frac{1}{g^2 a_{\rm lat}^2} \sum_p (1 - \cos \Phi_p), \tag{5.10}$$

$$H_M = m_0 \sum_n \eta_n \hat{n}_n, \qquad H_K = \sum_{e=(a,b)} H_{K,ab}. \tag{5.11}$$

Let Ψ_n and $\Psi_n^\dagger$ denote the fermionic annihilation and creation operators at site n. For a link $e = (a, b)$ oriented from site a to site b, let $\zeta_{ab} = e^{i\delta_{ab}}$ denote the fixed hopping phase. The gauge-covariant hopping term is

$$H_{K,ab} = \frac{\kappa}{2} \left(\zeta_{ab} \Psi_a^\dagger U_{ab} \Psi_b + \zeta_{ab}^* \Psi_b^\dagger U_{ab}^\dagger \Psi_a \right). \tag{5.12}$$

The direction-dependent phases in a Kogut–Susskind discretization are particular choices of ζ_{ab} [45, 46].

Choose a snake ordering $s(n)$ of the matter sites. The Jordan–Wigner transformation [47] introduces

$$\Pi_m^{\rm JW} = (-1)^{\hat{n}_m} = -Z_m, \qquad S_{ab} = \prod_{m:\, \min(s(a),s(b)) < s(m) < \max(s(a),s(b))} \Pi_m^{\rm JW}, \tag{5.13}$$

and gives

$$H_{K,ab} = \frac{\kappa}{2} \left(\zeta_{ab} \sigma_a^+ S_{ab} U_{ab} \sigma_b^- + \zeta_{ab}^* \sigma_b^+ S_{ab} U_{ab}^\dagger \sigma_a^- \right). \tag{5.14}$$

For adjacent sites in the chosen ordering, $S_{ab} = I$, so Eq. (5.14) reduces to a two-qubit exchange coupled to the link momentum shift U_{ab}. Expanding the ladder operators gives the form used below:

$$H_{K,ab} = \frac{\kappa}{4} \Big[\cos(\hat{\theta}_{ab} + \delta_{ab})(X_a S_{ab} X_b + Y_a S_{ab} Y_b) + \sin(\hat{\theta}_{ab} + \delta_{ab})(X_a S_{ab} Y_b - Y_a S_{ab} X_b) \Big]. \tag{5.15}$$

Appendix D.1 verifies that each of H_E, H_B, H_M, and H_K commutes with every G_n and derives the Pauli decomposition in Eq. (5.15). For each hopping term, the changes in matter charge and electric flux cancel in the Gauss-law generators at both endpoints.

5.2 Gate realization of the Hamiltonian

Electric term. The electric evolution on one link is a pure-rotor Clifford gate:

$$e^{-i\Delta t\, g^2 \hat{\ell}_e^2/2} = Z_{R,e}(g^2 \Delta t/2)\, \mathrm{QUAD}_e(-g^2 \Delta t). \tag{5.16}$$

The Weyl phase $Z_{R,e}(g^2\Delta t/2)$ compensates for the $\ell_e(\ell_e + 1)/2$ convention in the definition of QUAD.

Magnetic term. For a plaquette p, the boundary vector $b_p = (B_{pe})_e$ is a primitive integer vector. Choose $A_p \in \mathrm{GL}(N_\ell, \mathbb{Z})$ such that $A_p b_p = e_1$. Here $K_1(t)$ denotes the cosine-potential gate in Eq. (3.18) acting on the first rotor mode. The plaquette evolution is

$$e^{-i\Delta t(1-\cos\Phi_p)/(g^2 a_{\rm lat}^2)} = e^{-i\Delta t/(g^2 a_{\rm lat}^2)} U_{A_p}^\dagger K_1\!\left(-\frac{\Delta t}{g^2 a_{\rm lat}^2} \right) U_{A_p}. \tag{5.17}$$

Indeed, $U_{A_p}^\dagger X_R(e_1) U_{A_p} = X_R(b_p)$, so conjugation maps the cosine acting on the first rotor mode to $\cos \Phi_p$. This realizes the plaquette evolution using a rotor automorphism and the cosine-potential gate. The plaquette boundary vector satisfies $D b_p = 0$, the lattice identity that the boundary of a boundary vanishes, so the evolution preserves every Gauss-law constraint.

Mass term. Using $\hat{n}_n = (I + Z_n)/2$, the mass evolution is

$$e^{-i\Delta t H_M} = \exp\left(-\frac{i\Delta t\, m_0}{2}\sum_n \eta_n\right)\prod_n e^{-i\Delta t\, m_0 \eta_n Z_n/2}. \tag{5.18}$$

Apart from the displayed global phase, this term requires only qubit-local rotations.

Hopping term: controlled-shift realization. On the full rotor Hilbert space, define

$$H_{ab}^{(q)}(\delta_{ab}) = \frac{\kappa}{2}\left(e^{i\delta_{ab}}\sigma_a^+ S_{ab}\sigma_b^- + e^{-i\delta_{ab}}\sigma_b^+ S_{ab}\sigma_a^-\right). \tag{5.19}$$

Consider either of the following controlled shifts:

$$V_{ab}^{(a)} = \mathrm{CShift}_{a\to e}(-1), \qquad V_{ab}^{(b)} = \mathrm{CShift}_{b\to e}(1). \tag{5.20}$$

Let V_{ab} denote either $V_{ab}^{(a)}$ or $V_{ab}^{(b)}$. Then $H_{K,ab} = V_{ab}H_{ab}^{(q)}(\delta_{ab})V_{ab}^\dagger$, and therefore

$$e^{-i\tau H_{K,ab}} = V_{ab}e^{-i\tau H_{ab}^{(q)}(\delta_{ab})}V_{ab}^\dagger. \tag{5.21}$$

For $\delta_{ab} = 0$, define $P_1 = X_a S_{ab} X_b$, $\quad P_2 = Y_a S_{ab} Y_b$. These Pauli strings commute, and $H_{ab}^{(q)}(0) = \frac{\kappa}{4}(P_1 + P_2)$. Moreover, with $R_a(\delta) = e^{i\delta Z_a/2}$, we have $H_{ab}^{(q)}(\delta) = R_a(\delta)H_{ab}^{(q)}(0)R_a(\delta)^\dagger$. Consequently,

$$e^{-i\tau H_{ab}^{(q)}(\delta_{ab})} = R_a(\delta_{ab})e^{-i\tau\kappa P_1/4}e^{-i\tau\kappa P_2/4}R_a(\delta_{ab})^\dagger. \tag{5.22}$$

Together, Eqs. (5.21) and (5.22) implement the gauge-invariant hopping evolution. Appendix D.2 derives the controlled-shift conjugation identities and the commuting-Pauli decomposition underlying this realization.

Hopping term: PSR realization. Eq. (5.15) writes $H_{K,ab}$ as a sum of four Pauli-string–rotor angle-potential terms. The exponential of each term is a PSR gate of the form defined in Eq. (3.19). The sine potentials can be obtained from the cosine potential by a rotor phase translation.

The controlled-shift realization preserves the Gauss-law subspace. Finite-order product formulas built from the four PSR factors in Eq. (5.15) do not generally share this invariance [48].

5.3 Finite-flux truncation

Numerical calculations replace each link Hilbert space by

$$\mathcal{H}_{e,L} = \mathrm{span}\{|\ell\rangle : -L \le \ell \le L\}, \qquad \Pi_L = \sum_{\ell=-L}^{L}|\ell\rangle\langle\ell|. \tag{5.23}$$

The projected shift

$$U_{e,L} := \Pi_L U_e \Pi_L$$

acts as the ordinary link shift on every nonboundary momentum state but annihilates the upper-boundary state:

$$U_{e,L}|\ell\rangle = \begin{cases} |\ell+1\rangle, & -L \le \ell < L, \\ 0, & \ell = L. \end{cases}$$

Consequently,

$$U_{e,L}^\dagger U_{e,L} = I_{e,L} - |L\rangle\langle L|, \qquad U_{e,L}U_{e,L}^\dagger = I_{e,L} - |-L\rangle\langle -L|. \tag{5.24}$$

Thus $U_{e,L}$ is a nonunitary hard-wall truncation in which transitions leaving the selected electric-flux window are omitted.

The discrepancy from the full rotor shift is supported entirely at the cutoff boundary. For a normalized state $|\psi\rangle \in \mathcal{H}_{e,L}$,

$$\begin{aligned} \|(U_e - U_{e,L})|\psi\rangle\|^2 &= |\langle L|\psi\rangle|^2, \\ \left\|(U_e^\dagger - U_{e,L}^\dagger)|\psi\rangle\right\|^2 &= |\langle -L|\psi\rangle|^2. \end{aligned} \tag{5.25}$$

Eq. (5.25) identifies the occupations of $|L\rangle$ and $|-L\rangle$ with the squared norm errors of the projected forward and backward shifts, respectively.

Adding the boundary transition $|L\rangle \mapsto |-L\rangle$ restores unitarity. Define

$$\widetilde{U}_{e,L} = \sum_{\ell=-L}^{L-1} |\ell+1\rangle\langle\ell| + |-L\rangle\langle L|, \qquad d = 2L+1. \tag{5.26}$$

The operator $\widetilde{U}_{e,L}$ cyclically permutes the $d = 2L+1$ momentum states and is therefore unitary. For

$$E_{e,L} = \Pi_L E_e \Pi_L,$$

direct action on the momentum basis gives

$$[E_{e,L}, \widetilde{U}_{e,L}] = \widetilde{U}_{e,L} - d|-L\rangle\langle L|. \tag{5.27}$$

The operators $U_{e,L}$ and $\widetilde{U}_{e,L}$ agree on every transition with $\ell < L$. Their only difference is the added wraparound transition $|L\rangle \mapsto |-L\rangle$, which produces the rank-one correction in Eq. (5.27).

The projected shift preserves the ordinary integer-flux translation away from the boundary and is nonunitary; the cyclic completion is unitary. In the full hopping term, a unit change of the endpoint matter charges is accompanied by a unit change of the link flux. The cyclic wraparound changes the link flux by $-2L$ while the endpoint matter charges still change by one unit, so it violates the original integer-valued Gauss's law at the cutoff boundary.

In the cutoff calculation below, we use the hard-wall projected Hamiltonian: hopping and plaquette transitions whose final flux lies outside the window are omitted. The resulting Hamiltonian remains Hermitian and preserves the finite Gauss-law basis. Its agreement with the full rotor model is controlled by the weight on $|E_e| = L$, as quantified by Eq. (5.25). Appendix D.3 derives this boundary-supported shift error and compares the projected shift with its cyclic completion. We monitor this boundary occupation together with the physical observables in Sec. 5.4.

5.4 Finite-flux benchmarks

Flux-cutoff dependence is computed by diagonalizing the Hamiltonian in the joint kernel of the Gauss-law generators for an open 2×1 plaquette strip with six sites, seven links, and two plaquettes. The 2×1 strip is the smallest open geometry containing two plaquettes and therefore supports the connected correlator C_{12}. At $L = 6$, the corresponding physical basis has dimension 2350.

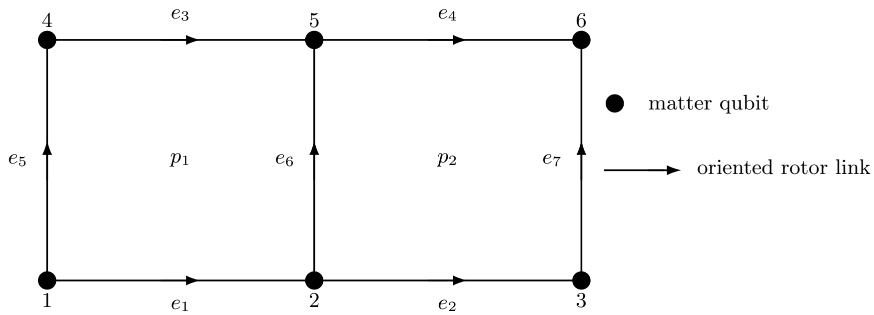

Figure 3: Open 2×1 gauge–matter strip used in the finite-flux benchmarks. Matter qubits occupy the six sites, $U(1)$ rotors occupy the seven oriented links, and p_1 and p_2 denote the two plaquettes. Horizontal links are oriented to the right and vertical links upward, with the site and link ordering used in the calculation listed in Appendix D.4.

We set $q_n^{\text{ext}} = 0$, $a_{\text{lat}} = 1$, $\kappa = 1$, $m_0 = 1.5$, and $\zeta_{ab} = 1$. The flux cutoffs are $L = 1, 2, 3, 4, 6$, and the scan uses 55 logarithmically spaced values of g^{-2} from 10^{-2} to 10. Here $\sum_n b_n = 3$, so Eq. (5.8) fixes the total matter occupation to $\sum_n \hat{n}_n = 3$. Using the finite basis, matrix elements, and sparse diagonalization specified in Appendix D.4, we evaluate

$$\overline{W} = \frac{1}{N_p} \sum_p \langle \cos \Phi_p \rangle, \qquad \Delta = \mathcal{E}_1 - \mathcal{E}_0, \qquad \langle E^2 \rangle_{\text{link}} = \frac{1}{N_\ell} \sum_e \langle E_e^2 \rangle. \tag{5.28}$$

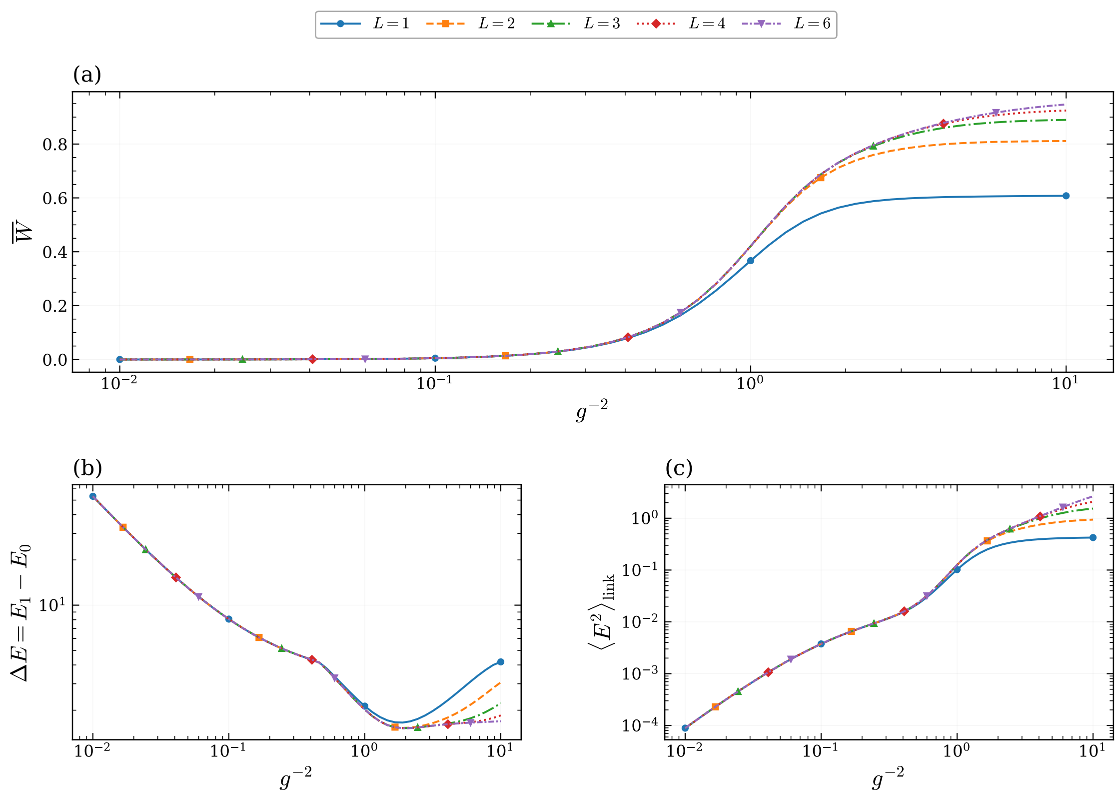

Figure 4: Ground-state results for the open 2×1 gauge–matter model. (a) Average plaquette cosine $\overline{W}$. (b) Spectral gap $\Delta = \mathcal{E}_1 - \mathcal{E}_0$. (c) Link-averaged squared electric flux $\langle E^2 \rangle_{\text{link}}$. The curves correspond to flux cutoffs $L = 1, 2, 3, 4, 6$. The vertical dotted line marks $g^{-2} = 1$.

At small g^{-2}, the electric term suppresses nonzero link flux, and $\overline{W}$ remains close to zero. As g^{-2} increases, the plaquette term becomes more important and the ground-state flux distribution broadens. The spectral gap Δ develops a minimum near $g^{-2} \sim 2$, in the same crossover region where $\overline{W}$ rises rapidly and the link-flux distribution broadens. Over the sampled interval $g^{-2} \leq 1$, the maximum absolute $L = 4$ versus $L = 6$ differences in $\overline{W}$, Δ, and $\langle E^2 \rangle_{\text{link}}$ are 1.34×10^{-8}, 4.69×10^{-10}, and 7.23×10^{-9}, respectively. The separation between the $L = 4$ and $L = 6$ curves increases toward $g^{-2} = 10$ as more weight approaches the cutoff boundary.

To probe the coupled qubit–rotor dynamics, we evolve the zero-flux strong-coupling state

$$|\Omega_{\text{sc}}\rangle = |\mathbf{o} = \mathbf{b}; E = \mathbf{0}\rangle, \qquad |\psi_L(t)\rangle = e^{-itH_L}|\Omega_{\text{sc}}\rangle. \tag{5.29}$$

This state satisfies $DE = \mathbf{o} - \mathbf{b} = \mathbf{0}$. We take $g^{-2} = 1$, $m_0 = 1.5$, $\kappa = 1$, $0 \leq t \leq 8$, and $L = 1, 2, 3, 4$.

We monitor

$$\begin{aligned}
\overline{W}(t) &= \frac{1}{N_p} \sum_p \langle \cos \Phi_p \rangle_t, \\
C_{12}(t) &= \langle \cos \Phi_1 \cos \Phi_2 \rangle_t - \langle \cos \Phi_1 \rangle_t \langle \cos \Phi_2 \rangle_t, \\
I_M(t) &= -\sum_n \eta_n \langle \hat{n}_n \rangle_t, \\
\overline{p}_{\partial L}(t) &= \frac{1}{N_\ell} \sum_e \left\langle \mathbf{1}_{\{|E_e| = L\}} \right\rangle_t.
\end{aligned} \tag{5.30}$$

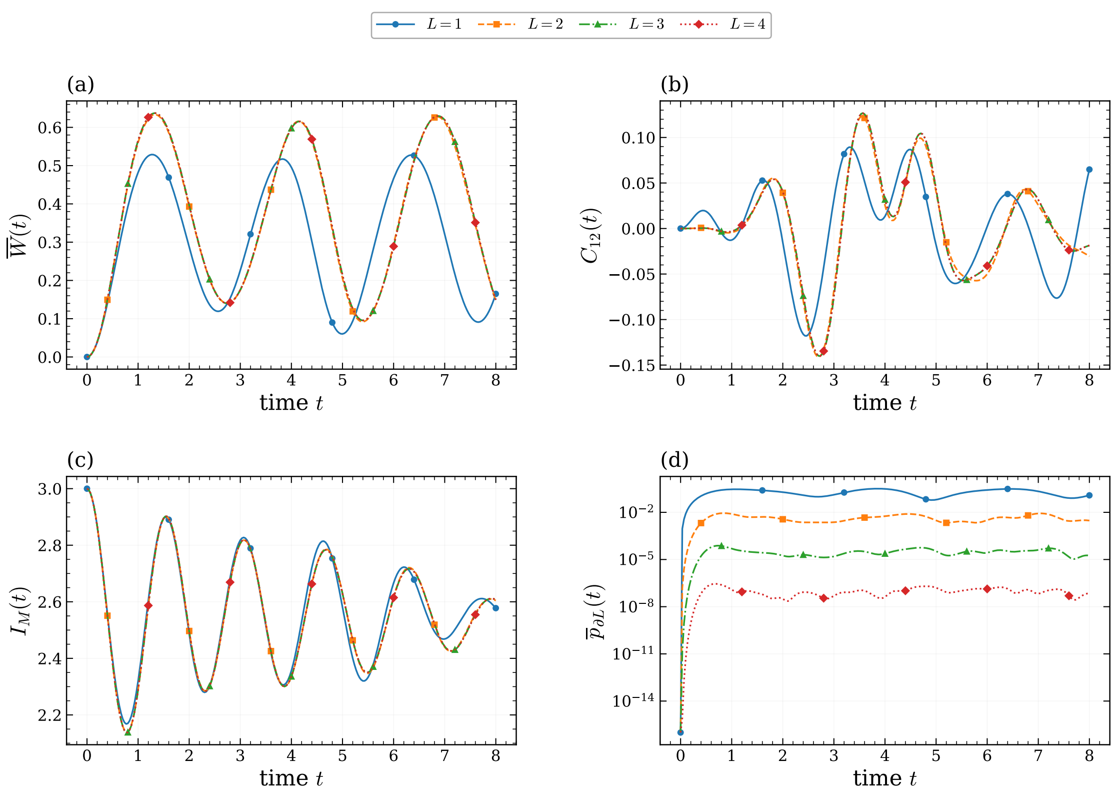

Figure 5: Gauge-invariant real-time dynamics of the open 2×1 gauge–matter model following evolution from the zero-flux strong-coupling reference state. The parameters are $g^{-2} = 1$, $m_0 = 1.5$, and $\kappa = 1$. (a) Average plaquette cosine $\overline{W}(t)$. (b) Connected two-plaquette correlation $C_{12}(t)$. (c) Staggered matter imbalance $I_M(t)$. (d) Link-averaged cutoff-boundary occupation $\overline{p}_{\partial L}(t)$. The first two panels probe the rotor gauge observables, panel (c) probes the matter-qubit dynamics, and panel (d) diagnoses the finite-flux truncation.

Starting from the zero-flux state, the plaquette expectation $\overline{W}(t)$ develops an oscillatory response, while the connected correlation $C_{12}(t)$ becomes nonzero. The evolution therefore generates both local magnetic coherence and correlations between the two rotor plaquettes. At the same time, the matter imbalance $I_M(t)$ departs from its initial value and undergoes oscillations. Since the electric and magnetic terms act only on the rotor register and the mass term is diagonal in the occupation basis, this redistribution of matter occupation is generated by the gauge-covariant hopping term H_K.

On the 241 sampled times, the maximum $L = 3$ versus $L = 4$ differences in $\overline{W}(t)$, $C_{12}(t)$, and $I_M(t)$ are 9.99×10^{-5}, 2.28×10^{-4}, and 3.54×10^{-5}, respectively. The maximum $\overline{p}_{\partial L}(t)$ decreases from 7.60×10^{-5} at $L = 3$ to 2.84×10^{-7} at $L = 4$.

6 Rotor quantum phase estimation and probe-state design

In rotor quantum phase estimation, a single rotor serves as the phase register for an n-qubit target. Let $U \in \mathrm{U}(\mathcal{H}_{n,0})$ have an eigenstate satisfying

$$U|\psi_\varphi\rangle = e^{i\varphi}|\psi_\varphi\rangle, \qquad |\psi_\varphi\rangle \in \mathcal{H}_{n,0}. \tag{6.1}$$

Standard QPE stores the phase in a finite register and applies an inverse quantum Fourier transform before measurement [41, 49, 50]. With a rotor phase register and direct angle measurement, the inverse transform can be omitted. The rotor momentum label $\ell \in \mathbb{Z}$ indexes the controlled powers $U^{-\ell}$, and phase kickback produces the character $e^{-i\ell\varphi}$. Under $\mathbb{Z} \longleftrightarrow \mathbb{T}$, this character translates the conjugate angle distribution by φ, so the eigenphase can be read directly from an angle measurement.

Bosonic modes have previously been used as phase registers [51, 52], and the rotor version with momentum-controlled powers and direct angle readout was proposed in Ref. [15]. Here we take this rotor protocol as the starting point and allow an arbitrary initial probe state. Its momentum amplitudes determine the shape of the translated angle distribution, and therefore control both the estimation error and the range of powers $U^{-\ell}$ required by the protocol.

This makes probe preparation the main resource question. At fixed momentum support, the optimum is the cosine-window probe used below [29, 30]. At fixed mean kinetic energy, the optimum is a Mathieu probe [31]. Sec. 6.2 compares these probes with the uniform finite-momentum state and relates their estimation error directly to the corresponding rotor resources.

6.1 Phase kickback and direct-angle readout

For a normalized rotor probe

$$|\eta\rangle_R = \sum_{\ell\in\mathbb{Z}} a_\ell|\ell\rangle_R, \qquad \sum_{\ell\in\mathbb{Z}} |a_\ell|^2 = 1, \tag{6.2}$$

define the momentum-controlled power operation

$$\mathcal{O}_U := \sum_{\ell\in\mathbb{Z}} U^{-\ell} \otimes |\ell\rangle\langle\ell|. \tag{6.3}$$

The sign convention is chosen so that, with the angle-state convention of Sec. 2.1, the measured angle distribution is centered at $\theta = \varphi$.

Phase kickback gives

$$\mathcal{O}_U\big(|\psi_\varphi\rangle \otimes |\eta\rangle_R\big) = |\psi_\varphi\rangle \otimes |\eta_\varphi\rangle_R, \qquad |\eta_\varphi\rangle_R = \sum_{\ell\in\mathbb{Z}} a_\ell e^{-i\ell\varphi}|\ell\rangle_R. \tag{6.4}$$

The generalized angle states define the periodic angle measurement

$$E_\theta(d\theta) = |\theta\rangle\langle\theta|\, d\theta, \qquad \int_0^{2\pi} E_\theta(d\theta) = I_R. \tag{6.5}$$

Its probability density after phase kickback is

$$p_\eta(\theta \mid \varphi) = \frac{1}{2\pi}\left|\sum_{\ell\in\mathbb{Z}} a_\ell e^{i\ell(\theta-\varphi)}\right|^2 = p_\eta(\theta-\varphi \mid 0). \tag{6.6}$$

Eq. (6.6) shows that phase kickback translates the angle profile without changing its shape. The amplitudes a_ℓ determine the localization and tails of the direct-angle distribution, and the largest occupied $|\ell|$ determines the required range of controlled powers.

The uniform momentum superposition provides the baseline. Set $d = 2^s$ and use the finite rotor momentum code

$$\mathcal{M}_d^{(0)} = \mathrm{span}\{|0\rangle_R, \ldots, |d-1\rangle_R\}. \tag{6.7}$$

Finite rotor momentum encodings have also been considered in Ref. [8].

The rotor analogue of the uniform qubit phase-register state is

$$|+_d\rangle_R = \frac{1}{\sqrt{d}} \sum_{\ell=0}^{d-1} |\ell\rangle_R. \tag{6.8}$$

Applying Eq. (6.3) gives

$$\mathcal{O}_U \big(|\psi_\varphi\rangle \otimes |+_d\rangle_R \big) = |\psi_\varphi\rangle \otimes |\chi_d(\varphi)\rangle_R, \tag{6.9}$$

where

$$|\chi_d(\varphi)\rangle_R = \frac{1}{\sqrt{d}} \sum_{\ell=0}^{d-1} e^{-i\ell\varphi} |\ell\rangle_R. \tag{6.10}$$

Indeed, the momentum component $|\ell\rangle_R$ applies $U^{-\ell}$ to the target eigenstate and therefore acquires the phase $e^{-i\ell\varphi}$.

Using the angle–momentum Fourier relation in Eq. (2.3), the angle-space amplitude after phase kickback is

$$\langle\theta|\chi_d(\varphi)\rangle_R = \frac{1}{\sqrt{2\pi d}} \sum_{\ell=0}^{d-1} e^{i\ell(\theta-\varphi)}. \tag{6.11}$$

The corresponding direct-angle probability density is

$$p_d(\theta \mid \varphi) = \frac{1}{2\pi d} \left| \sum_{\ell=0}^{d-1} e^{i\ell(\theta-\varphi)} \right|^2 = \frac{1}{2\pi d} \frac{\sin^2[d(\theta-\varphi)/2]}{\sin^2[(\theta-\varphi)/2]}. \tag{6.12}$$

Eq. (6.12) is a shifted periodic Fejér kernel. Its maximum is centered at $\theta = \varphi$, and its first zeros occur at circular distance $2\pi/d$. As $d \to \infty$, the probability measures $p_d(\theta \mid \varphi) d\theta$ converge weakly to the Dirac measure at φ. Appendix E.1 gives the calculation.

The eigenphase can therefore be recovered by measuring the rotor angle directly, without applying a coherent Fourier transform to the phase register. The corresponding rotor protocol is shown in Fig. 6.

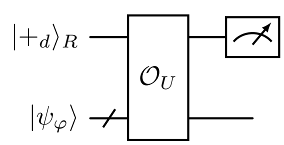

Figure 6: Rotor quantum phase estimation with direct angle readout. The momentum-controlled power operation translates the angle distribution of the rotor phase register by the target eigenphase φ, which is then read out by an angle measurement.

For the uniform probe above, Fourier processing followed by momentum measurement recovers the standard discrete QPE distribution. Direct angle measurement requires no such coherent Fourier stage.

6.2 Probe optimization under momentum and energy constraints

Two resource constraints determine the probe optimization: finite momentum support and fixed mean rotor energy.

For the general probe in Eq. (6.2), define its mean resultant length by

$$R(\eta) := |\langle\eta|X_R(1)|\eta\rangle| = \left| \sum_{\ell\in\mathbb{Z}} a_\ell a_{\ell+1}^* \right|, \tag{6.13}$$

and use the circular variance

$$V(\eta) := 1 - R(\eta). \tag{6.14}$$

The modulus makes $R(\eta)$ independent of the angular origin. After centering the probe at $\theta = 0$, $V(\eta) = \int_0^{2\pi}[1-\cos(\theta-\varphi)]p_\eta(\theta \mid \varphi)\,d\theta$. For a narrowly localized distribution,

$$1-\cos(\theta-\varphi) \simeq \frac{1}{2}(\theta-\varphi)^2, \tag{6.15}$$

so the angular error scale is

$$\Delta_\phi \simeq \sqrt{2V}. \tag{6.16}$$

The Holevo variance $R(\eta)^{-2}-1$ and $V(\eta) = 1-R(\eta)$ are both strictly decreasing functions of $R(\eta)$, so they select the same optimal probe states.

We also use the dimensionless rotor kinetic energy

$$E_R(\eta) := \langle\eta|\hat{\ell}^2|\eta\rangle = \sum_{\ell\in\mathbb{Z}} \ell^2|a_\ell|^2. \tag{6.17}$$

For probes with finite momentum support, the largest occupied $|\ell|$ determines the required range of controlled powers; E_R measures the rotor kinetic-energy resource.

Uniform momentum superposition. For comparison, consider the centered uniform state

$$|\eta^{(L)}_{\mathrm{unif}}\rangle_R = \frac{1}{\sqrt{2L+1}} \sum_{\ell=-L}^{L} |\ell\rangle_R. \tag{6.18}$$

For Eq. (6.18),

$$R_{\mathrm{unif}} = \frac{2L}{2L+1}, \qquad V_{\mathrm{unif}} = \frac{1}{2L+1}. \tag{6.19}$$

The corresponding energy is

$$E_{\mathrm{unif}} = \frac{1}{2L+1} \sum_{\ell=-L}^{L} \ell^2 = \frac{L(L+1)}{3}. \tag{6.20}$$

Since

$$2L+1 = \sqrt{12E_{\mathrm{unif}}+1}, \tag{6.21}$$

the circular variance obeys

$$V_{\mathrm{unif}} = \frac{1}{\sqrt{12E_{\mathrm{unif}}+1}} = O(E_{\mathrm{unif}}^{-1/2}). \tag{6.22}$$

The corresponding error scale is therefore $\Delta_{\mathrm{unif}} = O(E_{\mathrm{unif}}^{-1/4})$.

This scaling reflects the slowly decaying sidelobes of the uniform finite-momentum profile. Its central lobe still has angular width $O(1/L) = O(E_{\mathrm{unif}}^{-1/2})$. The weaker scaling in Eq. (6.22) arises because the circular variance is sensitive to probability away from the central peak.

Finite-support optimum. Among all normalized rotor states supported on $\{-L,\dots,L\}$, the cosine-window probe is optimal. This is the standard finite-support sine-state optimizer of Refs. [29, 30], written in centered momentum coordinates:

$$|\eta^{(L)}_{\cos}\rangle_R = \frac{1}{\sqrt{L+1}} \sum_{\ell=-L}^{L} \cos\!\left(\frac{\pi\ell}{2(L+1)}\right) |\ell\rangle_R. \tag{6.23}$$

With $n = \ell+L$, the cosine coefficient becomes $\sin[\pi(n+1)/(2L+2)]$. Appendix E.2 recovers its finite-support optimality from the numerical radius of the compressed rotor shift.

In particular,

$$R_{\cos} = \cos\!\left(\frac{\pi}{2(L+1)}\right). \tag{6.24}$$

Its circular variance is therefore

$$V_{\cos} = 1 - \cos\left(\frac{\pi}{2(L+1)}\right) = \frac{\pi^2}{8(L+1)^2} + O(L^{-4}). \tag{6.25}$$

The corresponding error scale is

$$\Delta_{\cos} \sim \frac{\pi}{2(L+1)}. \tag{6.26}$$

The kinetic energy of this state is

$$E_{\cos} = \frac{2L^2+4L+3}{6} - \frac{1}{2}\csc^2\left(\frac{\pi}{2(L+1)}\right), \tag{6.27}$$

with the large-L behavior

$$E_{\cos} = \left(\frac{1}{3} - \frac{2}{\pi^2}\right)(L+1)^2 + O(L^{-2}). \tag{6.28}$$

Combining Eqs. (6.25) and (6.28) gives

$$V_{\cos} \sim \frac{\pi^2-6}{24E_{\cos}}, \qquad \Delta_{\cos} \sim \sqrt{\frac{\pi^2-6}{12E_{\cos}}}. \tag{6.29}$$

The cosine taper suppresses the angular tails responsible for the larger circular variance of the uniform probe. It achieves the $E_{\cos}^{-1/2}$ error scaling while retaining strictly finite momentum support.

Fixed-energy Mathieu optimum. The cosine-window probe is optimal when the momentum support is fixed. A second optimization removes the support restriction and fixes the mean rotor energy $E_R = \langle \hat{\ell}^2 \rangle$. Under this constraint, the minimum-circular-variance probe is a Mathieu state [31].

For a prescribed energy E_R, consider

$$V_\star(E_R) := \min_{\substack{\langle \eta|\eta\rangle=1 \\ \langle \eta|\hat{\ell}^2|\eta\rangle = E_R}} \left[1 - |\langle \eta|X_R(1)|\eta\rangle|\right]. \tag{6.30}$$

After centering the angular distribution at $\theta = 0$, the minimizing state can be chosen even, and minimizing V reduces to maximizing $\langle \cos\hat{\theta}\rangle$ at fixed $\langle \hat{\ell}^2\rangle$.

Introducing a Lagrange multiplier $\lambda > 0$ for the energy constraint leads to $H_\lambda := \hat{\ell}^2 - \lambda\cos\hat{\theta}$. Its ground state minimizes the corresponding variational functional and satisfies

$$\left(\hat{\ell}^2 - \lambda\cos\hat{\theta}\right)|\eta_\lambda\rangle = \varepsilon_\lambda|\eta_\lambda\rangle. \tag{6.31}$$

Choosing λ so that $\langle \eta_\lambda|\hat{\ell}^2|\eta_\lambda\rangle = E_R$ gives the constrained optimum in Eq. (6.30).

In the angle representation, $\hat{\ell} = -i\,d/d\theta$. With $z = \theta/2$, Eq. (6.31) takes the standard Mathieu form

$$\frac{d^2\eta_\lambda}{dz^2} + (a_\lambda - 2q_\lambda\cos 2z)\,\eta_\lambda = 0, \qquad a_\lambda = 4\varepsilon_\lambda, \qquad q_\lambda = -2\lambda.$$

The normalized even ground-state wavefunction is therefore

$$\eta_\lambda(\theta) = \langle \theta|\eta_\lambda\rangle = \mathcal{N}_\lambda\,\mathrm{ce}_0\left(\frac{\theta}{2}, -2\lambda\right). \tag{6.32}$$

For large E_R, the optimal circular variance satisfies

$$V_\star(E_R) \sim \frac{1}{8E_R}, \tag{6.33}$$

so the corresponding error scale obeys

$$\Delta_\star \sim \frac{1}{2\sqrt{E_R}}. \tag{6.34}$$

The Mathieu probe therefore achieves the same $E_R^{-1/2}$ error scaling as the cosine-window probe, with the optimal prefactor under the fixed-energy constraint. Appendix E.3 derives Eqs. (6.33) and (6.34) from the local quadratic approximation to the Mathieu ground state.

The Hamiltonian in Eq. (6.31) contains the same cosine potential used in the universal-control construction of Sec. 4.

Asymptotic comparison. Table 2 collects the three direct-angle probe families and their resource constraints.

Probe	Constraint	V	Error scale Δ_ϕ
Uniform momentum	$\lvert\ell\rvert \le L$	$\sim \dfrac{1}{\sqrt{12E_R}}$	$O(E_R^{-1/4})$
Cosine-window	$\lvert\ell\rvert \le L$	$\sim \dfrac{\pi^2-6}{24E_R}$	$\sim \sqrt{\dfrac{\pi^2-6}{12E_R}}$
Mathieu	E_R fixed	$\sim \dfrac{1}{8E_R}$	$\sim \dfrac{1}{2\sqrt{E_R}}$

Table 2: Asymptotic comparison of direct-angle rotor probes. The cosine-window probe minimizes V at fixed momentum support. The Mathieu probe minimizes V at fixed mean rotor energy.

Both optimized probes have $E_R^{-1/2}$ error scaling under the circular variance V, compared with $E_R^{-1/4}$ for the uniform momentum profile. The Mathieu probe has the smaller leading variance prefactor at fixed energy, $1/8 < (\pi^2-6)/24$, and the cosine-window probe has strictly finite momentum support.

7 Quantum Fourier transforms with rotor registers

A finite rotor code can itself serve as a computational register. A d-dimensional logical register can be represented either by states localized at d angles or by d classes of rotor momentum. We use these two encodings to construct the same d^r-point Fourier transform in two ways.

The first construction maps an angle-code input to a momentum-code output. It follows the standard base-d Fourier factorization [41, 53], with one local angle-to-momentum transform on each rotor and mixed angle–momentum phases between different registers. The second construction stays within a finite momentum code and compiles the same Fourier matrix using the gates introduced earlier. In this construction, each cross-register base-d phase is implemented by the quadratic rotor Clifford gate $\mathrm{CPHS}_{jk}(\alpha) = e^{i\alpha\hat{\ell}_j\hat{\ell}_k}$.

The two constructions therefore differ mainly in the local Fourier step: the first takes the angle-to-momentum code map as a logical operation, while the second resolves the Fourier transform into momentum-code gates.

When the input or output is stored in qubits, a qubit–rotor interface can be added before or after the Fourier circuit. The construction in Sec. 7.1 adapts the displacement-and-reset state-transfer method of Ref. [17], and related mixed analog–digital Fourier methods are developed in Ref. [32].

7.1 Rotor codes and qubit–rotor interfaces

The constructions use two complementary d-dimensional rotor codes. The angle code represents $x \in \{0, \dots, d-1\}$ by a localized wavepacket centered at an angular grid point, and the momentum code represents $p \in \{0, \dots, d-1\}$ by a superposition over one residue class of the integer rotor momentum. The generalized angle states introduced in Sec. 2.1 are not normalizable and therefore do not themselves define codewords.

For the angle code, set

$$\theta_x := \frac{2\pi x}{d}, \qquad x = 0, \dots, d-1. \tag{7.1}$$

We begin with the von Mises packets

$$|x;\kappa\rangle := \mathcal{N}_\kappa \int_0^{2\pi} e^{\kappa\cos(\theta-\theta_x)}|\theta\rangle_R \, d\theta, \qquad \mathcal{N}_\kappa := \frac{1}{\sqrt{2\pi I_0(2\kappa)}}, \tag{7.2}$$

where $\kappa > 0$ controls the angular localization and I_ℓ is the modified Bessel function of the first kind. These states are translations of a single packet,

$$|x;\kappa\rangle = Z_R(-\theta_x)|0;\kappa\rangle, \tag{7.3}$$

and have the momentum expansion

$$|x;\kappa\rangle = \sum_{\ell\in\mathbb{Z}} c_\ell^{(\kappa)} e^{-i\ell\theta_x}|\ell\rangle_R, \qquad c_\ell^{(\kappa)} := \frac{I_\ell(\kappa)}{\sqrt{I_0(2\kappa)}}. \tag{7.4}$$

The von Mises packets are normalized and nonorthogonal. Let

$$G_{xy}^{(\kappa)} := \langle x;\kappa|y;\kappa\rangle = \frac{I_0\Big(2\kappa\cos\frac{\theta_x-\theta_y}{2}\Big)}{I_0(2\kappa)}. \tag{7.5}$$

The Gram matrix $G^{(\kappa)}$ is circulant and positive definite. We define the orthonormal angle-code states by

$$|\overline{x}\rangle := \sum_{y=0}^{d-1} |y;\kappa\rangle \big(G^{(\kappa)}\big)^{-1/2}_{yx}, \qquad x = 0, \dots, d-1. \tag{7.6}$$

They satisfy

$$\langle\overline{x}|\overline{y}\rangle = \delta_{xy}, \qquad |\overline{x}\rangle = Z_R(-\theta_x)|\overline{0}\rangle. \tag{7.7}$$

We write

$$\mathcal{A}_d := \mathrm{span}\big\{|\overline{x}\rangle : 0 \le x < d\big\}. \tag{7.8}$$

The off-diagonal overlaps obey $\|G^{(\kappa)} - I\|_2 \le (d-1)\max_{x\neq y}|G^{(\kappa)}_{xy}|$.

For the momentum code, choose a normalized sequence $f = (f_n)_{n\in\mathbb{Z}} \in \ell^2(\mathbb{Z})$,

$$\sum_{n\in\mathbb{Z}} |f_n|^2 = 1, \tag{7.9}$$

and define

$$|\overline{p}\rangle := \sum_{n\in\mathbb{Z}} f_n\,|p+nd\rangle_R, \qquad p = 0,\dots,d-1. \tag{7.10}$$

Thus $|\overline{p}\rangle$ is supported on the momentum values satisfying

$$\ell \equiv p \pmod d. \tag{7.11}$$

Different values of p correspond to disjoint residue classes, and hence

$$\langle\overline{p}|\overline{q}\rangle = \delta_{pq}. \tag{7.12}$$

The momentum-code space is

$$\mathcal{M}_d(f) := \operatorname{span}\big\{|\overline{p}\rangle : 0 \le p < d\big\}. \tag{7.13}$$

The projector onto the momentum code is

$$\Pi_M := \sum_{p=0}^{d-1} |\overline{p}\rangle\langle\overline{p}|. \tag{7.14}$$

For the CPHS realization and gate-set compilation below, we choose

$$f_n = \delta_{n0}, \qquad |\overline{p}\rangle = |p\rangle_R, \qquad p = 0,\dots,d-1. \tag{7.15}$$

The corresponding code space is

$$\mathcal{M}_d^{(0)} := \mathcal{M}_d(\delta_0) = \operatorname{span}\{|0\rangle_R,\dots,|d-1\rangle_R\}. \tag{7.16}$$

Set

$$\omega_d := e^{2\pi i/d}. \tag{7.17}$$

The angle-to-momentum Fourier operation $F_d^{A\to M}$ is defined on the angle code by

$$F_d^{A\to M}|\overline{x}\rangle = \frac{1}{\sqrt{d}}\sum_{p=0}^{d-1}\omega_d^{px}|\overline{p}\rangle, \qquad x = 0,\dots,d-1. \tag{7.18}$$

The states on each side form orthonormal bases, so $F_d^{A\to M}$ is an active code-space unitary from $\mathcal{A}_d$ to $\mathcal{M}_d(f)$; the Fourier relation between the angle and momentum wavefunctions of a fixed rotor state is a change of representation. The code-space map extends to a unitary on $L^2(\mathbb{T})$.

The momentum-code Fourier transform is defined by

$$F_d^M|\overline{p}\rangle = \frac{1}{\sqrt{d}}\sum_{q=0}^{d-1}\omega_d^{qp}|\overline{q}\rangle, \qquad p = 0,\dots,d-1. \tag{7.19}$$

The two operations use the same $d\times d$ Fourier matrix. Their domains are

$$F_d^{A\to M} : \mathcal{A}_d \longrightarrow \mathcal{M}_d(f), \qquad F_d^M : \mathcal{M}_d(f) \longrightarrow \mathcal{M}_d(f). \tag{7.20}$$

The first operation is used in the angle–momentum construction. For the specialization $f = \delta_0$, the second operation is compiled from the hybrid gate set in Sec. 7.3.

For r rotors, the input and output code spaces are

$$\mathcal{A}_d^{\otimes r} \qquad \text{and} \qquad \mathcal{M}_d(f)^{\otimes r}. \tag{7.21}$$

If the input amplitudes are initially stored in qubits, they may be transferred coherently to the rotor codes before the Fourier operation. For the angle code, one may adapt the displacement-and-reset construction of Ref. [17]: qubit-controlled angular translations write the binary input label into the center of a localized rotor packet, and rotor-conditioned qubit operations return the source qubits to $|0\rangle$. The periodic rotor angle removes the padding and anti-padding steps needed to isolate a finite cyclic region of a noncompact oscillator.

The inverse sequence transfers the rotor-code amplitudes back to qubits when a qubit output is required.

7.2 Angle–momentum construction of the base-d QFT

The angle and momentum codes implement the base-d quantum Fourier transform across r rotor registers. The construction treats the active code-space unitary $F_d^{A\to M}$ and the mixed code-space phase as logical operations. The explicit gate-set construction in Sec. 7.3 resolves the momentum-code Fourier transform into the hybrid gates introduced earlier.

To define the mixed phase, introduce the finite-code digit operators

$$D_A := \sum_{x=0}^{d-1} x|\overline{x}\rangle\langle\overline{x}|, \qquad D_M := \sum_{p=0}^{d-1} p|\overline{p}\rangle\langle\overline{p}|. \tag{7.22}$$

The first operator is defined on the angle code $\mathcal{A}_d$, and the second is defined on the momentum code $\mathcal{M}_d(f)$. These are finite-rank spectral operators on their respective code spaces, extended by zero on the orthogonal complements.

For two distinct rotor registers R_j and R_k, define the mixed angle–momentum phase

$$\Lambda_{jk}(\beta) := \exp[i\beta\, D_{M,j} \otimes D_{A,k}]\,. \tag{7.23}$$

Its action on the relevant code spaces is

$$\Lambda_{jk}(\beta)|\overline{p}\rangle_{R_j}|\overline{x}\rangle_{R_k} = e^{i\beta px}|\overline{p}\rangle_{R_j}|\overline{x}\rangle_{R_k}, \qquad 0 \le p, x < d. \tag{7.24}$$

For a fixed j, the operations $\Lambda_{jk}(\beta)$ with $k > j$ commute.

Set $N = d^r$. Write an input integer in base d as

$$X(\mathbf{x}) := \sum_{k=1}^{r} x_k d^{r-k}, \qquad \mathbf{x} = \big(x_1, \ldots, x_r\big), \qquad 0 \le x_k < d, \tag{7.25}$$

with the most significant digit stored in R_1. The corresponding angle-code basis state is

$$|\overline{\mathbf{x}}\rangle := \bigotimes_{k=1}^{r} |\overline{x_k}\rangle_{R_k} \in \mathcal{A}_d^{\otimes r}. \tag{7.26}$$

For the momentum-code output, write

$$P(\mathbf{p}) := \sum_{j=1}^{r} p_j d^{r-j}, \qquad \mathbf{p} = \big(p_1, \ldots, p_r\big), \qquad 0 \le p_j < d, \tag{7.27}$$

and define

$$|\overline{\mathbf{p}}\rangle := \bigotimes_{j=1}^{r} |\overline{p_j}\rangle_{R_j} \in \mathcal{M}_d(f)^{\otimes r}. \tag{7.28}$$

The angle-to-momentum N-point Fourier transform is defined by

$$F_N^{A\to M}|\overline{\mathbf{x}}\rangle = \frac{1}{\sqrt{d^r}} \sum_{p_1,\ldots,p_r=0}^{d-1} \exp\Big[\frac{2\pi i}{d^r} X(\mathbf{x})P(\mathbf{p})\Big]\, |\overline{\mathbf{p}}\rangle. \tag{7.29}$$

Its matrix from $\mathcal{A}_d^{\otimes r}$ to $\mathcal{M}_d(f)^{\otimes r}$ is the standard positive-exponent d^r-point discrete Fourier matrix.

The circuit processes the rotor registers in the order

$$R_1, R_2, \ldots, R_r.$$

When register R_j is processed, it still contains the angle-code state $|\overline{x_j}\rangle$. We first apply the local transform $F_{d,j}^{A\to M}$, whose action is

$$F_{d,j}^{A\to M}|\overline{x_j}\rangle_{R_j} = \frac{1}{\sqrt{d}} \sum_{p_j=0}^{d-1} \exp\Big(\frac{2\pi i}{d} p_j x_j\Big)\, |\overline{p_j}\rangle_{R_j}. \tag{7.30}$$

The register R_j is now in the momentum code, and each register R_k with $k > j$ remains in the angle code. For every $k > j$, we then apply

$$\Lambda_{jk}\left(\frac{2\pi}{d^{k-j+1}}\right). \tag{7.31}$$

On the basis state $|\overline{p_j}\rangle_{R_j}|\overline{x_k}\rangle_{R_k}$, this operation contributes the phase

$$\exp\left(\frac{2\pi i}{d^{k-j+1}} p_j x_k\right). \tag{7.32}$$

The total phase associated with p_j after processing register R_j is therefore

$$\exp\left[2\pi i p_j \left(\frac{x_j}{d} + \frac{x_{j+1}}{d^2} + \cdots + \frac{x_r}{d^{r-j+1}}\right)\right]. \tag{7.33}$$

Define the jth register step by

$$V_j := \left[\prod_{k=j+1}^{r} \Lambda_{jk}\left(\frac{2\pi}{d^{k-j+1}}\right)\right] F_{d,j}^{A\to M}, \qquad 1 \le j \le r. \tag{7.34}$$

The product is the identity for $j = r$. For fixed j, all mixed angle–momentum phase operations in the product commute.

The complete circuit is

$$U_{\mathrm{AM}} := V_r V_{r-1} \cdots V_1, \tag{7.35}$$

with V_1 acting first.

The circuit produces the Fourier output digits in reverse register order. We therefore define the register-reversal unitary REV_r by

$$\mathrm{REV}_r\left(|\overline{p_1}\rangle_{R_1} \otimes \cdots \otimes |\overline{p_r}\rangle_{R_r}\right) := |\overline{p_r}\rangle_{R_1} \otimes \cdots \otimes |\overline{p_1}\rangle_{R_r}. \tag{7.36}$$

This operation only reverses the order of the rotor registers. It may be implemented physically by rotor SWAP gates or absorbed into the output register convention.

With this output convention, the complete circuit acts on $\mathcal{A}_d^{\otimes r}$ as

$$U_{\mathrm{AM}} = \mathrm{REV}_r F_N^{A\to M}. \tag{7.37}$$

Thus the circuit implements the standard positive-exponent d^r-point Fourier transform, with the output rotor registers appearing in reverse order. Appendix F.3 proves this factorization by matching the accumulated digit phase to the base-d Fourier kernel.

The factorization contains r local angle-to-momentum transforms and $\binom{r}{2}$ mixed code-space phases, up to output-register relabeling.

We next relate the two logical operations to rotor-space operations. The local transform $F_d^{A\to M}$ changes the momentum envelope and therefore requires controls that modify momentum-amplitude magnitudes.

For the mixed phase Λ_{jk}, a periodic multiplication operator provides an approximate realization on localized angle codes, with the code-space error and leakage bounds of Appendix F.1.

For the specialization $f_n = \delta_{n0}$, the mixed phase also admits a reduction to CPHS. Define the label-preserving code isometry $T_d : \mathcal{A}_d \to \mathcal{M}_d^{(0)}$ by

$$T_d|\overline{x}\rangle = |x\rangle_R, \qquad 0 \le x < d, \tag{7.38}$$

and choose a unitary extension to $L^2(\mathbb{T})$, also denoted by T_d. Let T_k act as T_d on register R_k and as the identity on the other registers. On the tensor product of $\mathcal{M}_d^{(0)}$ in register R_j and $\mathcal{A}_d$ in register R_k,

$$\Lambda_{jk}(\beta) = T_k^\dagger \,\mathrm{CPHS}_{jk}(\beta)\, T_k. \tag{7.39}$$

The map T_d preserves the logical digit and changes its encoding. The map $F_d^{A\to M}$ applies the finite Fourier matrix. For the momentum-code specialization in Eq. (7.15), Eq. (7.39) gives a CPHS realization of the mixed logical phase.

7.3 Gate-set compilation on rotor momentum codes

The angle–momentum construction treats the local angle-to-momentum Fourier operation and the mixed angle–momentum phase as logical operations. The momentum-code construction uses MQR, CShift, conditional-phase, CPHS, and Hadamard gates as logical instructions. We use the specialization $\mathcal{M}_d^{(0)}$ in Eq. (7.16), with $d = 2^s$. Throughout this subsection and Appendix G, the momentum code is $\mathcal{M}_d^{(0)}$. When a qubit–rotor interface is required, the binary label can be loaded by qubit-controlled shifts of distances $1, 2, \ldots, 2^{s-1}$, after which momentum-conditioned qubit rotations reset the source register. This gives the code-space action

$$\sum_{p=0}^{d-1} c_p |p\rangle_Q |0\rangle_R \longmapsto |0\rangle_Q^{\otimes s} \sum_{p=0}^{d-1} c_p |p\rangle_R.$$

For one s-qubit block, the transfer uses s CShift and s MQR instructions. The inverse transfer has the same count. For r registers, a one-way transfer therefore uses rs CShift and rs MQR instructions.

7.3.1 Compiled QFT on one rotor momentum code

The positive-exponent d-point Fourier transform is compiled on the momentum code $\mathcal{M}_d^{(0)}$. The qubit–rotor interface described above is used only when the input amplitudes are initially stored in qubits or a qubit output is required. The Fourier circuit acts entirely within $\mathcal{M}_d^{(0)}$.

Recall that

$$F_d^M |\overline{p}\rangle_R = \frac{1}{\sqrt{d}} \sum_{q=0}^{d-1} \omega_d^{qp} |\overline{q}\rangle_R, \qquad 0 \le p < d, \tag{7.40}$$

with $d = 2^s$ and $\omega_d = e^{2\pi i/d}$.

Let a be a reusable ancilla qubit initialized in $|0\rangle_a$. For $j = 0, \ldots, s-1$, define the momentum-conditioned ancilla rotation

$$B_j := \sum_{m=0}^{d-1} (iY_a)^{m_j} \otimes |\overline{m}\rangle\langle\overline{m}| + I_a \otimes \big(I_R - \Pi_M\big), \tag{7.41}$$

where

$$m_j := \left\lfloor \frac{m}{2^j} \right\rfloor \bmod 2 \tag{7.42}$$

is the jth binary digit of the current rotor momentum. The gate B_j is an MQR operation. In particular,

$$B_j^\dagger |0\rangle_a |\overline{m}\rangle_R = |m_j\rangle_a |\overline{m}\rangle_R. \tag{7.43}$$

Define

$$S_j := \mathrm{CShift}_{a\to R}(-2^j), \qquad \alpha_j := \frac{2\pi}{2^{j+1}}. \tag{7.44}$$

The conditional phase C_j is the gate introduced in Eq. (3.7), with the ancilla as the qubit register and $P_{c_a} = Z_a$. Its action is

$$C_j |c\rangle_a |\ell\rangle_R = e^{i\alpha_j c\ell} |c\rangle_a |\ell\rangle_R, \qquad c \in \{0, 1\}. \tag{7.45}$$

The jth Fourier stage is

$$F_j := B_j S_j^\dagger C_j (H_a \otimes I_R) S_j B_j^\dagger. \tag{7.46}$$

The factors act from right to left in the order

$$B_j^\dagger, \quad S_j, \quad H_a \otimes I_R, \quad C_j, \quad S_j^\dagger, \quad B_j.$$

The stages are applied in the order $j = s-1, s-2, \ldots, 0$, with the rightmost factor acting first. Fig. 7 summarizes their action: stage j replaces the input bit p_j by the Fourier-output bit c_j and returns the ancilla to $|0\rangle_a$. The stages produce the output bits in reversed binary order.

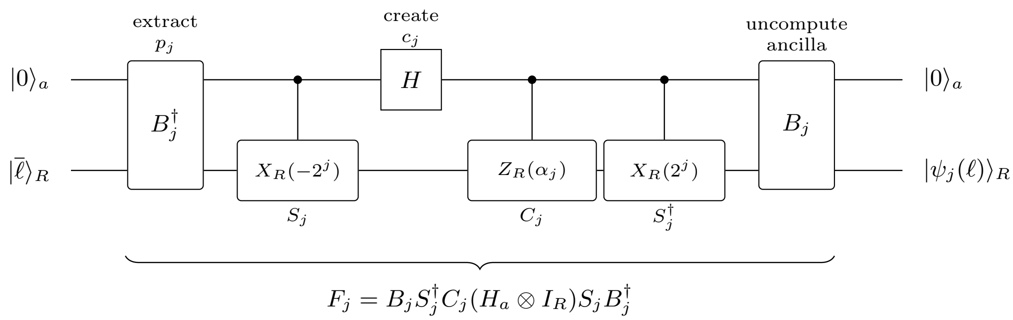

Figure 7: One stage of the gate-set compilation of the rotor momentum-code QFT. The momentum-dependent gate $B_j^\dagger$ extracts the jth input bit p_j into the ancilla. The controlled shift S_j removes this bit from the rotor momentum, the Hadamard introduces the output bit c_j, and C_j supplies the corresponding Fourier phase. The inverse shift writes c_j into the rotor momentum, and B_j returns the ancilla to $|0\rangle_a$.

Define the binary-reversal permutation on $\mathcal{M}_d^{(0)}$ by

$$\mathrm{BREV}_s \left| \overline{\sum_{j=0}^{s-1} 2^j c_j} \right\rangle_R := \left| \overline{\sum_{j=0}^{s-1} 2^{s-1-j} c_j} \right\rangle_R . \tag{7.47}$$

BREV_s reverses the s binary positions within one rotor code. The operation REV_r reverses the order of the r rotor registers.

Let $\widetilde{\mathrm{BREV}}_s$ denote the ancilla-assisted implementation satisfying

$$\widetilde{\mathrm{BREV}}_s |0\rangle_a |\overline{m}\rangle_R = |0\rangle_a \mathrm{BREV}_s |\overline{m}\rangle_R, \qquad 0 \le m < d. \tag{7.48}$$

Its construction from MQR and CShift operations is given in Appendix G.2.

Combining the s Fourier stages with the ancilla-assisted binary reversal, define

$$\widetilde{F}_d^M := \widetilde{\mathrm{BREV}}_s F_0 F_1 \cdots F_{s-1}. \tag{7.49}$$

Its action on the momentum code is

$$\widetilde{F}_d^M |0\rangle_a |\overline{p}\rangle_R = |0\rangle_a F_d^M |\overline{p}\rangle_R, \qquad 0 \le p < d. \tag{7.50}$$

The ancilla returns to $|0\rangle_a$ after every Fourier stage and after the binary-reversal circuit. Every rotor momentum visited by the compiled circuit lies in $\{0, \ldots, d-1\}$.

The Fourier-stage calculation and induction are given in Appendix G.1.

7.3.2 Base-d QFT compilation on rotor momentum codes

The one-rotor compilation extends to r rotor registers. This construction uses compiled one-rotor Fourier transforms and rotor–rotor CPHS gates on $(\mathcal{M}_d^{(0)})^{\otimes r}$, with both the input and the Fourier output encoded in this momentum code.

Let $N = d^r$, and write the input integer in base d as

$$X = \sum_{k=1}^{r} x_k d^{r-k}, \qquad x_k \in \{0, \ldots, d-1\}. \tag{7.51}$$

Here x_k denotes the input digit and p_j the Fourier-output digit; both are encoded in the momentum code $\mathcal{M}_d^{(0)}$. The digit x_k is encoded in register R_k as $|\overline{x_k}\rangle_{R_k}$.

The registers are processed sequentially in the order $R_1, R_2, \ldots, R_r$. On register R_j, first apply the compiled implementation of $F_{d,j}^M$. The resulting state is expanded in momentum-code output labels p_j, while every unprocessed register R_k, with $k > j$, still carries its input label x_k. Immediately after processing R_j, apply

$$\mathrm{CPHS}_{jk}\left(\frac{2\pi}{d^{k-j+1}}\right)|\ell_j, \ell_k\rangle = \exp\left(\frac{2\pi i \ell_j \ell_k}{d^{k-j+1}}\right)|\ell_j, \ell_k\rangle \tag{7.52}$$

for every $k > j$. For fixed j, these CPHS gates commute, so their order is immaterial. On a component labeled by p_j and x_k, the gate contributes

$$\exp\left(\frac{2\pi i p_j x_k}{d^{k-j+1}}\right), \tag{7.53}$$

which is the corresponding cross-digit factor in the base-d Fourier kernel. Because $\mathrm{CPHS}_{jk}(\alpha)$ is a pure-rotor quadratic Clifford gate, each cross-digit factor in Eq. (7.53) is realized by one rotor–rotor Clifford operation [26].

Let F_N^M denote the standard positive-exponent d^r-point Fourier transform in the standard base-d basis of $(\mathcal{M}_d^{(0)})^{\otimes r}$.

Let U_{QFT} denote the operation induced on the rotor registers by the circuit above, with the reusable ancilla initialized in $|0\rangle_a$ and returned to $|0\rangle_a$ after each local transform. Its action on $(\mathcal{M}_d^{(0)})^{\otimes r}$ is

$$U_{\mathrm{QFT}} = \mathrm{REV}_r F_N^M. \tag{7.54}$$

Here the register-order reversal is defined by

$$\mathrm{REV}_r \bigotimes_{j=1}^{r} |\overline{p_j}\rangle_{R_j} = \bigotimes_{j=1}^{r} |\overline{p_{r-j+1}}\rangle_{R_j}. \tag{7.55}$$

Appendix G.3 proves Eq. (7.54) from the base-d phase relation in Eq. (F.9).

Interpreting the output registers in reversed order requires no physical permutation. Restoring the original physical order requires $\lfloor r/2 \rfloor$ rotor SWAP gates.

The qubit–rotor interface described at the beginning of Sec. 7.3 may be applied separately to each rotor register when qubit input or output is required.

7.4 Logical resource comparison

To compare the two rotor constructions with the standard qubit circuit, we specialize to

$$N = d^r = 2^{rs}, \qquad d = 2^s. \tag{7.56}$$

All three constructions realize the same positive-exponent N-point Fourier matrix using different encodings and logical operations. The standard binary construction acts on rs qubits, the angle–momentum construction maps $\mathcal{A}_d^{\otimes r}$ to $\mathcal{M}_d(f)^{\otimes r}$, and the compiled momentum-code construction acts within $(\mathcal{M}_d^{(0)})^{\otimes r}$.

Table 3 compares the operations internal to the three encoded Fourier transforms; the qubit–rotor interface is counted separately in Table 7.

Table 3: Logical structure of three code-space constructions of the same $N = d^r = 2^{rs}$ Fourier matrix. The rows list the local and cross-block logical operations used by each construction.

Construction	Encoding map	Local transform on each block	Cross-block phase operations
Binary qubit construction	$\left(\mathbb{C}^2\right)^{\otimes rs} \longrightarrow \left(\mathbb{C}^2\right)^{\otimes rs}$	r s-qubit QFTs	$s^2\binom{r}{2}$ binary controlled-phase gates
Angle–momentum construction	$\mathcal{A}_d^{\otimes r} \longrightarrow \mathcal{M}_d(f)^{\otimes r}$	r angle-to-momentum Fourier operations	$\binom{r}{2}$ mixed angle–momentum phase operations
Compiled momentum-code construction	$(\mathcal{M}_d^{(0)})^{\otimes r} \longrightarrow (\mathcal{M}_d^{(0)})^{\otimes r}$	r compiled one-rotor d-point QFTs	$\binom{r}{2}$ CPHS gates

Each QFT on an s-qubit block contains s Hadamard gates and $\binom{s}{2}$ controlled-phase gates. The standard binary construction therefore uses rs Hadamard gates and

$$\binom{rs}{2} = r\binom{s}{2} + s^2\binom{r}{2} \tag{7.57}$$

controlled-phase gates. The first term counts phases internal to the r blocks, and the second counts phases coupling distinct blocks. Counting each Hadamard and controlled-phase gate once, the binary construction has total instruction count

$$N_{\mathrm{bin}} = rs + \binom{rs}{2} = \Theta((rs)^2). \tag{7.58}$$

The angle–momentum construction uses one local angle-to-momentum Fourier operation per rotor and one mixed angle–momentum phase per pair of rotors. In the compiled momentum-code construction, the cross-block Fourier factor that requires s^2 binary controlled-phase gates is implemented by one CPHS gate.

Each compiled one-rotor transform uses s sequential Fourier stages, the internal binary bit reversal constructed in Appendix G.2, and one reusable ancilla qubit. The same ancilla may be reused for all r local transforms. Detailed counts are collected in Table 7. Using the logical-instruction counting convention of Appendix G.4, these counts give

$$N_d = 6s + 5\left\lfloor \frac{s}{2} \right\rfloor - 1, \qquad N_{\mathrm{rot}} = rN_d + \binom{r}{2} = O(rs + r^2). \tag{7.59}$$

For $r \geq 2$, the smallest cross-register phase angle in both rotor constructions is

$$\frac{2\pi}{d^r} = \frac{2\pi}{N}. \tag{7.60}$$

The binary QFT contains controlled-phase rotations at the same scale. Approximate QFT circuits can reduce the binary count by truncating small-angle rotations [54]; the same truncation principle applies to the small conditional-phase and CPHS angles in the rotor decomposition. Table 3 compares the transforms.

8 Physical implementation considerations

The logical operations used above require different physical controls in native rotors and finite-code implementations. A native rotor supplies the periodic angle and integer momentum directly. A finite-code implementation reproduces selected rotor operations on a spectral subspace of another system.

8.1 Native-rotor and finite-code routes

Native-rotor route. Superconducting phase–charge degrees of freedom directly realize a periodic phase and integer-valued conjugate charge. A flux-tunable Cooper-pair-box Hamiltonian $H_{\mathrm{CPB}} = 4E_C(\hat{n}-n_g)^2 - E_J \cos\hat{\phi}$ contains the drift and cosine terms used in the universal-control construction [33]. After division by $4E_C$ and removal of an additive constant, its charging term has the form of Eq. (4.6), with $\hat{\ell} = \hat{n}$ and $\xi = -2n_g$, while tuning E_J supplies the cosine control. A stable offset bias $n_g \notin \frac{1}{2}\mathbb{Z}$ realizes the nonresonance condition $\xi \notin \mathbb{Z}$ used in Sec. 4. At a different operating point, $n_g = 0$, the rescaled Hamiltonian is the Mathieu operator in Eq. (6.31), with $\lambda = E_J/(4E_C)$. The same phase–charge variables also appear in proposals for rotor codes [9], and in recent superconducting implementations of compact $U(1)$ gauge fields coupled to matter [7].

Trapped planar rotors provide a direct realization of the U(1) degree of freedom, with a periodic angle and integer-valued angular momentum [3–5]. Molecular ions and ultracold molecules have larger rotational state spaces, but resolved angular-momentum manifolds and coherent internal-state control allow selected levels to be used as finite rotor codes [1, 55, 56]. Coherent translation on a momentum lattice, another operation used in the constructions above, has also been demonstrated in atom-optics kicked rotors and momentum-space quantum walks [57, 58].

Finite-code route. Oscillator platforms can reproduce selected rotor operations on finite codes. Dispersive cavity and trapped-ion controls provide number-selective qubit operations, conditional displacements, and nonlinear bosonic interactions [21, 34, 35]. Trapped-ion implementations of trigonometric continuous-variable gates also include the periodic cosine control used in Sec. 4 [36]. In this setting, the rotor is represented only on a chosen finite spectral subspace; the full oscillator need not reproduce the rotor algebra outside that code. The additional requirements are preparation of the encoded states, spectrally selective control within the code, and suppression of leakage outside it.

8.2 Physical requirements for the gate set

Table 4 summarizes the physical capabilities associated with the logical operations used throughout the paper.

Table 4: Physical requirements and main uses of the logical operations in the paper.

Logical operation	Required physical capability	Main use
Momentum shifts and momentum-diagonal phase gates	Integer translations of rotor momentum and evolution generated by $\hat{\ell}$ or $\hat{\ell}^2$	Rotor Clifford circuits; gauge dynamics
Periodic angle potentials	Evolution generated by $V(\hat{\theta})$, including the cosine gate used in the universal-control construction	Universal control; gauge dynamics
Momentum-lattice automorphisms U_A	Integer linear transformations of the rotor momentum coordinates	Multirotor Clifford synthesis
$\Gamma_{c,j}$ and MQR	Qubit operations conditioned on rotor parity or on selected momentum values or residue classes	Mixed Clifford gates; coherent transfer; QFT compilation
CShift and $\mathcal{O}_U$	Qubit-conditioned momentum shift or target operations conditioned on rotor momentum	Gauge hopping; phase estimation; coherent transfer
$\mathrm{CPHS}_{ij}(\alpha)$	Evolution generated by an interaction proportional to $\hat{\ell}_i\hat{\ell}_j$	Cross-register Fourier phases
Code preparation and readout	Preparation of finite momentum superpositions and measurement of rotor momentum or angle	Phase estimation; encoded Fourier processing

Momentum-resolved qubit control gives an oscillator analogue of MQR [20, 21, 34], and conditional displacements implement the qubit-to-mode control used by CShift [35]. The two-rotor interaction required by CPHS is proportional to $\hat{\ell}_i \hat{\ell}_j$; its oscillator analogue is a number–number or cross-Kerr interaction [59, 60].

8.3 Control scales and finite-window diagnostics

For the compiled QFT, the code size $d = 2^s$ fixes both the momentum range and the phase resolution. We use the momentum code

$$\mathcal{M}_d^{(0)} = \operatorname{span}\{|0\rangle_R, \ldots, |d-1\rangle_R\}, \qquad d = 2^s.$$

Every intermediate momentum reached by the circuit remains in $\{0, \ldots, d-1\}$. The Fourier stages use qubit-controlled shifts with distances at most 2^{s-1} and MQR operations that resolve individual binary digits of the momentum label. The binary-reversal circuit also uses MQR operations conditioned on selected two-bit patterns. The smallest local conditional phase used in the compilation is $2\pi/d$. For r rotor registers, with $N = d^r$, the smallest cross-register CPHS angle is

$$\frac{2\pi}{N} = \frac{2\pi}{d^r}.$$

Table 5 gives an illustrative example with $r = 2$, $s = 3$, $d = 8$, and $N = 64$. The instruction counts follow Eq. (7.59) and the convention of Appendix G.4.

Table 5: Illustrative control requirements and instruction counts for the compiled two-rotor $N = 64$ QFT with $r = 2$, $s = 3$, and $d = 8$. Counts follow the logical-instruction convention of Appendix G.4.

Requirement	Target
Momentum range per rotor	$\ell = 0, \ldots, 7$
Maximum CShift distance	4
Momentum selectivity (MQR)	Individual bits and selected two-bit patterns of $\ell \in \{0, \ldots, 7\}$
Smallest local conditional phase used	$\pi/4$
Cross-register CPHS phase	$\pi/32$
Compiled-QFT instruction count	$N_d = 22$ per rotor; $N_{\text{rot}} = 45$ total

The phase-estimation protocol imposes a different finite-range requirement. For a probe with finite momentum support, the largest occupied $|\ell|$ fixes the largest controlled power $U^{-\ell}$ that must be implemented. Increasing the support therefore increases the range of controlled powers required by the protocol.

For the angle-code QFT construction, the relevant finite-code errors are those associated with the realization of the mixed angle–momentum phase. The code-space error and leakage are bounded by Eqs. (F.3) and (F.4), respectively. Both bounds are controlled by the weight of the angle-code wavefunctions outside their assigned angular cores.

The gauge calculation uses the hard-wall electric-flux cutoff $|E_e| \le L$. The link-averaged boundary occupation $\overline{p}_{\partial L}$ in Eq. (D.24) measures the weight on the flux states where the projected shift differs from the full rotor shift. Its decrease with L therefore provides a direct diagnostic of the finite-flux truncation.

9 Conclusion and outlook

This paper has treated the $U(1)$ rotor as a computational register in its own right, coupled directly to qubits. The Clifford theory that results is directional but constructive: rotor momentum parity may control qubit Pauli operations while the reverse is forbidden, every commutation-preserving phase-space action has an explicit finite circuit realization, and the mixed part of that circuit has an exact minimal gate count. The same analysis gives complete Clifford criteria for the momentum- and angle-dependent gate families used throughout the paper. Adding two non-Clifford controls promotes the local Clifford operations to universal control on the full Hilbert space in the strong operator topology.

The applications use this structure in different ways. For compact $U(1)$ gauge–matter dynamics, we constructed an exact full-space realization of gauge-covariant hopping and studied the effect of a hard-wall electric-flux cutoff on ground-state and real-time observables. For rotor phase estimation, we used the duality $\mathbb{Z} \longleftrightarrow \mathbb{T}$ to convert phase kickback into a translation of the measured angle distribution; this removes the need for a coherent inverse QFT on the phase register and turns probe preparation into an optimization problem under momentum-support or mean-energy constraints. For Fourier processing, we gave both an angle-to-momentum code construction and an explicit gate-set compilation within a finite momentum code, in which quadratic rotor interactions implement the cross-register Fourier phases.

We also identified the physical capabilities these logical constructions require. A native phase–charge rotor supplies the integer momentum, periodic angle, quadratic drift, and cosine potential directly. A finite-code implementation can reproduce the same logical operations through momentum-selective qubit control, conditional displacements, and nonlinear interactions on a chosen spectral subspace. In both routes the rotor enters through its full phase-space structure, not only as a large code space.

Two limitations remain. Strong-operator density is an existence statement and yields no bound on circuit length or control time. The Fourier resource counts are logical instruction counts, not physical gate counts; they assign unit cost to MQR, CShift, conditional-phase, CPHS, and Hadamard operations, and they exclude state preparation, spectral selectivity, interaction time, phase resolution, readout, and leakage. Sec. 8 identifies where these requirements enter the two implementation routes, but does not fix their quantitative cost.

The main remaining problem is therefore quantitative compilation. Finite-window synthesis bounds for CShift, MQR, and $\mathcal{O}_U$ would connect the strong-density result to circuit length and control time, and would determine whether the logical compression of the cross-register Fourier phases survives once spectral selectivity and small interaction angles are assigned physical costs. A second problem is algebraic: hard-wall projection makes the rotor shift nonunitary while preserving the finite Gauss-law basis, while cyclic completion restores unitarity at the price of changing the shift relation at the boundary, so the Clifford and normalizer structures of these finite models need not coincide with those of the full rotor. Understanding that change bears directly on gate synthesis and on the boundary between classically simulable hybrid normalizer circuits and circuits containing additional non-Clifford operations. Beyond $U(1)$, compact Abelian groups are the next setting for the structural theory, followed by non-Abelian compact groups, where continuous group variables are accompanied by discrete representation data.

Acknowledgments

We thank Joel Bierman, Weijian Chen, Raghav Jha, Yuan Liu, and Grant Scotto for fruitful discussions. This work was supported by the U.S. Department of Energy, Advanced Scientific Computing Research, under contract number DE-SC0025384.

A Proofs for the hybrid Clifford classification

This appendix gives the block calculation underlying the hybrid phase-space classification in Theorem 2.3 and computes the one-qubit–one-rotor symplectic group and Clifford quotient. The explicit unitary realization, the kernel of the induced Clifford action, and the classification of mixed blocks under separate qubit and rotor Clifford operations are proved in the main text.

A.1 Block classification of hybrid phase-space transformations

Set $V = \mathbb{F}_2^{2n}$, and let $\rho_2 : \mathbb{Z}^r \to \mathbb{F}_2^r$ denote reduction modulo two. Let $S : K_{n,r} \to K_{n,r}$ be a group automorphism preserving ω. With respect to the decomposition $K_{n,r} = V \oplus \mathbb{Z}^r \oplus \mathbb{T}^r$, write S in block form as

$$\begin{pmatrix} q' \\ m' \\ \phi' \end{pmatrix} = \begin{pmatrix} S_{VV} & S_{V\mathbb{Z}} & S_{V\mathbb{T}} \\ S_{\mathbb{Z}V} & S_{\mathbb{Z}\mathbb{Z}} & S_{\mathbb{Z}\mathbb{T}} \\ S_{\mathbb{T}V} & S_{\mathbb{T}\mathbb{Z}} & S_{\mathbb{T}\mathbb{T}} \end{pmatrix} \begin{pmatrix} q \\ m \\ \phi \end{pmatrix}. \tag{A.1}$$

Each row specifies a target component, and each column specifies a source component. We first use the group structures of V, $\mathbb{Z}^r$, and $\mathbb{T}^r$ to determine the possible nonzero blocks, and then impose preservation of ω.

The group $\mathbb{T}^r$ is divisible. The groups V and $\mathbb{Z}^r$ contain no nonzero divisible subgroups. In addition, V is torsion and $\mathbb{Z}^r$ is torsion-free. Hence

$$\mathrm{Hom}(\mathbb{T}^r, V) = 0, \qquad \mathrm{Hom}(\mathbb{T}^r, \mathbb{Z}^r) = 0, \qquad \mathrm{Hom}(V, \mathbb{Z}^r) = 0. \tag{A.2}$$

Every homomorphism $\mathbb{Z}^r \to V$ factors through ρ_2; every homomorphism $V \to \mathbb{T}^r$ has image in $\{0, \pi\}^r$. The remaining blocks therefore have the form

$$\begin{pmatrix} q' \\ m' \\ \phi' \end{pmatrix} = \begin{pmatrix} M & C\rho_2 & 0 \\ 0 & A & 0 \\ \pi G & B & \alpha \end{pmatrix} \begin{pmatrix} q \\ m \\ \phi \end{pmatrix}, \tag{A.3}$$

or, in component form,

$$\begin{aligned} q' &= Mq + C\bar{m}, \\ m' &= Am, \\ \phi' &= \alpha(\phi) + Bm + \pi G q. \end{aligned} \tag{A.4}$$

Here M, C, and G are matrices over $\mathbb{F}_2$, A is an integer matrix, and B has entries in $\mathbb{T}$.

The subgroup $\mathbb{T}^r$ is the unique maximal divisible subgroup of $K_{n,r}$ and is therefore preserved by S. In the quotient $K_{n,r}/\mathbb{T}^r$, the subgroup V is precisely the torsion subgroup and is also preserved. It follows that S induces automorphisms on the three diagonal components, so

$$M \in \mathrm{GL}(2n, \mathbb{F}_2), \qquad A \in \mathrm{GL}(r, \mathbb{Z}), \qquad \alpha \in \mathrm{Aut}(\mathbb{T}^r). \tag{A.5}$$

We now impose preservation of ω on four types of inputs.

Qubit–qubit inputs. For $q, p \in V$, preservation of ω on $(q, 0, 0)$ and $(p, 0, 0)$ gives

$$M^{\mathsf{T}} J_n M = J_n. \tag{A.6}$$

Thus $M \in \mathrm{Sp}(2n, \mathbb{F}_2)$.

Torus–integer inputs. For $\phi \in \mathbb{T}^r$ and $k \in \mathbb{Z}^r$, preservation of ω on $(0, 0, \phi)$ and $(0, k, 0)$ gives $\exp\bigl(i\alpha(\phi)^{\mathsf{T}} Ak\bigr) = \exp\bigl(i\phi^{\mathsf{T}} k\bigr)$ for all $k \in \mathbb{Z}^r$. Taking k to be the standard basis vectors of $\mathbb{Z}^r$ gives $A^{\mathsf{T}}\alpha(\phi) = \phi$ in $\mathbb{T}^r$. Therefore

$$\alpha(\phi) = A^{-\mathsf{T}}\phi. \tag{A.7}$$

Qubit–integer inputs. For $q \in V$ and $k \in \mathbb{Z}^r$, $\omega\big((q,0,0),(0,k,0)\big) = 1$. Preservation of ω therefore requires $M^\mathsf{T} J_n C + G^\mathsf{T} \bar{A} = 0$. Since $\bar{A}$ is invertible over $\mathbb{F}_2$, this gives

$$G = \bar{A}^{-\mathsf{T}} C^\mathsf{T} J_n M. \tag{A.8}$$

Integer–integer inputs. For $m, k \in \mathbb{Z}^r$, preservation of ω on $(0,m,0)$ and $(0,k,0)$ gives

$$A^\mathsf{T} B - B^\mathsf{T} A = \pi C^\mathsf{T} J_n C. \tag{A.9}$$

Define $\Theta = A^\mathsf{T} B$. Then $B = A^{-\mathsf{T}}\Theta$ and Eq. (A.9) becomes Eq. (2.23).

For every $v \in \mathbb{F}_2^r$, $A^{-\mathsf{T}}(\pi v) = \pi \bar{A}^{-\mathsf{T}} v$ in $\mathbb{T}^r$. Substitution of Eqs. (A.7), (A.8), and (A.9) into Eq. (A.4) gives Eq. (2.22).

The pairing is already trivial on $V \times \mathbb{T}^r$ and $\mathbb{T}^r \times \mathbb{T}^r$, both before and after applying S. Reversing the order of the two inputs only inverts the resulting phase. The four cases above therefore cover all pairs of components. Conversely, direct substitution shows that M preserves the qubit–qubit term, $\alpha = A^{-T}$ preserves the torus–integer term, the block G cancels the qubit–integer terms, and Eq. (2.23) cancels the extra integer–integer term. Hence every map in Eq. (2.22) satisfying Eq. (2.23) preserves ω.

Such a map is invertible. From (q', m', ϕ'), the input is recovered successively as

$$m = A^{-1} m', \qquad q = M^{-1}(q' - C\bar{m}), \qquad \phi = A^\mathsf{T}\phi' - \Theta m - \pi C^\mathsf{T} J_n M q. \tag{A.10}$$

All maps whose domains are V or $\mathbb{Z}^r$ are continuous because these groups are discrete. The formula $\alpha = A^{-\mathsf{T}}$ and the inverse above show that S and S^{-1} are continuous.

Finally, the action of S on inputs supported in each of the three components determines M, C, A, B, G, and α uniquely, and $\Theta = A^\mathsf{T} B$. This proves Theorem 2.3.

Composition and inverse. With the convention $S_1 S_2 = S_1 \circ S_2$, direct substitution gives, for $S_i = S_{M_i, A_i, C_i, \Theta_i}$,

$$\begin{aligned} M_{12} &= M_1 M_2, & A_{12} &= A_1 A_2, \\ C_{12} &= M_1 C_2 + C_1 \bar{A}_2, & \Theta_{12} &= \Theta_2 + A_2^\mathsf{T} \Theta_1 A_2 + \pi \bar{A}_2^\mathsf{T} C_1^\mathsf{T} J_n M_1 C_2. \end{aligned} \tag{A.11}$$

The inverse has parameters

$$\begin{aligned} \widetilde{M} &= M^{-1}, & \widetilde{A} &= A^{-1}, \\ \widetilde{C} &= M^{-1} C \bar{A}^{-1}, & \widetilde{\Theta} &= -A^{-\mathsf{T}} \Theta A^{-1} + \pi \widetilde{C}^\mathsf{T} J_n \widetilde{C}. \end{aligned} \tag{A.12}$$

A.2 The one-qubit–one-rotor quotient

Proposition A.1 (One-qubit–one-rotor symplectic group)**.** *For one qubit and one rotor,*

$$\mathrm{Sp}(K_{1,1}, \omega) \cong \mathbb{T} \times S_4 \times \mathbb{Z}_2. \tag{A.13}$$

Consequently, $\mathrm{Cl}_{1,1} / \mathcal{P}_{1,1} \cong \mathbb{T} \times S_4 \times \mathbb{Z}_2$.

Proof. For $n = r = 1$, the parameters in Theorem 2.3 reduce to $M \in \mathrm{Sp}(2, \mathbb{F}_2) = \mathrm{GL}(2, \mathbb{F}_2), c \in \mathbb{F}_2^2, \epsilon \in \{\pm 1\}, \theta \in \mathbb{T}$. Since the form defined by J_1 is alternating, $c^\mathsf{T} J_1 c = 0$. The constraint on θ is therefore automatically satisfied for every $\theta \in \mathbb{T}$. Using the convention $S_1 S_2 = S_1 \circ S_2$, the composition law is

$$(M, c, \epsilon, \theta)(N, d, \delta, \eta) = \big(MN, c + Md, \epsilon\delta, \theta + \eta + \pi c^\mathsf{T} J_1 M d\big). \tag{A.14}$$

Define $\nu : \mathbb{F}_2^2 \to \mathbb{F}_2$ by $\nu(0) = 0, \nu(c) = 1 (c \neq 0)$. Every $M \in \mathrm{GL}(2, \mathbb{F}_2)$ permutes the three nonzero vectors, and direct calculation gives

$$\nu(Mc) = \nu(c), \qquad \nu(c) + \nu(d) + \nu(c + d) = c^\mathsf{T} J_1 d \quad \text{in } \mathbb{F}_2. \tag{A.15}$$

Define the shifted torus coordinate $\widetilde{\theta} = \theta + \pi\nu(c)$. With this redefined parameter, the final phase term in Eq. (A.14) is absorbed, and the product becomes

$$(M, c, \epsilon, \widetilde{\theta})(N, d, \delta, \widetilde{\eta}) = \Big(MN, c + Md, \epsilon\delta, \widetilde{\theta} + \widetilde{\eta}\Big). \tag{A.16}$$

The pair (M, c) has the product law of $\mathrm{AGL}(2, \mathbb{F}_2)$. Its action on the four points of $\mathbb{F}_2^2$ is faithful, and $|\mathrm{AGL}(2, \mathbb{F}_2)| = 4|\mathrm{GL}(2, \mathbb{F}_2)| = 24$. Hence $\mathrm{AGL}(2, \mathbb{F}_2) \cong S_4$. Equation (A.16) proves Eq. (A.13), and Corollary 2.5 gives the Clifford quotient. □

B Proofs of the gate-family criteria

This appendix proves the classification results for momentum-diagonal phase gates and momentum-dependent qubit gates. Both proofs use conjugation of the elementary momentum shift. In the first case, this gives a scalar finite-difference equation; in the second, it gives an operator-valued finite-difference equation. The remaining Clifford criteria in Sec. 3 are proved directly in the main text.

B.1 Momentum-diagonal phase gates

Proof of Proposition 3.1. Let e_j be the jth standard basis vector of $\mathbb{Z}^r$. Conjugating the corresponding momentum shift gives

$$G_u X_R(e_j) G_u^\dagger |\ell\rangle = \frac{u(\ell + e_j)}{u(\ell)} |\ell + e_j\rangle. \tag{B.1}$$

If G_u is Clifford, the coefficient multiplying the shift must, up to a constant phase, be a character of $\mathbb{Z}^r$. Hence there exist $\rho_j \in \mathbb{T}$ and $r_j \in \mathbb{T}^r$ such that

$$\frac{u(\ell + e_j)}{u(\ell)} = e^{i\rho_j + i r_j^\mathsf{T} \ell}. \tag{B.2}$$

We now compare the value of $u(\ell + e_i + e_j)$ obtained by applying Eq. (B.2) first in the e_i-direction and then in the e_j-direction with the value obtained in the reverse order. This gives $(r_j)_i = (r_i)_j$ in $\mathbb{T}$. Thus the matrix $R = (r_1, \ldots, r_r)$ is symmetric.

From the definition of f_R in Eq. (2.30),

$$f_R(\ell + e_j) - f_R(\ell) = r_j^\mathsf{T} \ell + R_{jj}. \tag{B.3}$$

Set $\lambda_j = \rho_j - R_{jj}$ and define

$$h(\ell) = u(\ell) e^{-i\lambda^\mathsf{T} \ell - i f_R(\ell)}. \tag{B.4}$$

Eqs. (B.2) and (B.3) imply $h(\ell + e_j) = h(\ell)$ for every $\ell \in \mathbb{Z}^r$ and every j. Replacing ℓ by $\ell - e_j$ gives the same equality for a shift by $-e_j$. Since any two points of $\mathbb{Z}^r$ are connected by such unit shifts, h is constant on $\mathbb{Z}^r$. Writing $h(0) = e^{i\gamma}$ gives

$$u(\ell) = e^{i\gamma + i\lambda^\mathsf{T} \ell + i f_R(\ell)}. \tag{B.5}$$

Conversely, if u has the form in Eq. (B.5), then $G_u = e^{i\gamma} Z_R(\lambda) Q_R$. The gates $Z_R(\lambda)$ and Q_R are pure-rotor Clifford gates by Sec. 3.1. Therefore $G_u \in \mathrm{Cl}_{0,r}$. □

B.2 Momentum-dependent qubit gates

Proof of Proposition 3.2. For brevity, write $U = \mathcal{V}$. Conjugating the elementary rotor shift gives

$$U(I \otimes X_R(1)) U^\dagger = \sum_{\ell \in \mathbb{Z}} V_{\ell+1} V_\ell^\dagger \otimes |\ell + 1\rangle\langle \ell|. \tag{B.6}$$

If U is Clifford, the right-hand side must be proportional to a hybrid Weyl operator with momentum shift 1. Its qubit part must therefore be a fixed Pauli operator. Its scalar dependence on ℓ must be a character of $\mathbb{Z}$. Hence there exist $c \in \mathbb{F}_2^{2n}$ and $\mu, \alpha \in \mathbb{T}$ such that

$$V_{\ell+1} V_\ell^\dagger = e^{i\mu + i\alpha\ell} P_c. \tag{B.7}$$

Applying Eq. (B.7) successively gives

$$V_\ell = e^{i\mu\ell + i\alpha\ell(\ell-1)/2} P_c^\ell V_0. \tag{B.8}$$

For negative ℓ, the same formula follows by solving Eq. (B.7) for V_ℓ in terms of $V_{\ell+1}$.

Set $\lambda = \mu - \alpha$. Then

$$V_\ell = e^{i[\lambda\ell + \alpha\ell(\ell+1)/2]} P_c^\ell V_0. \tag{B.9}$$

It remains to show that V_0 is a qubit Clifford operator.

For every qubit Pauli operator P_b,

$$U(P_b \otimes I_R)U^\dagger = \sum_{\ell\in\mathbb{Z}} V_\ell P_b V_\ell^\dagger \otimes |\ell\rangle\langle\ell|. \tag{B.10}$$

Since U is Clifford, this operator must be proportional to a hybrid Weyl operator. It preserves each momentum subspace, so its rotor-shift component must be zero. Evaluating the qubit block at $\ell = 0$ shows that $V_0 P_b V_0^\dagger$ is proportional to a Pauli operator. This holds for every P_b, and hence V_0 normalizes the qubit Pauli group. Therefore $V_0 \in \mathrm{Cl}_{n,0}$.

Conversely, suppose that Eq. (B.9) holds with $V_0 \in \mathrm{Cl}_{n,0}$. Let $Q_{(\alpha)}$ be the one-rotor quadratic gate corresponding to the 1×1 matrix $R = (\alpha)$. Acting on each momentum subspace gives

$$\mathcal{V} = \big[I_Q \otimes Z_R(\lambda)Q_{(\alpha)}\big]\Gamma_{c,1}(V_0 \otimes I_R). \tag{B.11}$$

Here $Z_R(\lambda)Q_{(\alpha)}$ is a pure-rotor Clifford gate, $\Gamma_{c,1}$ is a mixed Clifford gate, and V_0 is a qubit Clifford gate. Therefore $\mathcal{V} \in \mathrm{Cl}_{n,1}$. $\square$

C Proofs for universal control

As in Sec. 4.1, all strong closures below are taken in $\mathrm{U}(\mathcal{H})$. Multiplication and inversion are continuous in the strong operator topology on $\mathrm{U}(\mathcal{H})$, so the strong closure of a unitary subgroup is again a subgroup.

C.1 Finite-window approximation and strong density

Let P_L and $\mathcal{H}_L$ be as in Lemma 4.2.

Lemma C.1 (Finite-window unitary approximation)**.** *For every $V \in \mathrm{U}(\mathcal{H})$, every finite set of vectors $\psi_1, \ldots, \psi_s \in \mathcal{H}$, and every $\delta > 0$, there exist L and $V_L \in \mathrm{U}(\mathcal{H}_L)$ such that*

$$\|V_L P_L \psi_j - P_L V \psi_j\| < \delta, \qquad j = 1, \ldots, s, \tag{C.1}$$

and

$$\|(I - P_L)\psi_j\| < \delta, \qquad \|(I - P_L)V\psi_j\| < \delta. \tag{C.2}$$

Proof. Let $\mathcal{S} = \mathrm{span}\{\psi_1, \ldots, \psi_s\}$. Since $\mathcal{S}$ and $V\mathcal{S}$ are finite-dimensional and $P_L \to I$ strongly, the convergence is uniform on the unit spheres of both subspaces. Hence, for sufficiently large L, the restrictions of P_L to $\mathcal{S}$ and $V\mathcal{S}$ are injective.

Define

$$T_L : P_L\mathcal{S} \longrightarrow P_L V\mathcal{S}, \qquad T_L(P_L x) = P_L V x. \tag{C.3}$$

This map is well defined because the restriction of P_L to $\mathcal{S}$ is injective. The uniform convergence on $\mathcal{S}$ and $V\mathcal{S}$ implies

$$\left\|T_L^\dagger T_L - I_{P_L\mathcal{S}}\right\| \longrightarrow 0. \tag{C.4}$$

Let $T_L = Q_L|T_L|$ be the polar decomposition of T_L. Since T_L is an invertible map from $P_L\mathcal{S}$ onto $P_L V\mathcal{S}$, the operator Q_L is unitary between these two subspaces. Moreover,

$$\|Q_L - T_L\| = \big\||T_L| - I_{P_L\mathcal{S}}\big\| \longrightarrow 0. \tag{C.5}$$

The subspaces $P_L\mathcal{S}$ and $P_L V\mathcal{S}$ have the same dimension. Their orthogonal complements in $\mathcal{H}_L$ therefore also have the same dimension, so Q_L extends to a unitary $V_L \in \mathrm{U}(\mathcal{H}_L)$. For each j, $\|V_L P_L \psi_j - P_L V \psi_j\| = \|(Q_L - T_L)P_L\psi_j\|$, which is smaller than δ for sufficiently large L. Increasing L further if necessary also gives Eq. (C.2). $\square$

Proof of Lemma 4.2. Fix $V \in \mathrm{U}(\mathcal{H})$, vectors $\psi_1, \ldots, \psi_s \in \mathcal{H}$, and $\epsilon > 0$. Set

$$M = \max\{1, \|\psi_1\|, \ldots, \|\psi_s\|\}, \qquad \delta = \frac{\epsilon}{8M}. \tag{C.6}$$

Choose L and $V_L \in \mathrm{U}(\mathcal{H}_L)$ from Lemma C.1. By the hypothesis of Lemma 4.2, there exists $W \in \overline{G}^{\mathrm{s}}$ preserving $\mathcal{H}_L$ and satisfying $\|W|_{\mathcal{H}_L} - V_L\| < \delta$. Since W and V are unitary,

$$\begin{aligned}\|(W - V)\psi_j\| &\le \|(I - P_L)\psi_j\| + \|WP_L\psi_j - V_LP_L\psi_j\| + \|V_LP_L\psi_j - P_LV\psi_j\| + \|(I - P_L)V\psi_j\| \\ &< 3\delta + \delta\|\psi_j\| \le 4\delta M = \frac{\epsilon}{2}.\end{aligned} \tag{C.7}$$

Because $W \in \overline{G}^{\mathrm{s}}$, there exists $g \in G$ such that $\|(g - W)\psi_j\| < \epsilon/2$ for every j. Therefore $\|(g - V)\psi_j\| < \epsilon$ for every j, proving that G is strongly dense in $\mathrm{U}(\mathcal{H})$. $\square$

C.2 Spectral conditions for single-rotor universal control

For H_{b} in Eq. (4.6), the domain in the momentum basis is

$$\mathcal{D}(H_{\mathrm{b}}) = \left\{ \psi = \sum_{\ell \in \mathbb{Z}} \psi_\ell |\ell\rangle : \sum_{\ell \in \mathbb{Z}} |\ell^2 + \xi\ell|^2 |\psi_\ell|^2 < \infty \right\}. \tag{C.8}$$

The control operator $\cos\hat{\theta}$ is bounded and self-adjoint, with matrix elements

$$\langle k|\cos\hat{\theta}|\ell\rangle = \frac{1}{2}\left(\delta_{k,\ell+1} + \delta_{k,\ell-1}\right). \tag{C.9}$$

Thus the momentum states form a complete eigenbasis of the drift, and the control couples only neighboring momentum states.

To match the notation of Ref. [28], set $A_{\mathrm{c}} = -iH_{\mathrm{b}}, B_{\mathrm{c}} = -i\cos\hat{\theta}$, and take the control values in a fixed interval $[0, \delta]$. Since $\cos\hat{\theta}$ is bounded and self-adjoint, $H_{\mathrm{b}} + u\cos\hat{\theta}$ is self-adjoint on $\mathcal{D}(H_{\mathrm{b}})$ for every $u \in [0, \delta]$. Its restriction to finite linear combinations of momentum states has this operator as its self-adjoint closure. These facts verify the basis and domain assumptions of the cited controllability theorem [28, 61].

The drift eigenvalues are $\varepsilon_\ell = \ell^2 + \xi\ell$. If $\varepsilon_\ell = \varepsilon_k$, then $(\ell - k)(\ell + k + \xi) = 0$. For distinct integers ℓ and k, the second factor cannot vanish because $\xi \notin \mathbb{Z}$. Hence the spectrum is nondegenerate.

The control couples the transitions $|\ell\rangle \longleftrightarrow |\ell+1\rangle$, whose transition frequencies are $|\varepsilon_{\ell+1} - \varepsilon_\ell| = |2\ell+1+\xi|$. Suppose that two such frequencies are equal: $|2\ell + 1 + \xi| = |2k + 1 + \xi|$. Either $2\ell + 1 + \xi = 2k + 1 + \xi$, which gives $\ell = k$, or $2\ell + 1 + \xi = -(2k + 1 + \xi)$, which requires $\ell + k + 1 + \xi = 0$. The latter is impossible because $\xi \notin \mathbb{Z}$. Therefore the nearest-neighbor transition frequencies are pairwise distinct.

These nearest-neighbor transitions connect all momentum states $|\ell\rangle$, $\ell \in \mathbb{Z}$, and hence form a nonresonant connectedness chain in the sense of Ref. [28, Definition 2.5]. The nondegenerate spectrum also makes the condition on degenerate energy levels automatic. Thus the hypotheses of Theorem 2.11 in Ref. [28] are satisfied. The conclusion of that theorem is approximate simultaneous controllability in the sense of Ref. [28, Definition 2.10], namely approximation of a prescribed unitary on any finite set of states. The phase-adjustment argument uses the unbounded-spectrum case of Ref. [28, Lemma 6.3], and the present drift spectrum $\varepsilon_\ell = \ell^2 + \xi\ell$ is unbounded.

D Gauge-model calculations

D.1 Gauge invariance and the Pauli form of hopping

Gauge invariance. For the oriented link $e = (a, b)$, temporarily omit the factor ζ_{ab} and define the forward hopping operator

$$T_{ab} = \sigma_a^+ S_{ab} U_{ab} \sigma_b^-. \tag{D.1}$$

The required commutators are

$$[\hat{n}_a, \sigma_a^+] = \sigma_a^+, \qquad [\hat{n}_b, \sigma_b^-] = -\sigma_b^-, \qquad [E_{ab}, U_{ab}] = U_{ab}. \tag{D.2}$$

By construction, the Jordan–Wigner string S_{ab} contains neither endpoint and therefore commutes with $\hat{n}_a$ and $\hat{n}_b$. The background charge b_n and external charge q_n^{ext} are scalar terms and do not contribute to the commutators.

The link $e = (a, b)$ enters the Gauss-law generator with sign $+1$ at a and sign -1 at b. Hence

$$\begin{aligned} [G_a, T_{ab}] &= [E_{ab} - \hat{n}_a, T_{ab}] = T_{ab} - T_{ab} = 0, \\ [G_b, T_{ab}] &= [-E_{ab} - \hat{n}_b, T_{ab}] = -T_{ab} + T_{ab} = 0. \end{aligned} \tag{D.3}$$

Every other Gauss-law generator commutes with T_{ab}, and the same calculation applies to $T_{ab}^{\dagger}$. Therefore $[G_n, H_{K,ab}] = 0$ for every n.

The electric and mass terms are functions of the mutually commuting operators E_e and $\hat{n}_n$, and hence commute with every G_n. For the magnetic term, a plaquette operator changes the link fluxes by the oriented boundary of the plaquette. The incidence and boundary matrices satisfy $DB^{\mathsf{T}} = 0$, so the plaquette operators also commute with every Gauss-law generator. Consequently, $[G_n, H] = 0$ for every n.

Pauli form of the hopping term. With the occupation convention in Eq. (5.4), $\sigma^+ = \frac{X+iY}{2}, \sigma^- = \frac{X-iY}{2}$. Substituting these expressions together with $\zeta_{ab} = e^{i\delta_{ab}}$ and $U_{ab} = e^{i\hat{\theta}_{ab}}$ gives

$$\zeta_{ab} T_{ab} + \zeta_{ab}^* T_{ab}^{\dagger} = \frac{1}{2}\Big[\cos(\hat{\theta}_{ab} + \delta_{ab})(X_a S_{ab} X_b + Y_a S_{ab} Y_b) + \sin(\hat{\theta}_{ab} + \delta_{ab})(X_a S_{ab} Y_b - Y_a S_{ab} X_b)\Big]. \tag{D.4}$$

Multiplying by $\kappa/2$ gives Eq. (5.15).

D.2 Full-space hopping realization

Consider first the controlled shift using the qubit at site a as the control: $V_{ab}^{(a)} = |0\rangle\langle 0|_a \otimes I_e + |1\rangle\langle 1|_a \otimes U_e^{\dagger}$. With the occupation convention used here, $\sigma_a^+ = |0\rangle\langle 1|_a, \sigma_a^- = |1\rangle\langle 0|_a$. Direct multiplication gives

$$V_{ab}^{(a)} \sigma_a^+ V_{ab}^{(a)\dagger} = \sigma_a^+ \otimes U_e, \qquad V_{ab}^{(a)} \sigma_a^- V_{ab}^{(a)\dagger} = \sigma_a^- \otimes U_e^{\dagger}. \tag{D.5}$$

Alternatively, using the qubit at site b as the control gives $V_{ab}^{(b)} = |0\rangle\langle 0|_b \otimes I_e + |1\rangle\langle 1|_b \otimes U_e$, and

$$V_{ab}^{(b)} \sigma_b^- V_{ab}^{(b)\dagger} = \sigma_b^- \otimes U_e, \qquad V_{ab}^{(b)} \sigma_b^+ V_{ab}^{(b)\dagger} = \sigma_b^+ \otimes U_e^{\dagger}. \tag{D.6}$$

The Jordan–Wigner string S_{ab} acts only on the sites between a and b in the chosen ordering. It therefore commutes with both $V_{ab}^{(a)}$ and $V_{ab}^{(b)}$. Substitution into Eq. (5.19) gives Eq. (5.21) for either choice of control qubit.

For $\delta_{ab} = 0$, define $P_1 = X_a S_{ab} X_b$ and $P_2 = Y_a S_{ab} Y_b$. At sites a and b, the Pauli operators X and Y anticommute. The two minus signs cancel, and the Pauli factors on all other sites are identical. Hence $[P_1, P_2] = 0$. The qubit exchange Hamiltonian therefore becomes $H_{ab}^{(q)}(0) = \frac{\kappa}{4}(P_1 + P_2)$.

Let $R_a(\delta) = e^{i\delta Z_a/2}$. Its action on the qubit raising and lowering operators is

$$R_a(\delta)\sigma_a^+ R_a(\delta)^{\dagger} = e^{i\delta}\sigma_a^+, \qquad R_a(\delta)\sigma_a^- R_a(\delta)^{\dagger} = e^{-i\delta}\sigma_a^-. \tag{D.7}$$

Consequently, $H_{ab}^{(q)}(\delta) = R_a(\delta) H_{ab}^{(q)}(0) R_a(\delta)^{\dagger}$. Since P_1 and P_2 commute,

$$e^{-i\tau H_{ab}^{(q)}(\delta_{ab})} = R_a(\delta_{ab}) e^{-i\tau\kappa P_1/4} e^{-i\tau\kappa P_2/4} R_a(\delta_{ab})^{\dagger}, \tag{D.8}$$

which proves Eq. (5.22).

D.3 Projected and cyclic shifts

For the projector Π_L in Eq. (5.23), the projected shift acts as

$$U_{e,L}|\ell\rangle = \begin{cases} |\ell + 1\rangle, & -L \le \ell < L, \\ 0, & \ell = L. \end{cases} \tag{D.9}$$

Its adjoint acts as

$$U_{e,L}^{\dagger}|\ell\rangle = \begin{cases} |\ell-1\rangle, & -L < \ell \leq L, \\ 0, & \ell = -L. \end{cases} \tag{D.10}$$

Computing $U_{e,L}^{\dagger}U_{e,L}$ and $U_{e,L}U_{e,L}^{\dagger}$ gives Eq. (5.24).

The operator $\widetilde{U}_{e,L}$ in Eq. (5.26) cyclically permutes the $2L+1$ momentum states and is therefore unitary. For every nonboundary momentum state,

$$[E_{e,L}, \widetilde{U}_{e,L}]|\ell\rangle = \widetilde{U}_{e,L}|\ell\rangle, \qquad -L \leq \ell < L. \tag{D.11}$$

For the boundary state $|L\rangle$,

$$[E_{e,L}, \widetilde{U}_{e,L}]|L\rangle = -2L|-L\rangle. \tag{D.12}$$

Since $\left(\widetilde{U}_{e,L} - (2L+1)|-L\rangle\langle L|\right)|L\rangle = -2L|-L\rangle$, these relations give Eq. (5.27).

A finite-dimensional controlled shift defined using $\widetilde{U}_{e,L}$ agrees with the full rotor shift for $-L \leq \ell < L$, but maps the boundary state according to $|L\rangle \longmapsto |-L\rangle$.

D.4 Finite Gauss-law basis and numerical details

For the geometry in Fig. 3, the sites are numbered as $1=(0,0)$, $2=(1,0)$, $3=(2,0)$, $4=(0,1)$, $5=(1,1)$, and $6=(2,1)$. The oriented links, listed from tail to head, are $e_1=(1,2)$, $e_2=(2,3)$, $e_3=(4,5)$, $e_4=(5,6)$, $e_5=(1,4)$, $e_6=(2,5)$, and $e_7=(3,6)$. The Jordan–Wigner snake order is $1 \prec 2 \prec 3 \prec 6 \prec 5 \prec 4$. With sites and links in these orders, the incidence matrix is

$$D = \begin{pmatrix} 1 & 0 & 0 & 0 & 1 & 0 & 0 \\ -1 & 1 & 0 & 0 & 0 & 1 & 0 \\ 0 & -1 & 0 & 0 & 0 & 0 & 1 \\ 0 & 0 & 1 & 0 & -1 & 0 & 0 \\ 0 & 0 & -1 & 1 & 0 & -1 & 0 \\ 0 & 0 & 0 & -1 & 0 & 0 & -1 \end{pmatrix}. \tag{D.13}$$

Ordering the plaquettes as (p_1, p_2) gives

$$B = \begin{pmatrix} 1 & 0 & -1 & 0 & -1 & 1 & 0 \\ 0 & 1 & 0 & -1 & 0 & -1 & 1 \end{pmatrix} = \begin{pmatrix} b_{p_1}^{\mathsf{T}} \\ b_{p_2}^{\mathsf{T}} \end{pmatrix}, \qquad DB^{\mathsf{T}} = 0. \tag{D.14}$$

Set $q_n^{\mathrm{ext}} = 0$. For occupation eigenvalues $\mathbf{o} = (o_n)_n$, defined by $\hat{n}_n|\mathbf{o};E\rangle = o_n|\mathbf{o};E\rangle$, the finite physical basis is

$$\mathcal{B}_L = \{|\mathbf{o};E\rangle : o_n \in \{0,1\}, \quad |E_e| \leq L, \quad DE = \mathbf{o} - \mathbf{b}\}. \tag{D.15}$$

For each allowed $\mathbf{o}$, choose one integer solution $E_0(\mathbf{o})$ of $DE_0 = \mathbf{o} - \mathbf{b}$. On the open 2×1 strip, every solution can be written as

$$E = E_0(\mathbf{o}) + B^{\mathsf{T}}h, \qquad h \in \mathbb{Z}^2, \qquad |E_e| \leq L. \tag{D.16}$$

The two integer components of h are enumerated subject to the final flux bounds.

The diagonal terms act by

$$H_E|\mathbf{o};E\rangle = \frac{g^2}{2}\left(\sum_e E_e^2\right)|\mathbf{o};E\rangle, \tag{D.17}$$

$$H_M|\mathbf{o};E\rangle = m_0\left(\sum_n \eta_n o_n\right)|\mathbf{o};E\rangle. \tag{D.18}$$

Let $b_p = (B_{pe})_e$ denote the oriented flux vector around plaquette p. The magnetic term acts as

$$H_B|\mathbf{o};E\rangle = \frac{N_p}{g^2 a_{\mathrm{lat}}^2}|\mathbf{o};E\rangle - \frac{1}{2g^2 a_{\mathrm{lat}}^2}\sum_p\left(|\mathbf{o};E+b_p\rangle + |\mathbf{o};E-b_p\rangle\right), \tag{D.19}$$

where a state is omitted when any final flux lies outside the window.

For $e = (a, b)$, let I_{ab} be the sites strictly between the two endpoints in the Jordan–Wigner ordering and set

$$s_{ab}(\mathbf{o}) = (-1)^{\sum_{m \in I_{ab}} o_m}. \tag{D.20}$$

When $o_a = 0$ and $o_b = 1$, the forward hopping rule at $\zeta_{ab} = 1$ is

$$H_{K,ab}|\mathbf{o}; E\rangle \supset \frac{\kappa}{2} s_{ab}(\mathbf{o})|\mathbf{o}^{a\leftarrow b}; E + \delta_e\rangle. \tag{D.21}$$

Here δ_e is the unit flux vector on link e, and $\mathbf{o}^{a\leftarrow b}$ moves one matter occupation from b to a. For $o_a = 1$ and $o_b = 0$, the reverse rule is

$$H_{K,ab}|\mathbf{o}; E\rangle \supset \frac{\kappa}{2} s_{ab}(\mathbf{o})|\mathbf{o}^{b\leftarrow a}; E - \delta_e\rangle. \tag{D.22}$$

Terms whose final flux leaves the window are omitted. The two rules are adjoints and preserve the finite Gauss-law basis.

The finite-flux cutoff calculation uses the parameters and cutoffs listed in Sec. 5.4. For $L = 1, 2, 3, 4, 6$, the dimensions of the physical basis are $90, 302, 634, 1086$, and 2350. The $L = 1$ matrix was diagonalized with `scipy.linalg.eigh`; for $L \geq 2$ we used the shift-invert solver `scipy.sparse.linalg.eigsh` with tolerance 2×10^{-11}. Over the full scan, the largest residual of the two computed eigenpairs satisfies

$$\max_k \|H\psi_k - \mathcal{E}_k\psi_k\|_2 \leq 6.51 \times 10^{-10}. \tag{D.23}$$

The numerical environment used Python 3.11.4, NumPy 2.4.6, SciPy 1.17.1, and Matplotlib 3.10.9.

The processed data also record the link-averaged boundary occupation

$$\overline{p}_{\partial L} = \frac{1}{N_\ell} \sum_e \left\langle \mathbf{1}_{\{|E_e|=L\}} \right\rangle. \tag{D.24}$$

Its maximum over the scan decreases from 1.05×10^{-2} at $L = 4$ to 6.72×10^{-4} at $L = 6$. Taking $L = 6$ as the largest available cutoff, the maximum absolute differences between $L = 4$ and $L = 6$ are 2.25×10^{-2} for $\overline{W}$, 1.57×10^{-1} for Δ, and 5.79×10^{-1} for $\langle E^2\rangle_{\text{link}}$; all three maxima occur at $g^{-2} = 10$. On the sampled interval $g^{-2} \leq 1$, the corresponding maxima are 1.34×10^{-8}, 4.69×10^{-10}, and 7.23×10^{-9}.

The plaquette expectation values use the same projected shifts as Eq. (D.19); the remaining observables are diagonal in the flux basis. These data give the three panels in Fig. 4.

For Fig. 5, the initial state is $|\mathbf{o} = \mathbf{b}; E = \mathbf{0}\rangle$. The projected Hamiltonian was exponentiated on the finite Gauss-law basis for $L = 1, 2, 3, 4$, $g^{-2} = 1$, and $0 \leq t \leq 8$ using 241 equally spaced time points. Across all reported calculations, the maximum norm error was 5.67×10^{-13} and the maximum total-matter-number error was 1.70×10^{-12}.

Table 6: Real-time cutoff comparison on the 241 equally spaced sample times in $0 \leq t \leq 8$. The first six rows compare the successive cutoffs $L = 2, 3, 4$; the final two rows report the largest link-averaged boundary occupation at $L = 3$ and $L = 4$.

Diagnostic	Maximum over the sampled times
$\lvert\overline{W}_2(t) - \overline{W}_3(t)\rvert$	1.33×10^{-2}
$\lvert C_{12,2}(t) - C_{12,3}(t)\rvert$	1.18×10^{-2}
$\lvert I_{M,2}(t) - I_{M,3}(t)\rvert$	4.72×10^{-3}
$\lvert\overline{W}_3(t) - \overline{W}_4(t)\rvert$	9.99×10^{-5}
$\lvert C_{12,3}(t) - C_{12,4}(t)\rvert$	2.28×10^{-4}
$\lvert I_{M,3}(t) - I_{M,4}(t)\rvert$	3.54×10^{-5}
$\overline{p}_{\partial L}(t)$ at $L = 3$	7.60×10^{-5}
$\overline{p}_{\partial L}(t)$ at $L = 4$	2.84×10^{-7}

E Calculations for rotor quantum phase estimation

E.1 Fejér kernel and weak convergence for direct-angle readout

For $\Delta \notin 2\pi\mathbb{Z}$, the finite geometric series satisfies

$$\sum_{\ell=0}^{d-1} e^{-i\ell\Delta} = e^{-i(d-1)\Delta/2}\frac{\sin(d\Delta/2)}{\sin(\Delta/2)}. \tag{E.1}$$

The angle-state convention in Sec. 2.1 gives

$$\langle\theta|\chi_d(\varphi)\rangle_R = \frac{1}{\sqrt{2\pi d}}\sum_{\ell=0}^{d-1} e^{i\ell(\theta-\varphi)}. \tag{E.2}$$

Taking the squared modulus and using Eq. (E.1) gives Eq. (6.12).

The density is normalized because

$$\int_0^{2\pi} e^{i(\ell-k)\theta}\,d\theta = 2\pi\delta_{\ell k}. \tag{E.3}$$

Therefore

$$\int_0^{2\pi} p_d(\theta \mid \varphi)\,d\theta = \frac{1}{d}\sum_{\ell,k=0}^{d-1}\delta_{\ell k} = 1. \tag{E.4}$$

The numerator of Eq. (6.12) vanishes when $\theta-\varphi = \frac{2\pi m}{d} \pmod{2\pi}, m \in \mathbb{Z}$. The closest nonzero choices are $m = \pm 1$, so the first zeros occur at circular distance $\frac{2\pi}{d}$ from the central maximum at $\theta = \varphi$.

Moreover,

$$2\pi p_d(\theta \mid \varphi) = K_{d-1}(\theta-\varphi), \tag{E.5}$$

where K_{d-1} is the periodic Fejér kernel of order $d-1$. A standard property of the Fejér kernels gives, for every continuous 2π-periodic function f,

$$\lim_{d\to\infty}\int_0^{2\pi} f(\theta)p_d(\theta \mid \varphi)\,d\theta = f(\varphi). \tag{E.6}$$

Thus the probability distribution becomes concentrated at $\theta = \varphi$ as d increases.

E.2 Finite-support probe optimization

Let

$$\Pi_L := \sum_{\ell=-L}^{L} |\ell\rangle\langle\ell|, \qquad X_{R,L} := \Pi_L X_R(1)\Pi_L. \tag{E.7}$$

Conjugation by $Z_R(\phi)$ gives

$$Z_R(\phi)^\dagger X_{R,L} Z_R(\phi) = e^{-i\phi}X_{R,L}. \tag{E.8}$$

The phase of $\langle\eta|X_{R,L}|\eta\rangle$ can therefore be removed without changing the momentum support. With both maxima taken over normalized states in $\Pi_L\mathcal{H}_{0,1}$,

$$\max_{\|\eta\|=1}|\langle\eta|X_{R,L}|\eta\rangle| = \max_{\|\eta\|=1}\left\langle\eta\,\middle|\,\frac{X_{R,L}+X_{R,L}^\dagger}{2}\,\middle|\,\eta\right\rangle. \tag{E.9}$$

In the ordered basis $|-L\rangle, \ldots, |L\rangle$, the Hermitian operator on the right is the path matrix with $1/2$ on its first off-diagonals. Its largest eigenvalue and a normalized eigenvector are

$$\cos\!\left(\frac{\pi}{2(L+1)}\right), \qquad \frac{1}{\sqrt{L+1}}\sum_{\ell=-L}^{L}\cos\!\left(\frac{\pi\ell}{2(L+1)}\right)|\ell\rangle. \tag{E.10}$$

This proves the fixed-support optimality of Eq. (6.23) and the value of $R_{\cos}$ used in Eq. (6.25).

Set $\alpha = \pi/[2(L+1)]$. The energy of the cosine-window probe is

$$E_{\cos} = \frac{1}{L+1} \sum_{\ell=-L}^{L} \ell^2 \cos^2(\alpha\ell). \tag{E.11}$$

Using $\cos^2 t = (1 + \cos 2t)/2$ and differentiating the Dirichlet kernel gives

$$\sum_{\ell=-L}^{L} \ell^2 = \frac{L(L+1)(2L+1)}{3}, \qquad \sum_{\ell=-L}^{L} \ell^2 \cos(2\alpha\ell) = (L+1)\big[L+1-\csc^2\alpha\big]. \tag{E.12}$$

Substitution gives Eq. (6.27). The expansion

$$\csc^2\alpha = \alpha^{-2} + \frac{1}{3} + \frac{\alpha^2}{15} + O(\alpha^4) \tag{E.13}$$

then gives Eq. (6.28), and combining this result with Eq. (6.25) proves Eq. (6.29).

E.3 Fixed-energy probe asymptotics

For large λ, the ground state of Eq. (6.31) is localized near $\theta = 0$. Expanding the potential gives

$$-\lambda\cos\theta = -\lambda + \frac{\lambda}{2}\theta^2 + O(\lambda\theta^4), \tag{E.14}$$

so the leading local Hamiltonian is

$$H_\lambda + \lambda \simeq \hat{\ell}^2 + \frac{\lambda}{2}\theta^2. \tag{E.15}$$

The ground-state variances in this local quadratic approximation satisfy

$$\langle\hat{\ell}^2\rangle \sim \sqrt{\frac{\lambda}{8}}, \qquad \langle\theta^2\rangle \sim \frac{1}{\sqrt{2\lambda}}. \tag{E.16}$$

Writing $E_R = \langle\hat{\ell}^2\rangle$ gives $\lambda \sim 8E_R^2$ and $\langle\theta^2\rangle \sim 1/(4E_R)$. Since $1 - \cos\theta \sim \theta^2/2$ on the localized ground state,

$$V_\star(E_R) \sim \frac{1}{8E_R}, \qquad \Delta_\star \sim \frac{1}{2\sqrt{E_R}}. \tag{E.17}$$

The localization width tends to zero as λ grows, so periodic-boundary corrections do not change the leading terms.

F Angle–momentum construction of the rotor QFT

F.1 Code-space realization of the mixed angle–momentum phase

Let $\overline{\psi}_x(\theta) := \langle\theta|\overline{x}\rangle$ and $\Pi_A := \sum_{x=0}^{d-1} |\overline{x}\rangle\langle\overline{x}|$. Choose pairwise disjoint measurable angular cores C_x and a bounded real periodic function g satisfying $g(\theta) = x$ on C_x. Write M_g for multiplication by g and define

$$\eta_x := \int_{\mathbb{T}\setminus C_x} |\overline{\psi}_x(\theta)|^2 \, d\theta, \qquad \Delta_x := \operatorname*{ess\,sup}_{\theta \notin C_x} |g(\theta) - x|. \tag{F.1}$$

The xth column of $(M_g - D_A)\Pi_A$ is $(g - x)\overline{\psi}_x$. The operator norm is bounded by the Hilbert–Schmidt norm, and hence

$$\delta_g := \big\|(M_g - D_A)\Pi_A\big\| \leq \left(\sum_{x=0}^{d-1} \Delta_x^2 \eta_x\right)^{1/2}. \tag{F.2}$$

Thus the error is controlled by the weight of the orthonormalized codewords outside their assigned cores. If $0 \leq g \leq d-1$, then $\delta_g \leq (d-1)(\sum_x \eta_x)^{1/2}$.

Let $\Pi := \Pi_{M,j} \otimes \Pi_{A,k}$. The Duhamel formula and $\|D_M\| = d-1$ give

$$\big\|[e^{i\beta D_{M,j} \otimes M_{g,k}} - \Lambda_{jk}(\beta)]\Pi\big\| \leq |\beta|(d-1)\delta_g. \tag{F.3}$$

Since the logical operation preserves the code space, the same estimate bounds leakage:

$$\big\|(I - \Pi)e^{i\beta D_{M,j} \otimes M_{g,k}}\Pi\big\| \leq |\beta|(d-1)\delta_g. \tag{F.4}$$

For the CPHS realization in Eq. (7.39), take $f_n = \delta_{n0}$. Then

$$\mathrm{CPHS}_{jk}(\beta)|p\rangle_{R_j}|x\rangle_{R_k} = e^{i\beta px}|p\rangle_{R_j}|x\rangle_{R_k}. \tag{F.5}$$

Conjugating by T_k proves Eq. (7.39). For the general residue-class code,

$$\mathrm{CPHS}_{jk}(\beta)|\overline{p}\rangle_{R_j}|\overline{x}\rangle_{R_k} = \sum_{n,m\in\mathbb{Z}} f_n f_m e^{i\beta(p+nd)(x+md)}|p+nd\rangle_{R_j}|x+md\rangle_{R_k}. \tag{F.6}$$

The n, m-dependent phases generally prevent the codeword from acquiring a uniform logical phase $e^{i\beta px}$.

F.2 Base-d Fourier phase identity

For digits $x_k, p_j \in \{0, \ldots, d-1\}$, write $\mathbf{x} = (x_1, \ldots, x_r)$ and $\mathbf{p} = (p_1, \ldots, p_r)$, and define

$$X(\mathbf{x}) = \sum_{k=1}^{r} x_k d^{r-k}, \qquad P_{\mathrm{rev}}(\mathbf{p}) = \sum_{j=1}^{r} p_j d^{j-1}. \tag{F.7}$$

Expanding the product in Eq. (F.7) gives

$$\frac{X(\mathbf{x})P_{\mathrm{rev}}(\mathbf{p})}{d^r} - \sum_{1\leq j\leq k\leq r} \frac{p_j x_k}{d^{k-j+1}} = \sum_{j>k} p_j x_k d^{j-k-1} \in \mathbb{Z}. \tag{F.8}$$

Consequently,

$$\exp\left[\frac{2\pi i X(\mathbf{x})P_{\mathrm{rev}}(\mathbf{p})}{d^r}\right] = \exp\left[2\pi i \sum_{1\leq j\leq k\leq r} \frac{p_j x_k}{d^{k-j+1}}\right]. \tag{F.9}$$

If $y_j = p_{r-j+1}$, then $P_{\mathrm{rev}}(\mathbf{p}) = \sum_{j=1}^{r} y_j d^{r-j}$, and

$$\bigotimes_{j=1}^{r} |\overline{p_j}\rangle_{R_j} = \mathrm{REV}_r \bigotimes_{j=1}^{r} |\overline{y_j}\rangle_{R_j}. \tag{F.10}$$

Hence REV_r relates the physical and standard digit orders.

F.3 Proof of the angle–momentum factorization

Consider the angle-code basis state

$$|\overline{\mathbf{x}}\rangle = \bigotimes_{k=1}^{r} |\overline{x_k}\rangle_{R_k}, \qquad \mathbf{x} = \big(x_1, \ldots, x_r\big). \tag{F.11}$$

Write $X(\mathbf{x})$ for the associated input integer in Eq. (F.7).

When processing register R_j, the local angle-to-momentum transform gives

$$F_{d,j}^{A\to M} |\overline{x_j}\rangle_{R_j} = \frac{1}{\sqrt{d}} \sum_{p_j=0}^{d-1} \exp\!\left(\frac{2\pi i}{d} p_j x_j\right) |\overline{p_j}\rangle_{R_j}. \tag{F.12}$$

For each $k > j$, the operation $\Lambda_{jk}(2\pi/d^{k-j+1})$ contributes

$$\exp\!\left(\frac{2\pi i}{d^{k-j+1}} p_j x_k\right). \tag{F.13}$$

The total contribution associated with p_j is therefore

$$\exp\left[2\pi i p_j \sum_{k=j}^{r} \frac{x_k}{d^{k-j+1}}\right]. \tag{F.14}$$

Multiplying the contributions from all r register steps gives

$$U_{\mathrm{AM}} |\overline{\mathbf{x}}\rangle = \frac{1}{\sqrt{d^r}} \sum_{p_1,\ldots,p_r=0}^{d-1} \exp\left[2\pi i \sum_{1\le j\le k\le r} \frac{p_j x_k}{d^{k-j+1}}\right] \times \bigotimes_{j=1}^{r} |\overline{p_j}\rangle_{R_j}. \tag{F.15}$$

The local transforms give the terms $j = k$ in the exponent of Eq. (F.15), and the mixed angle–momentum phases give the terms $j < k$. Eq. (F.9) identifies their product with the standard d^r-point Fourier phase and gives the register-order reversal. Comparing Eq. (F.15) with the definition of $F_N^{A\to M}$ now gives

$$U_{\mathrm{AM}} |\overline{\mathbf{x}}\rangle = \mathrm{REV}_r F_N^{A\to M} |\overline{\mathbf{x}}\rangle. \tag{F.16}$$

Since the states $|\overline{\mathbf{x}}\rangle$ form a basis of $\mathcal{A}_d^{\otimes r}$, Eq. (F.16) proves Eq. (7.37).

G Gate-set compilation of rotor QFTs

G.1 Verification of the one-rotor momentum-code QFT

To verify Eq. (7.50), write $p = \sum_{k=0}^{s-1} 2^k p_k$, with $p_k \in \{0,1\}$, and consider the jth stage $F_j = B_j S_j^\dagger C_j (H_a \otimes I_R) S_j B_j^\dagger$. Immediately before this stage, the downward-induction invariant is

$$\ell_j = \sum_{k=0}^{j} 2^k p_k + \sum_{k=j+1}^{s-1} 2^k c_k. \tag{G.1}$$

The positions $0,\dots,j$ retain the corresponding input bits, while the higher positions contain the output bits already generated. Removing bit p_j gives $u_j = \ell_j - 2^j p_j$, whose jth binary digit is zero.

The gates $B_j^\dagger$ and S_j extract p_j into the ancilla and remove that bit from the rotor momentum. The Hadamard and the conditional phase produce the superposition over c_j, after which $S_j^\dagger$ writes c_j into the vacant position and B_j resets the ancilla. Their combined action is

$$F_j\big(|0\rangle_a \otimes |\overline{\ell_j}\rangle_R\big) = \frac{|0\rangle_a}{\sqrt{2}} \otimes \sum_{c_j=0}^{1} (-1)^{c_j p_j} e^{i\alpha_j c_j u_j} |\overline{u_j + 2^j c_j}\rangle_R. \tag{G.2}$$

For $j=0$, the integer u_0 is even and $\alpha_0 = \pi$, so C_0 acts trivially on every state reached in that stage and may be omitted.

The invariant holds initially because $\ell_{s-1} = p$. Equation (G.2) replaces p_j by c_j and leaves all other binary positions unchanged, producing the invariant for stage $j-1$. Moreover,

$$(-1)^{c_j p_j} e^{i\alpha_j c_j u_j} = \exp\left[2\pi i c_j \sum_{k=0}^{j} \frac{p_k}{2^{j-k+1}}\right], \tag{G.3}$$

because the terms containing previously generated bits are integer multiples of 2π in the exponent. Downward induction therefore gives

$$F_0 F_1 \cdots F_{s-1}\big(|0\rangle_a \otimes |\overline{p}\rangle_R\big) = \frac{|0\rangle_a}{\sqrt{d}} \otimes \sum_{c_0,\dots,c_{s-1}=0}^{1} \exp\left[2\pi i \sum_{j=0}^{s-1} c_j \sum_{k=0}^{j} \frac{p_k}{2^{j-k+1}}\right] \left|\overline{\sum_{j=0}^{s-1} 2^j c_j}\right\rangle_R. \tag{G.4}$$

After the internal binary reversal, set $y = \sum_{j=0}^{s-1} 2^{s-1-j} c_j$. Expanding py/d shows that the omitted terms are integers and hence

$$e^{2\pi i p y/d} = \exp\left[2\pi i \sum_{j=0}^{s-1} c_j \sum_{k=0}^{j} \frac{p_k}{2^{j-k+1}}\right]. \tag{G.5}$$

The map from $(c_0,\dots,c_{s-1})$ to y is a bijection, so

$$\widetilde{\mathrm{BREV}}_s F_0 F_1 \cdots F_{s-1}\big(|0\rangle_a \otimes |\overline{p}\rangle_R\big) = \frac{|0\rangle_a}{\sqrt{d}} \otimes \sum_{y=0}^{d-1} e^{2\pi i p y/d} |\overline{y}\rangle_R = |0\rangle_a \otimes F_d^M |\overline{p}\rangle_R. \tag{G.6}$$

This proves Eq. (7.50).

The Fourier-stage sequence remains inside $\mathcal{M}_d^{(0)}$. Each S_j removes one occupied binary digit and each $S_j^\dagger$ writes into the vacant position, so no borrow or carry occurs.

G.2 Binary bit reversal within one rotor momentum code

For $0 \le \mu < \nu < s$, let

$$P_{10}^{\mu\nu} = \sum_{\substack{0 \le p < d \\ p_\mu = 1,\ p_\nu = 0}} |\overline{p}\rangle_R \langle \overline{p}|_R, \qquad P_{01}^{\mu\nu} = \sum_{\substack{0 \le p < d \\ p_\mu = 0,\ p_\nu = 1}} |\overline{p}\rangle_R \langle \overline{p}|_R. \tag{G.7}$$

Define the momentum-dependent ancilla rotations

$$R_{10}^{\mu\nu} = (-iY_a) \otimes P_{10}^{\mu\nu} + I_a \otimes (I_R - P_{10}^{\mu\nu}), \qquad R_{01}^{\mu\nu} = (iY_a) \otimes P_{01}^{\mu\nu} + I_a \otimes (I_R - P_{01}^{\mu\nu}). \tag{G.8}$$

These are MQR operations used in the gate-set compilation. With $\Delta_{\mu\nu} = 2^\nu - 2^\mu$, set

$$S_{\mu\nu} = R_{10}^{\mu\nu} \mathrm{CShift}_{a\to R}(-\Delta_{\mu\nu}) R_{01}^{\mu\nu} \mathrm{CShift}_{a\to R}(\Delta_{\mu\nu}) R_{10}^{\mu\nu}. \tag{G.9}$$

A direct check of the four patterns $00, 01, 10, 11$ shows that $S_{\mu\nu}$ exchanges bits μ and ν, returns the ancilla to $|0\rangle_a$, and never leaves the code.

The complete binary reversal exchanges the disjoint pairs $(0, s-1), (1, s-2), \ldots$. Define

$$\widetilde{\mathrm{BREV}}_s = \prod_{\mu=0}^{\lfloor s/2\rfloor - 1} S_{\mu, s-1-\mu}. \tag{G.10}$$

If $z = \sum_{\mu=0}^{s-1} 2^\mu z_\mu$, then $\mathrm{rev}_s(z) = \sum_{\mu=0}^{s-1} 2^{s-1-\mu} z_\mu$, and

$$\widetilde{\mathrm{BREV}}_s\big(|0\rangle_a \otimes |\overline{z}\rangle_R\big) = |0\rangle_a \otimes |\overline{\mathrm{rev}_s(z)}\rangle_R = |0\rangle_a \otimes \mathrm{BREV}_s |\overline{z}\rangle_R. \tag{G.11}$$

For $s = 1$, the product is empty and acts as the identity on $|0\rangle_a \otimes \mathcal{M}_2^{(0)}$. The operation count is recorded in Appendix G.4.

G.3 Verification of the compiled base-d QFT

We suppress the reusable ancilla from the notation, since it is initialized in $|0\rangle_a$ and returned to $|0\rangle_a$ after each compiled one-rotor transform.

For $\mathbf{x} = \big(x_1, \ldots, x_r\big), \qquad \mathbf{p} = \big(p_1, \ldots, p_r\big)$, write

$$|\overline{\mathbf{x}}\rangle_R := \bigotimes_{k=1}^{r} |\overline{x_k}\rangle_{R_k}, \quad |\overline{\mathbf{p}}\rangle_R := \bigotimes_{j=1}^{r} |\overline{p_j}\rangle_{R_j}. \tag{G.12}$$

When register R_j is processed, the local transform $F_{d,j}^M$ contributes the phase $\exp\!\Big(\frac{2\pi i p_j x_j}{d}\Big)$. At that point, every register R_k with $k > j$ still carries its input digit x_k. Hence $\mathrm{CPHS}_{jk}\,\big(\frac{2\pi}{d^{k-j+1}}\big)$ contributes $\exp\!\Big(\frac{2\pi i p_j x_k}{d^{k-j+1}}\Big)$.

Multiplying all local and cross-register phases gives

$$U_{\mathrm{QFT}} |\overline{\mathbf{x}}\rangle_R = \frac{1}{\sqrt{d^r}} \sum_{\mathbf{p}\in\{0,\ldots,d-1\}^r} \exp\left[2\pi i \sum_{1\le j\le k\le r} \frac{p_j x_k}{d^{k-j+1}}\right] |\overline{\mathbf{p}}\rangle_R. \tag{G.13}$$

The terms with $j = k$ are generated by the local transforms $F_{d,j}^M$, and the terms with $j < k$ are generated by the CPHS gates.

By Eq. (F.9), the phase in Eq. (G.13) is

$$\exp\left[2\pi i \sum_{1\le j\le k\le r} \frac{p_j x_k}{d^{k-j+1}}\right] = \exp\left[\frac{2\pi i X(\mathbf{x}) P_{\mathrm{rev}}(\mathbf{p})}{d^r}\right]. \tag{G.14}$$

The same derivation shows that the physical ordering of the digits $p_1, \ldots, p_r$ differs from the standard base-d output ordering by REV_r. Since $\mathbf{p} \longmapsto P_{\mathrm{rev}}(\mathbf{p})$ is a bijection from $\{0, \ldots, d-1\}^r$ to $\{0, \ldots, d^r - 1\}$, it follows that

$$U_{\mathrm{QFT}} |\overline{\mathbf{x}}\rangle_R = \mathrm{REV}_r F_N^M |\overline{\mathbf{x}}\rangle_R. \tag{G.15}$$

The states $|\overline{\mathbf{x}}\rangle_R$ form a basis of $(\mathcal{M}_d^{(0)})^{\otimes r}$. Linearity therefore gives Eq. (7.54).

G.4 Logical instruction counts

Each CShift by an arbitrary integer amount, MQR, conditional-phase, CPHS, and Hadamard gate is counted as one logical instruction. Set $f_s = \lfloor s/2 \rfloor$.

At stage $j = 0$, the reduced momentum is even and $\alpha_0 = \pi$. The gate $C_0 = C_{c_a,1}(\pi)$ therefore acts trivially on every state reached in that stage, leaving $s-1$ nontrivial conditional-phase gates.

Table 7: Logical instruction counts for the explicit momentum-code QFT compilation. Each CShift of arbitrary size, MQR, conditional-phase, CPHS, and Hadamard gate counts as one instruction.

Operation	Logical instruction count
One compiled d-point rotor QFT F_d^M	$(2s+3f_s)$ MQR $+(2s+2f_s)$ CShift $+s$ Hadamard gates $+(s-1)$ conditional-phase gates C_j
Compiled base-d QFT on r rotor momentum codes	r applications of F_d^M $+\binom{r}{2}$ CPHS
Qubit–momentum-code transfer, one direction, r registers	rs MQR $+rs$ CShift

References

[1] Chin-wen Chou et al. "Preparation and Coherent Manipulation of Pure Quantum States of a Single Molecular Ion". In: *Nature* 545.7653 (2017), pp. 203–207. DOI: 10.1038/nature22338. URL: https://doi.org/10.1038/nature22338.

[2] Christiane P. Koch, Mikhail Lemeshko, and Dominique Sugny. "Quantum control of molecular rotation". In: *Rev. Mod. Phys.* 91 (3 Sept. 2019), p. 035005. DOI: 10.1103/RevModPhys.91.035005. URL: https://link.aps.org/doi/10.1103/RevModPhys.91.035005.

[3] Erik Urban et al. "Coherent Control of the Rotational Degree of Freedom of a Two-Ion Coulomb Crystal". In: *Phys. Rev. Lett.* 123.13 (2019), p. 133202. DOI: 10.1103/PhysRevLett.123.133202. URL: https://doi.org/10.1103/PhysRevLett.123.133202.

[4] Neil Glikin et al. "Probing Rotational Decoherence with a Trapped-Ion Planar Rotor". In: *Phys. Rev. Lett.* 134 (3 Jan. 2025), p. 033601. DOI: 10.1103/PhysRevLett.134.033601. URL: https://link.aps.org/doi/10.1103/PhysRevLett.134.033601.

[5] Monika Leibscher, Ferdinand Schmidt-Kaler, and Christiane P. Koch. *A Planar Rotor Trapped and Coupled to the Vibrational Modes of an Ion Crystal*. 2025. DOI: 10.48550/arXiv.2504.00590. arXiv: 2504.00590 [quant-ph]. URL: https://arxiv.org/abs/2504.00590.

[6] Lukas Martinetz et al. "Quantum Electromechanics with Levitated Nanoparticles". In: *npj Quantum Information* 6 (2020), p. 101. DOI: 10.1038/s41534-020-00333-7.

[7] J. M. Alcaine-Cuervo et al. *Compact $U(1)$ Lattice Gauge Theory in Superconducting Circuits with Infinite-Dimensional Local Hilbert Spaces*. 2026. DOI: 10.48550/arXiv.2601.23150. arXiv: 2601.23150 [quant-ph]. URL: https://arxiv.org/abs/2601.23150.

[8] Philippe Raynal et al. "Encoding many qubits in a rotor". In: *Phys. Rev. A* 81 (5 May 2010), p. 052327. DOI: 10.1103/PhysRevA.81.052327. URL: https://link.aps.org/doi/10.1103/PhysRevA.81.052327.

[9] Christophe Vuillot, Alessandro Ciani, and Barbara M. Terhal. "Homological Quantum Rotor Codes: Logical Qubits from Torsion". In: *Communications in Mathematical Physics* 405, 53 (2024). DOI: 10.1007/s00220-023-04905-4. URL: https://doi.org/10.1007/s00220-023-04905-4.

[10] Muhammad Shaeer Moeed et al. "Qubit encodings for lattices of dipolar planar rotors". In: *The Journal of Chemical Physics* 163.17 (2025), p. 174103. DOI: 10.1063/5.0292230.

[11] John Kogut and Leonard Susskind. "Hamiltonian formulation of Wilson's lattice gauge theories". In: *Phys. Rev. D* 11 (2 Jan. 1975), pp. 395–408. DOI: 10.1103/PhysRevD.11.395. URL: https://link.aps.org/doi/10.1103/PhysRevD.11.395.

[12] Eleanor Crane et al. "Hybrid Oscillator-Qubit Quantum Processors: Simulating Fermions, Bosons, and Gauge Fields". In: *Physical Review X* (2026). Accepted 23 July 2026. DOI: 10.1103/s5bn-z4jq. arXiv: 2409.03747 [quant-ph]. URL: https://doi.org/10.1103/s5bn-z4jq.

[13] Victor Ale et al. "Simulating quantum electrodynamics in 2+1 dimensions with qubits and qumodes". In: *Journal of High Energy Physics* 2026.4 (2026), p. 122. DOI: 10.1007/JHEP04(2026)122. URL: https://doi.org/10.1007/JHEP04(2026)122.

[14] Heather Leitch, Kenza Hammam, and Gabriele De Chiara. "Thermodynamics of hybrid quantum rotor devices". In: *Phys. Rev. E* 109 (2 Feb. 2024), p. 024108. DOI: 10.1103/PhysRevE.109.024108. URL: https://link.aps.org/doi/10.1103/PhysRevE.109.024108.

[15] A. F. Kemper et al. *Hybrid continuous-discrete-variable quantum computing: a guide to utility*. 2025. DOI: 10.48550/arXiv.2511.13882. arXiv: 2511.13882 [quant-ph]. URL: https://arxiv.org/abs/2511.13882.

[16] Yuan Liu et al. "Hybrid Oscillator-Qubit Quantum Processors: Instruction Set Architectures, Abstract Machine Models, and Applications". In: *PRX Quantum* 7 (1 Jan. 2026), p. 010201. DOI: 10.1103/4rf7-9tfx. URL: https://link.aps.org/doi/10.1103/4rf7-9tfx.

[17] Joel Bierman et al. *Scalable Qumode-Qubit State Transfer and Fast-forward Quantum Fourier Transform using Oscillators*. 2026. DOI: 10.48550/arXiv.2604.12157. arXiv: 2604.12157 [quant-ph]. URL: https://arxiv.org/abs/2604.12157.

[18] Peter van Loock et al. "Hybrid Quantum Computation in Quantum Optics". In: *Physical Review A* 78 (2008), p. 022303. DOI: 10.1103/PhysRevA.78.022303.

[19] Ulrik L. Andersen et al. "Hybrid discrete- and continuous-variable quantum information". In: *Nature Physics* 11.9 (2015), pp. 713–719. ISSN: 1745-2481. DOI: 10.1038/nphys3410. URL: https://doi.org/10.1038/nphys3410.

[20] Stefan Krastanov et al. "Universal Control of an Oscillator with Dispersive Coupling to a Qubit". In: *Phys. Rev. A* 92.4 (2015), p. 040303. DOI: 10.1103/PhysRevA.92.040303. URL: https://doi.org/10.1103/PhysRevA.92.040303.

[21] Alec Eickbusch et al. "Fast Universal Control of an Oscillator with Weak Dispersive Coupling to a Qubit". In: *Nature Physics* 18.12 (2022), pp. 1464–1469. DOI: 10.1038/s41567-022-01776-9. URL: https://doi.org/10.1038/s41567-022-01776-9.

[22] Sayan Chakraborty and Victor V. Albert. "Hybrid Oscillator–Qudit Quantum Processors: Stabilizer States, Stabilizer Codes, Symplectic Operations, and Noncommutative Geometry". In: *PRX Quantum* 7.2 (May 2026), p. 020320. DOI: 10.1103/yr64-ypxt. arXiv: 2508.04819 [quant-ph]. URL: https://doi.org/10.1103/yr64-ypxt.

[23] Victor V. Albert, Saverio Pascazio, and Michel H. Devoret. "General phase spaces: from discrete variables to rotor and continuum limits". In: *Journal of Physics A: Mathematical and Theoretical* 50.50 (2017), p. 504002. DOI: 10.1088/1751-8121/aa9314. URL: https://doi.org/10.1088/1751-8121/aa9314.

[24] Juan Bermejo-Vega, Cedric Yen-Yu Lin, and Maarten Van den Nest. "Normalizer Circuits and a Gottesman–Knill Theorem for Infinite-Dimensional Systems". In: *Quantum Information and Computation* 16.5–6 (2016), pp. 361–422. DOI: 10.26421/QIC16.5-6-1. arXiv: 1409.3208 [quant-ph].

[25] Andreas Bauer and Seth Lloyd. *Quadratic Tensors as a Unification of Clifford, Gaussian, and Free-Fermion Physics*. 2026. DOI: 10.48550/arXiv.2601.15396. arXiv: 2601.15396 [quant-ph]. URL: https://arxiv.org/abs/2601.15396.

[26] Yijia Xu, Yixu Wang, and Victor V. Albert. "Multimode rotation-symmetric bosonic codes from homological rotor codes". In: *Phys. Rev. A* 110 (2 Aug. 2024), p. 022402. DOI: 10.1103/PhysRevA.110.022402. URL: https://link.aps.org/doi/10.1103/PhysRevA.110.022402.

[27] Thomas Chambrion et al. "Controllability of the Discrete-Spectrum Schrödinger Equation Driven by an External Field". In: *Annales de l'Institut Henri Poincaré C, Analyse non linéaire* 26.1 (2009), pp. 329–349. DOI: 10.1016/j.anihpc.2008.05.001. arXiv: 0801.4893 [math.OC].

[28] Ugo Boscain et al. "A Weak Spectral Condition for the Controllability of the Bilinear Schrödinger Equation with Application to the Control of a Rotating Planar Molecule". In: *Communications in Mathematical Physics* 311.2 (2012), pp. 423–455. DOI: 10.1007/s00220-012-1441-z. arXiv: 1101.4313 [math.OC].

[29] Vladimír Bužek, Radoslav Derka, and Serge Massar. "Optimal Quantum Clocks". In: *Physical Review Letters* 82.10 (1999), pp. 2207–2210. DOI: 10.1103/PhysRevLett.82.2207. arXiv: quant-ph/9808042 [quant-ph].

[30] Hiroshi Imai and Masahito Hayashi. "Fourier Analytic Approach to Phase Estimation in Quantum Systems". In: *New Journal of Physics* 11.4 (2009), p. 043034. DOI: 10.1088/1367-2630/11/4/043034. URL: https://doi.org/10.1088/1367-2630/11/4/043034.

[31] Masahito Hayashi. "Special Functions in Quantum Phase Estimation". In: *Proceedings of the 16th International Symposium on Orthogonal Polynomials, Special Functions and Applications (OPSFA-16)*. Ed. by Howard S. Cohl et al. Cham: Springer Nature Switzerland, 2025, pp. 81–92. ISBN: 978-3-031-90135-5. DOI: 10.1007/978-3-031-90135-5_5. arXiv: 2302.06899 [quant-ph]. URL: https://doi.org/10.1007/978-3-031-90135-5_5.

[32] Yuan Liu et al. "Toward Mixed Analog-Digital Quantum Signal Processing: Quantum AD/DA Conversion and the Fourier Transform". In: *IEEE Transactions on Signal Processing* 73 (2025), pp. 3641–3655. DOI: 10.1109/TSP.2025.3599462. arXiv: 2408.14729 [eess.SP]. URL: https://doi.org/10.1109/TSP.2025.3599462.

[33] Jens Koch et al. "Charge-insensitive qubit design derived from the Cooper pair box". In: *Phys. Rev. A* 76 (4 Oct. 2007), p. 042319. DOI: 10.1103/PhysRevA.76.042319. URL: https://link.aps.org/doi/10.1103/PhysRevA.76.042319.

[34] Reinier W. Heeres et al. "Cavity State Manipulation Using Photon-Number Selective Phase Gates". In: *Phys. Rev. Lett.* 115.13 (2015), p. 137002. DOI: 10.1103/PhysRevLett.115.137002. URL: https://doi.org/10.1103/PhysRevLett.115.137002.

[35] Asaf A. Diringer et al. "Conditional-Not Displacement: Fast Multioscillator Control with a Single Qubit". In: *Phys. Rev. X* 14.1 (2024), p. 011055. DOI: 10.1103/PhysRevX.14.011055. URL: https://doi.org/10.1103/PhysRevX.14.011055.

[36] Tommaso Rainaldi et al. *Benchmarking Trigonometric Continuous-Variable Gate Primitives with Trapped Ions*. 2026. DOI: 10.48550/arXiv.2607.14085. arXiv: 2607.14085 [quant-ph]. URL: https://arxiv.org/abs/2607.14085.

[37] Amritanshu Prasad, Ilya Shapiro, and M. K. Vemuri. "Locally Compact Abelian Groups with Symplectic Self-Duality". In: *Advances in Mathematics* 225.5 (2010), pp. 2429–2454. DOI: 10.1016/j.aim.2010.04.023. arXiv: 0906.4397 [math.GR].

[38] Daniel Gottesman. "The Heisenberg Representation of Quantum Computers". In: *Group22: Proceedings of the XXII International Colloquium on Group Theoretical Methods in Physics*. Ed. by S. P. Corney, R. Delbourgo, and P. D. Jarvis. Cambridge, MA: International Press, 1999, pp. 32–43. arXiv: quant-ph/9807006 [quant-ph].

[39] David Sprehn and Nathalie Wahl. "Forms over Fields and Witt's Lemma". In: *Mathematica Scandinavica* 126.3 (2020), pp. 401–423. DOI: 10.7146/math.scand.a-120488. arXiv: 1811.12219 [math.KT]. URL: https://doi.org/10.7146/math.scand.a-120488.

[40] P. Oscar Boykin et al. "On Universal and Fault-Tolerant Quantum Computing: A Novel Basis and a New Constructive Proof of Universality for Shor's Basis". In: *40th Annual Symposium on Foundations of Computer Science*. IEEE, 1999, pp. 486–494. DOI: 10.1109/SFFCS.1999.814621. arXiv: quant-ph/9906054 [quant-ph].

[41] Michael A. Nielsen and Isaac L. Chuang. *Quantum Computation and Quantum Information*. Cambridge University Press, 2000.

[42] Aram W. Harrow. "Exact Universality from Any Entangling Gate without Inverses". In: *Quantum Information and Computation* 9.9–10 (2009), pp. 773–777. DOI: 10.26421/QIC9.9-10-4. arXiv: 0806.0631 [quant-ph].

[43] Erez Zohar, J. Ignacio Cirac, and Benni Reznik. "Quantum simulations of lattice gauge theories using ultracold atoms in optical lattices". In: *Reports on Progress in Physics* 79.1 (2016), p. 014401. DOI: 10.1088/0034-4885/79/1/014401. URL: https://doi.org/10.1088/0034-4885/79/1/014401.

[44] Mari Carmen Bañuls and Krzysztof Cichy. "Review on novel methods for lattice gauge theories". In: *Reports on Progress in Physics* 83.2 (2020), p. 024401. DOI: 10.1088/1361-6633/ab6311. URL: https://doi.org/10.1088/1361-6633/ab6311.

[45] Leonard Susskind. "Lattice fermions". In: *Physical Review D* 16.10 (1977), pp. 3031–3039. DOI: 10.1103/PhysRevD.16.3031. URL: https://link.aps.org/doi/10.1103/PhysRevD.16.3031.

[46] Arianna Crippa, Karl Jansen, and Enrico Rinaldi. "Analysis of the confinement string in (2+1)-dimensional quantum electrodynamics with a trapped-ion quantum computer". In: *Communications Physics* 9.1 (2026), p. 46. DOI: 10.1038/s42005-025-02465-8. URL: https://doi.org/10.1038/s42005-025-02465-8.

[47] Pascual Jordan and Eugene Wigner. "Über das Paulische Äquivalenzverbot". In: *Zeitschrift für Physik* 47 (1928), pp. 631–651. DOI: 10.1007/BF01331938. URL: https://doi.org/10.1007/BF01331938.

[48] Masuo Suzuki. "Fractal decomposition of exponential operators with applications to many-body theories and Monte Carlo simulations". In: *Physics Letters A* 146.6 (1990), pp. 319–323. DOI: 10.1016/0375-9601(90)90962-N. URL: https://doi.org/10.1016/0375-9601(90)90962-N.

[49] Alexei Y. Kitaev. *Quantum Measurements and the Abelian Stabilizer Problem*. Electronic Colloquium on Computational Complexity, Report TR96-003. 1996. arXiv: quant-ph/9511026 [quant-ph]. URL: https://eccc.weizmann.ac.il/eccc-reports/1996/TR96-003/.

[50] Richard Cleve et al. "Quantum Algorithms Revisited". In: *Proceedings of the Royal Society of London. Series A: Mathematical, Physical and Engineering Sciences* 454.1969 (1998), pp. 339–354. DOI: 10.1098/rspa.1998.0164. URL: https://doi.org/10.1098/rspa.1998.0164.

[51] Ben C. Travaglione, Gerard J. Milburn, and Timothy C. Ralph. *Phase Estimation as a Quantum Nondemolition Measurement*. 2002. DOI: 10.48550/arXiv.quant-ph/0203130. arXiv: quant-ph/0203130 [quant-ph]. URL: https://arxiv.org/abs/quant-ph/0203130.

[52] Nana Liu et al. "Power of One Qumode for Quantum Computation". In: *Phys. Rev. A* 93.5 (2016), p. 052304. DOI: 10.1103/PhysRevA.93.052304. URL: https://doi.org/10.1103/PhysRevA.93.052304.

[53] Archimedes Pavlidis and Emmanuel Floratos. "Quantum-Fourier-transform-based quantum arithmetic with qudits". In: *Physical Review A* 103.3 (2021), p. 032417. DOI: 10.1103/PhysRevA.103.032417. URL: https://doi.org/10.1103/PhysRevA.103.032417.

[54] Don Coppersmith. *An Approximate Fourier Transform Useful in Quantum Factoring*. IBM Research Report RC 19642. IBM Research Division, T. J. Watson Research Center, 1994. arXiv: quant-ph/0201067 [quant-ph]. URL: https://arxiv.org/abs/quant-ph/0201067. arXiv posting, 2002.

[55] Yiheng Lin et al. "Quantum Entanglement between an Atom and a Molecule". In: *Nature* 581.7808 (2020), pp. 273–277. DOI: 10.1038/s41586-020-2257-1. URL: https://doi.org/10.1038/s41586-020-2257-1.

[56] Tom R. Hepworth et al. "Long-Lived Multilevel Coherences and Spin-1 Dynamics Encoded in the Rotational States of Ultracold Molecules". In: *Nature Communications* 16.1 (2025), p. 7131. DOI: 10.1038/s41467-025-62275-y. URL: https://doi.org/10.1038/s41467-025-62275-y.

[57] F. L. Moore et al. "Atom Optics Realization of the Quantum δ-Kicked Rotor". In: *Phys. Rev. Lett.* 75 (25 Dec. 1995), pp. 4598–4601. DOI: 10.1103/PhysRevLett.75.4598. URL: https://link.aps.org/doi/10.1103/PhysRevLett.75.4598.

[58] Siamak Dadras et al. "Experimental realization of a momentum-space quantum walk". In: *Phys. Rev. A* 99.4 (2019), p. 043617. DOI: 10.1103/PhysRevA.99.043617. URL: https://doi.org/10.1103/PhysRevA.99.043617.

[59] M. Kounalakis et al. "Tuneable Hopping and Nonlinear Cross-Kerr Interactions in a High-Coherence Superconducting Circuit". In: *npj Quantum Information* 4 (2018), p. 38. DOI: 10.1038/s41534-018-0088-9. URL: https://doi.org/10.1038/s41534-018-0088-9.

[60] E. T. Holland et al. "Single-Photon-Resolved Cross-Kerr Interaction for Autonomous Stabilization of Photon-Number States". In: *Phys. Rev. Lett.* 115 (18 Oct. 2015), p. 180501. DOI: 10.1103/PhysRevLett.115.180501. URL: https://link.aps.org/doi/10.1103/PhysRevLett.115.180501.

[61] Michael Reed and Barry Simon. *Methods of Modern Mathematical Physics, Vol. I: Functional Analysis*. Revised and Enlarged. New York: Academic Press, 1980. ISBN: 978-0-12-585050-6.